To the Graduate Council:

I am submitting herewith a dissertation written by Michael O. Bedwell entitled "The Application of a Rejection Technique for Slow Risetime Signals to ARC Timing with a Ge(Li) Detector." I recommend that it be accepted in partial fulfillment of the requirements for the degree of Doctor of Philosophy, with a major in Electrical Engineering.

J. F. Pierce

J. F. Pierce, Major Professor

We have read this dissertation
and recommend its acceptance:

E. D. Kennedy

T. Vaughn Blalock

J. Morlee

Accepted for the Council:

L. Evan Pugh

Vice Chancellor
Graduate Studies and Research

THE APPLICATION OF A REJECTION TECHNIQUE FOR SLOW RISETIME SIGNALS TO ARC TIMING WITH A Ge(Li) DETECTOR

A Dissertation

Presented for the

Doctor of Philosophy

Degree

The University of Tennessee, Knoxville

Michael O. Bedwell

March 1977

1315171

ACKNOWLEDGMENT

I would like to express my appreciation to the members of the committee, Dr. J. F. Pierce (chairman), Dr. T. V. Blalock, Dr. E. J. Kennedy and Dr. F. W. Stallmann, for their assistance in implementing this work. Special thanks go to Dr. J. F. Pierce for his continued guidance throughout the preparation of this dissertation.

I am particularly grateful to ORTEC, Inc. for providing the material and the technical and financial assistance for this project. The stimulating atmosphere and the technical support provided by the ORTEC personnel are greatly appreciated. Particular thanks go to Dr. T. J. Paulus and Dr. R. Nutt for their invaluable assistance.

I am particularly grateful to my wife, Sharon T. Bedwell, for her continued enthusiastic support and for typing the rough draft of this dissertation. Special thanks also go to my parents, Mr. and Mrs. Ray O. Bedwell, for their years of encouragement and for providing the financial means to print this dissertation.

ABSTRACT

The purpose of this investigation was to study the application of a refined constant-fraction discriminator to amplitude-and-risetime compensated (ARC) timing with a Ge(Li) detector. Three distinguishing features of this ARC timing discriminator were discussed. First, a lower-level leading-edge (LLLE) discriminator is used to arm the constant-fraction zero-crossing detector. The threshold level for the LLLE discriminator is automatically set at one-half the minimum energy level required to produce an output pulse from the unit. An upper-level leading-edge (ULLE) discriminator determines the minimum energy level of interest and arms a coincidence gate for the detection of the delayed logic pulse from the zero-crossing detector. The second distinguishing feature of the instrument is the delay t_k, in the path of the timing logic pulse from the crossover detection device. This delay allows approximately 19 nsec. after zero-crossing for the input signal to trigger the ULLE discriminator. Input signals not meeting this constraint produce leading-edge timing at the coincidence gate. The third distinguishing feature of the ARC timing discriminator is the addition of a Slow-Risetime-Reject (SRT) circuit, which can be employed to reject the logic pulses resulting from leading-edge timing. This SRT circuit is intended for use with Ge(Li) detectors or other similar semiconductor detectors, which have charge collection times ranging from 20 nsec. to 200 nsec. or more.

Criteria were derived for the constant-fraction shaping delay, t_d, and for the fixed circuit delay, t_k, to insure ARC timing and to permit the SRT circuitry, when employed, to eliminate logic pulses resulting from leading-edge timing. These criteria were established for three specific input signal shapes—a decreasing slope signal, an increasing slope signal, and a constant slope signal.

Timing resolution improvements resulting from the use of the SRT circuitry were measured. A gamma-gamma timing coincidence experiment was performed, using a 1" x 1", cylindrical, KL236 plastic scintillator, on an RCA 8575 photomultiplier tube, and a true coaxial Ge(Li) detector. The Ge(Li) detector is a right circular cylinder, with a 58.6 cc active volume and a 10.3 percent measured relative efficiency. Timing resolution data were obtained for coincident events in a 1.1:1 dynamic range of energies around the 0.511 MeV energy of ^{22}Na. Timing resolution as a function of threshold level was determined both with and without the use of the SRT circuitry and was plotted. As an example of the resolution improvement, use of the SRT circuitry provided an improvement in the FWHM timing resolution of 33 percent for a 350 keV threshold setting. An improvement of 48 percent was realized in the FW(1/10)M resolution for a 250 keV threshold setting. Photographs of timing spectra qualitatively showed the dramatic improvement in timing that was obtained with the SRT circuitry.

Timing resolution in the Ge(Li) timing system was improved by using the SRT circuitry; however, the counting efficiency was reduced. Because of the risetime constraints imposed by the SRT circuitry, some

input signals that have sufficient amplitude to exceed the threshold level of the discriminator do not produce output pulses. Analytical expressions were derived to describe the relative loss in the counting efficiency of the discriminator when the SRT circuitry is employed.

The expression for the loss in counting efficiency in a particular energy peak as a function of the relative threshold level was verified experimentally. Energy spectra were gated by the ARC timing discriminator, and the counting efficiency loss was determined for the 0.511 MeV photopeak of ^{22}Na and for the 1.174 MeV photopeak of ^{60}Co. The calculated and measured values of the threshold level at which counting efficiency loss became total differed by less than 7 percent. Photographs of several gated energy spectra qualitatively illustrated the loss in counting efficiency caused by using the SRT circuitry.

Calculations for the loss in counting efficiency of the discriminator required a knowledge of the risetime probability density function of signals from the Ge(Li) detector and amplifier system. An experimental technique for measuring this distribution of risetimes was described. For an uncollimated gamma-ray source, the risetime probability density function of signals from the coaxial Ge(Li) detector and amplifier system was shown to be a decaying exponential with a 32.6 nsec. average decay time constant. The distribution was approximately independent of energy in the range considered.

Several additional analytical expressions were derived to further characterize the effects of pulse shapes on constant-fraction timing. An expression was developed to relate the noise on the constant-fraction

signal to the noise on the input signal. Expressions for noise-induced time jitter and for zero-crossing times were derived for true constant-fraction (TCF) and for ARC timing with the three previously mentioned input signals.

TABLE OF CONTENTS

CHAPTER		PAGE
I.	INTRODUCTION	1
	Background	1
	Scope of the Thesis	8
II.	BASIC PRINCIPLES OF LEADING-EDGE AND CONSTANT-FRACTION DISCRIMINATORS	12
	Leading-Edge Technique	12
	Constant-Fraction Technique	23
	Summary	38
III.	SIGNAL FORMATION FOR TIMING	40
	Transfer Function of the Signal Shaping System	40
	Approximate Time Response of the Signal Shaping System	47
	Charge Collection Time Variations in a Ge(Li) Detector	51
	Three Representative Charge Collection Functions	58
	Summary	69
IV.	REJECTION OF LEADING-EDGE SIGNALS: CRITERIA AND EFFECTS	70
	Discussion of Constant-Fraction Implementation	70
	Circuit Delay Criteria	75
	Effects of Slow-Risetime-Reject on Energy Information	92
	Efficiency Loss for Nonuniform Risetime Probability Density	112
	Summary	117
V.	A CONSTANT-FRACTION DISCRIMINATOR WITH DUAL THRESHOLD AND SLOW-RISETIME-REJECT CIRCUITRY	120
	Circuit Description	120
	Specifications	127
	Summary	132
VI.	EXPERIMENTAL RESULTS	133
	Timing Coincidence Measurements	133
	Distribution of Risetimes	147
	System Counting Efficiency Loss	155
	Summary	165

CHAPTER PAGE

VII. CONCLUSIONS 167

Summary 167
Suggestions for Further Study 175

REFERENCES 178

APPENDIX 182

VITA 185

LIST OF FIGURES

FIGURE		PAGE
2.1.	A Typical Representation of a Leading-Edge Discriminator	13
2.2.	Leading-Edge Time Walk Due to Amplitude and Risetime Variations	14
2.3.	Leading-Edge Time-to-Threshold Versus Risetime for Linear, Fixed Amplitude Signals and Various Threshold Levels	17
2.4.	Leading-Edge Time-to-Threshold Versus Signal Amplitude for Linear, Fixed Risetime Signals for Various Risetimes	17
2.5.	Jitter in a Leading-Edge Discriminator	18
2.6.	Timing Error of a Leading-Edge Discriminator Due to Charge Sensitivity of the Discriminating Element	21
2.7.	Functional Representation of a Constant-Fraction Trigger	24
2.8.	Signal Formation in an Ideal Constant-Fraction Trigger, for Linear Input Signals, with t_d Selected for True Constant-Fraction Operation	26
2.9.	Signal Formation in an Ideal Constant-Fraction Trigger, for Linear Input Signals, with t_d Selected for ARC Operation	30
2.10.	Jitter in a Constant-Fraction Discriminator	35
3.1.	Block Diagram of a Signal Processing System for Timing with Ge(Li) Detectors	41
3.2.	Simplified Circuit Model of the Signal Processing System	43
3.3.	Normalized Curves for Charge Collection as a Function of Time at Seven Interaction Positions for an Ideal Double-Open-End Ge(Li) Coaxial Detector	53
3.4.	Curves Representing Three Different Charge Accumulation Functions for a Ge(Li) Coaxial Detector	59

FIGURE PAGE

4.1. Typical Second Generation Constant-Fraction Discriminator, Implemented with MECL II Emitter-Coupled Logic 72

4.2. Block Diagram of a Third Generation Constant-Fraction Discriminator with Double Threshold and Slow-Risetime-Reject Circuitry; Implemented with MECL 10,000 logic . . . 74

4.3. Timing Diagram for the Third Generation Constant-Fraction Discriminator Operating in the ARC Mode with Linear Signals 78

4.4. Uniform Energy Probability Density Function, Modified Due to Rejection of Slow Risetime, Decreasing Slope Input Signals with a Uniform Risetime Probability Density 100

4.5. Uniform Energy Probability Density Function, Modified Due to Rejection of Slow Risetime Linear Input Signals with a Uniform Risetime Probability Density 104

4.6. Uniform Energy Probability Density Function, Modified Due to Rejection of Slow Risetime, Increasing Slope Input Signals with a Uniform Risetime Probability Density 108

4.7. Normalized Loss in System Counting Efficiency at Energy E_2 Due to Rejection of Valid Linear Input Signals because of Slow-Risetime-Reject Circuitry; Risetime Probability Density is Uniform 111

4.8. Uniform Energy Probability Density Function, Modified Due to Rejection of Slow Risetime Linear Input Signals with an Exponential Risetime Probability Density 116

4.9. Normalized Loss in System Counting Efficiency at Energy E_2 as a Function of Threshold Due to Slow-Risetime-Reject Circuit; Linear Input Signals with an Exponential Risetime Probability Density Function 118

5.1. Circuit Diagram of Essential Logic Components in the Third Generation Constant-Fraction Discriminator with Dual Threshold and Slow-Risetime-Reject Circuitry 121

5.2. Timing Diagram for the Discriminator Operating in the ARC Timing Mode with the SRT Circuitry Employed 124

5.3. Test System for Measuring Time Walk in the Discriminator 129

FIGURE PAGE

5.4. Typical Time Walk Curves for the Third Generation Constant-Fraction Discriminator, with Input Signals from a Pulse Generator 130

5.5. Propagation Delay Variation as a Function of Temperature for Four Prototype Units 131

6.1. Gamma-Gamma Timing Coincidence System, Using a Ge(Li) Detector and a Fast Plastic Scintillator 134

6.2. Three Decade Logarithmic Display of Timing Spectra for an Energy Window of 0.511 MeV ± 5%: (a) E_{th}=0.35 MeV, (b) E_{th}=0.25 MeV, and (c) E_{th}=0.1 MeV 137

6.3. Three Decade Logarithmic Display of Timing Spectra for an Energy Window of 0.3 MeV to 0.6 MeV and for: (a) E_{th}=0.25 MeV, (b) E_{th}=0.2 MeV, and (c) E_{th}=0.15 MeV . . 140

6.4. System Timing Resolution as a Function of the ARC2 Discriminator Threshold Setting, for a 1.1:1 (0.511 MeV ± 5%) Dynamic Range of Energies; SRT Circuitry Not Employed 141

6.5. System Timing Resolution as a Function of the ARC2 Discriminator Threshold Setting, for a 1.1:1 (0.511 MeV ± 5%) Dynamic Range of Energies; SRT Circuitry in Use 142

6.6. System Timing Resolution as a Function of the ARC2 Discriminator Threshold Setting, for a 2:1 (0.3 MeV to 0.6 MeV) Dynamic Range of Energies; SRT Circuitry Not Employed 145

6.7. System Timing Resolution as a Function of the ARC2 Discriminator Threshold Setting, for a 2:1 (0.3 MeV to 0.6 MeV) Dynamic Range of Energies; SRT Circuitry in Use . 146

6.8. System for Measuring Risetime Probability Density Functions for Signals from a Coaxial Ge(Li) Detector . . . 149

6.9. Probability Density Functions of 10 Percent to 90 Percent Risetimes for Signals from a Coaxial Ge(Li) Detector-Amplifier System for: (a) the 0.511 MeV Photopeak of ^{22}Na, and (b) the 1.274 MeV Photopeak of ^{22}Na 151

FIGURE PAGE

6.10. Probability Density Functions of 10 Percent to 90 Percent Risetimes for Signals from a Coaxial Ge(Li) Detector-Amplifier System for: (a) the 1.174 MeV Photopeak of ^{60}Co, and (b) the 1.333 MeV Photopeak of ^{60}Co 152

6.11. System Used for Gated Energy Analysis 159

6.12. Five Decade Logarithmic Display of a Gamma-Ray Energy Distribution for ^{60}Co with a Coaxial Ge(Li) Detector: (a) Ungated, (b) Gated by ARC Discriminator without SRT Circuitry, and (c) Gated by ARC Discriminator with SRT Circuitry 161

6.13. Loss in the Counting Efficiency of the Commercial Discriminator, as a Function of Threshold, for the 0.511 MeV Photopeak of ^{22}Na and the 1.174 MeV Photopeak of ^{60}Co 163

A.1. True Coaxial Ge(Li) Detector 184

CHAPTER I

INTRODUCTION

Background

A nuclear detection system consists of a source of nuclear radiation, radiation detectors and various instruments that analyze the energy or the time of occurrence of the detected radiation events. The term nuclear radiation is commonly understood to apply to a wide variety of emanations associated with materials undergoing nuclear transformations. These emanations include atomic and subatomic particles as well as X-rays and gamma-rays.[1]

Methods for detecting nuclear radiation are usually based on either the excitation of atoms or the liberation of charge in the detection medium, caused by the absorption of all or part of the energy of the incident radiation. A scintillation detector is an example of a detector that operates under the principle of excitation of atoms. The basic process of detection in the scintillator involves the emission of light from atoms that are excited by the passage of radiation into the detector. This emitted light is collected by a photomultiplier tube (PMT) and converted into a stream of electrons.[2] Under proper conditions, the charge in the current pulse from the PMT is proportional to the energy lost by the ionizing radiation in the scintillator medium.[1]

A semiconductor detector is an example of a device that operates under the charge liberation principle. Charges (hole-electron pairs) are liberated in an electric field by the passage of radiation into the

detector.[3] The charges are then collected on the detector electrodes to produce a current pulse.[1]

For energy analysis the output current pulse from a PMT or from a semiconductor detector is often applied to the input of a charge-sensitive preamplifier. The preamplifier produces an output voltage pulse with a peak amplitude that is proportional to the total charge in the input current signal. Amplifiers and filters shape and amplify the voltage pulses from the preamplifier and minimize the noise contributed by the electronics and by the detector. Following the amplifiers, discriminators and single-channel analyzers can be used to determine the presence of certain energies in the detected radiation. A discriminator produces an output logic pulse if its input signal exceeds a preset threshold level. A single-channel analyzer (SCA) produces an output logic pulse if the peak amplitude of its input signal falls within the energy window established by two preset threshold levels.

A multichannel analyzer (MCA) can be used to separate the output signals obtained from the detector-amplifier system into incremental ranges of pulse heights. These ranges of pulse amplitudes correspond to ranges of energies in the detected radiation. The number of events occurring in each incremental energy range is counted and stored. This stored energy information can be used to provide a histogram representing a probability density of pulse heights (energies).

Time spectroscopy involves the measurement of the time relationship between the occurrence of two events.[4] A particularly difficult problem in timing is to obtain a signal that is precisely related in time to the

occurrence of a nuclear event. Some form of time-pickoff circuit is employed to produce an output logic pulse that is consistently related in time to the beginning of each input signal. Ideally, the time of occurrence of the logic pulse from the pickoff circuit is insensitive to the shape and to the amplitude of the input signals.

A time-to-pulse-height converter (TPHC) can be used to measure the time relationship between correlated or coincident nuclear events sensed by two different detectors that are irradiated by the same source. A time-pickoff unit is associated with each detector. The logic pulses from one time-pickoff are used to start the TPHC; the logic pulses from the other time-pickoff are used to stop the TPHC. The TPHC is usually implemented by charging a capacitor with a constant-current source during the time interval between a start input pulse and the next stop signal.[4,5] The voltage on the capacitor at the end of the charging interval is proportional to the time difference between the two input signals. This amplitude information is then applied to a multichannel analyzer, which accumulates the data and displays a distribution of start-to-stop time intervals.

Energy restrictions and time coincidence restrictions may be placed on the events that would cause a TPHC output signal. These restrictions are accomplished by using energy side channels, composed of amplifiers, single-channel analyzers and coincidence units. If two nuclear events are coincident within a preset time window and if each of the events is within the proper energy range, the timing information is strobed from the TPHC.

Common to all timing systems is a time-pickoff element.[2] As mentioned previously, an ideal time-pickoff produces a logic pulse at its output that is precisely related in time to the occurrence of a nuclear event. Three important sources of error may occur in time-pickoff measurements: (1) walk (sometimes called time slewing), (2) jitter, and (3) drift.[5] Walk is the time movement of the output pulse from the pickoff element, relative to its input signal, due to variations in the amplitude and the shape of the input signal. Jitter is the timing uncertainty of the pickoff signal caused by noise in the system and by statistical fluctuations in the detector. Drift is the long-term timing error introduced by component aging and by temperature variations in the time-pickoff circuitry.

Three basic time-pickoff methods are commonly used. One of these methods employs a leading-edge trigger, which produces an output logic pulse when the input signal to the trigger crosses a fixed threshold level. This method is normally used for applications involving a very narrow dynamic range of input signal, since time walk due to large variations in input signals amplitude or risetime is severe. Simplicity is a primary advantage of the leading-edge technique.[2]

A second type of time-pickoff method is the crossover technique. Double differentiation of the input signal to the pickoff unit produces a bipolar pulse. The zero-crossing of the bipolar pulse is detected and used to produce an output logic pulse. Walk due to the amplitude variations of input pulses having the same risetime and pulse width is minimized by the crossover technique. However, for a narrow dynamic

range of input pulse amplitudes, timing error due to jitter can be much worse than with the leading-edge trigger.[2,4,6]

A constant-fraction-of-pulse-height trigger is the third commonly used time-pickoff method. In this method an input signal to the unit is delayed and a fraction of the undelayed pulse is substracted from it.[2] A bipolar pulse is generated, and its zero-crossing is detected and used to produce an output logic pulse. Walk due to risetime and amplitude variations of the input signals can be minimized by proper selection of the delay time.[3] Jitter can be minimized for each detector by proper selection of the attenuation factor.[4,7-9] Though difficult to implement, the constant-fraction-of-pulse-height trigger provides timing at a particular fraction of input pulse amplitude regardless of dynamic range.

A typical means of implementing a constant-fraction discriminator is described by Maier and Sperr.[10] In this discriminator identical emitter-coupled logic (ECL) line receivers simultaneously derive a leading-edge signal and a constant-fraction signal. The leading-edge signal arms an ECL AND gate, which acts as a zero-crossing detector for the constant-fraction bipolar pulse. By arming the zero-crossing gate only for an input signal whose amplitude is above the minimum level of interest, noise on the constant-fraction signal does not produce a time-pickoff output signal. The logic signal from the zero-crossing detector triggers a one-shot multivibrator that blocks the logic circuitry for a fixed time that is comparable to the pulse width of the input signal to the discriminator. The one-shot output pulse

is then differentiated to form a standardized output logic pulse that conveys the timing information on its leading edge.

However, the constant-fraction discriminator just described can exhibit excessive time walk characteristics. This problem occurs at the zero-crossing detector. For an input signal with an exceptionally long risetime or with an amplitude only slightly greater than the leading-edge threshold, the constant-fraction and leading-edge signals exchange roles at the input of the zero-crossing gate. Thus the constant-fraction pulse arms the gate for the detection of the leading-edge pulse, resulting in leading-edge timing from the instrument. Timing resolution is severely impaired. Input signals that cause excessive walk in a constant-fraction discriminator occur often when using lithium-drifted, germanium [Ge(Li)] detectors, due to large variations in charge collection time.

Several discriminators have been developed that tend to compensate for the walk effect just described. An instrument developed by White and McDonald uses pulse-shape discrimination to reject pulses that convey poor timing information. This technique employs three parallel constant-fraction discriminators.[11,12] Cho and Chase indicate improved timing resolution with Ge(Li) detectors by using a dual-primed[13] amplitude-and-risetime-compensated (ARC)[9] time-pickoff technique. Maier and Landis show improved Ge(Li) timing by rejecting those logic pulses generated by the leading-edge signal rather than by the constant-fraction signal.[14]

The constant-fraction discriminator described in this dissertation deals with the walk effect in two steps. As in the technique employed by Maier and Sperr, two identical ECL line receivers simultaneously develop a leading-edge signal and a constant-fraction signal. The leading-edge signal arms an ECL AND gate, which acts as a zero-crossing detector for the constant-fraction signal. However, in this instrument the arming signal is developed by using a threshold level for a lower-level leading-edge (LLLE) discriminator that is internally set at one-half the minimum level that is required to produce an output pulse from the instrument. This arming technique helps to insure that, for input signals that reach the minimum level of interest, the leading-edge arming signal and the constant-fraction signal do not exchange roles at the input of the zero-crossing detector.

The threshold for a second or upper-level leading-edge (ULLE) discriminator determines the minimum input signal amplitude that is required to produce an output pulse from the instrument. This leading-edge signal arms an upper-level coincidence gate for the detection of the delayed logic pulse from the zero-crossing detector. For an input signal that has an exceptionally long risetime or that has an amplitude only slightly greater than the upper-level threshold, the delayed timing signal and the upper-level leading-edge signal can exchange roles at the input of the coincidence gate. This condition produces leading-edge timing at the upper-level coincidence gate.

A Slow-Risetime-Reject (SRT) circuit can be used to eliminate those logic signals that result from leading-edge timing introduced at the

upper-level coincidence gate. The output signal from the gate is delayed while the upper-level leading-edge signal and the delayed timing logic pulse are evaluated. The signal from the AND gate is accepted and processed to the output if the upper-level leading-edge signal arrived at the input to the coincidence gate before the delayed timing logic pulse arrived. The signal evaluation process is similar to that used by Maier and Landis.[14] Further processing of a timing signal that is accepted includes a one-shot, to block the logic for the duration of the input signal, and networks to shape the instrument output pulse.

Use of the SRT circuitry improves timing resolution in a Ge(Li) timing system by rejecting those logic pulses generated by leading-edge timing in the constant-fraction discriminator. However, this improvement in timing resolution is made at the expense of the counting efficiency of the system. The SRT circuitry imposes severe risetime constraints on the input signals to the discriminator. Thus, some input signals with sufficient amplitudes to exceed the minimum energy threshold of the discriminator do not produce output signals. The counting efficiency loss, introduced by the use of the SRT circuitry, is not uniform; it is most severe for input signals only slightly exceeding the minimum energy threshold of the constant-fraction discriminator. The nonuniform loss in the counting efficiency of the discriminator results in distorted energy information.

Scope of the Thesis

Since 1967 the constant-fraction time-pickoff method has gained widespread usage in almost all areas that require stringent timing

performance over a wide dynamic range of signal amplitudes and risetimes. This dissertation discusses a signal selection technique that can be employed to significantly improve ARC timing resolution with Ge(Li) detectors. This technique has been applied in a commercially available timing discriminator, which has a worldwide distribution. The many experimenters using the instrument should be aware of the trade-offs to be made between counting efficiency and timing resolution in a Ge(Li) timing system.

The purpose of this dissertation is to study the application of a constant-fraction discriminator, that employs the signal selection process, to a Ge(Li) timing system. The design concept of this discriminator will be discussed, emphasizing the purposes of the double threshold and the Slow-Risetime-Reject (SRT) circuitry. Criteria will be derived for two critical circuit delays. These criteria will permit the experimenter to use the SRT circuitry to eliminate logic pulses resulting from leading-edge timing in the discriminator. Analytical expression will be derived to describe the loss in counting efficiency that results from using the SRT circuitry.

To illustrate the advantages of this new approach, timing resolution measurements will be presented for a gamma-coincidence experiment using a true coaxial Ge(Li) detector. The timing resolution, for the case in which the SRT circuitry is employed, will be compared to the resolution for the case in which SRT circuitry is not employed. In addition, the loss in system counting efficiency, caused

by the use of the SRT circuitry, will be experimentally determined and compared to the analytical prediction.

In Chapter II the basic principles of leading-edge and constant-fraction timing are presented. Timing error due to walk, noise-induced jitter and charge sensitivity are examined for linear input signals.

A system used in processing signals for constant-fraction timing applications with Ge(Li) detectors is shown in Chapter III. An analysis of this system is presented to show that the zero-crossing time of the constant-fraction signal is a function of the charge-collection time in the detector. Three charge accumulation functions are chosen to represent variations in the shape of the signals from a coaxial Ge(Li) detector; a decreasing slope function, a constant slope function and an increasing slope function. True constant-fraction (TCF) and ARC zero-crossing times and expressions for time jitter due to noise are derived for each of these input signal representations.

Chapter IV contains a simplified block diagram of the timing discriminator that was used to obtain the experimental data. A functional circuit description is given, explaining the purpose of the double threshold circuitry and the SRT circuitry. Circuit delay criteria are derived to insure that ARC timing and not leading-edge timing is provided by the instrument when the SRT circuitry is employed. Analytical expressions are derived to describe the reduction in the counting efficiency of the system that results from employing the SRT circuitry.

Chapter V contains a more detailed discussion of the commercially available instrument that was used. A diagram of the logic circuitry, a circuit description and some of the important specifications are presented.

Experimental results are given in Chapter VI. Timing resolution measurements made with and without the SRT circuitry are compared. In addition, measured results of the loss in counting efficiency of the system are given. Conclusions and suggestions for further study are presented in Chapter VII.

CHAPTER II

BASIC PRINCIPLES OF LEADING-EDGE AND CONSTANT-FRACTION DISCRIMINATORS

The basic principles of leading-edge and constant-fraction discriminators are presented in this chapter. Timing errors due to amplitude and risetime dependent time walk, noise-induced time jitter and charge sensitivity are illustrated for these time-pickoff techniques, using linear signals.

Leading-Edge Technique

As indicated in Chapter I, an ideal time-pickoff circuit produces an output logic pulse that is precisely related in time to the beginning of an input signal. The time of occurrence of the output pulse should be independent of both the amplitude and the risetime of the input signal.

A leading-edge discriminator is the simplest means of deriving a time-pickoff signal; it produces an output logic pulse when the input signal crosses a fixed threshold level. A conventional representation for a leading-edge discriminator is shown in Figure 2.1. A primary disadvantage of the leading-edge technique is that the time of occurrence of the output pulse from a leading-edge trigger is a function of the amplitude and the risetime of the input signal.

Figure 2.2 illustrates the time walk of an ideal leading-edge discriminator due to variations in the amplitude and risetime of linear

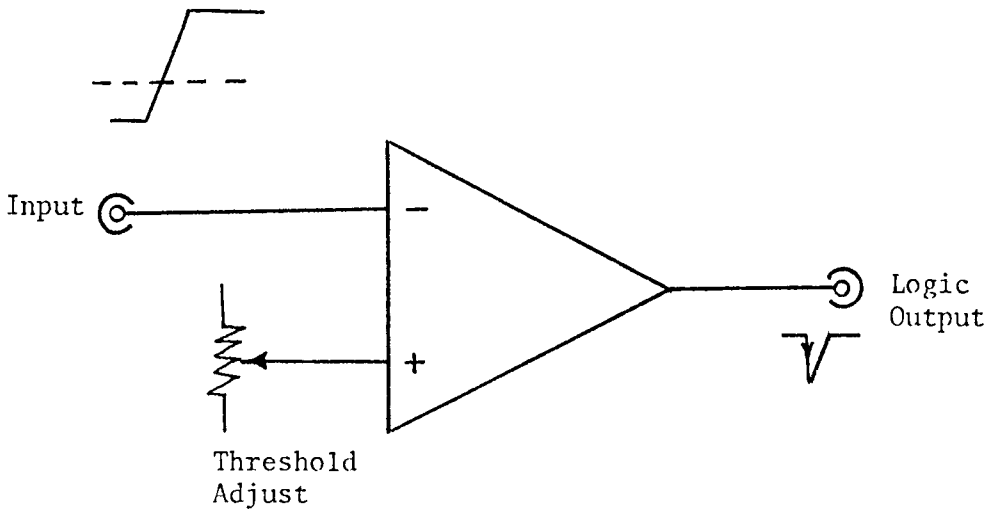


Figure 2.1. A typical representation of a leading-edge discriminator.

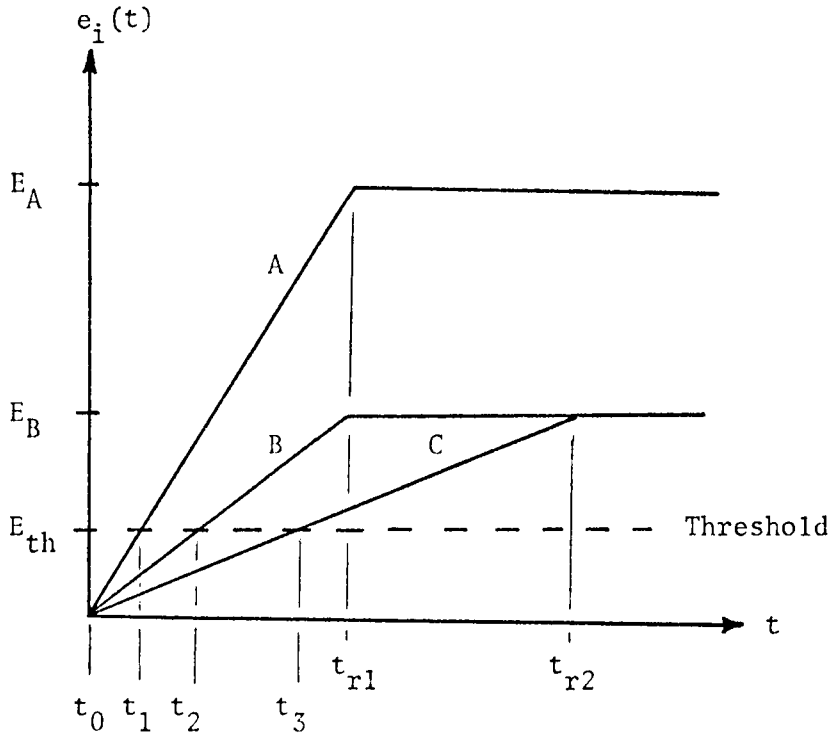


Figure 2.2. Leading-edge time walk due to amplitude and risetime variations.

input signals. Signals A and B are linear signals that have the same risetime but different amplitudes. Although signals A and B occur simultaneously, the discriminator senses them at different times, t_1 and t_2. Signals B and C of Figure 2.2 are linear input signals that have the same amplitude but different risetimes. They also occur simultaneously but are sensed at different times, t_2 and t_3, by the leading-edge discriminator. Walk (or time slewing) is a term used to describe timing error caused by variations in the shape and the amplitude of the pulses applied to the input of the discriminator. Walk is one of the three major sources of timing error mentioned in Chapter I.

Time walk in an ideal leading-edge discriminator can be characterized for the simple illustrative case involving linear signals. Let a linear input signal to the ideal leading-edge discriminator be represented by the equation

$$e_i(t) = \frac{E_A t U(t)}{t_{r1}} - \frac{E_A (t-t_{r1}) U(t-t_{r1})}{t_{r1}} , \qquad (2.1)$$

which can be shown as signal A in Figure 2.2. The threshold of the leading-edge discriminator is set at a level E_{th} that is less than the maximum signal amplitude, E_A. The time at which the signal crosses through the threshold is t_1, which is less than the risetime, t_{r1}. At the time of threshold crossing, Equation (2.1) becomes

$$e_i(t_1) = E_{th} = \frac{E_A t_1}{t_{r1}} . \qquad (2.2)$$

Solving for the threshold crossing time yields

$$t_1 = \frac{E_{th} t_{rl}}{E_A} . \qquad (2.3)$$

The threshold crossing time as a function of input signal risetime is shown in Figure 2.3 for linear input signals of identical amplitude and for various threshold levels. Figure 2.4 shows the time-to-threshold as a function of signal amplitude for linear input signals of identical risetimes, for several different risetimes. From these figures and from Equation (2.3), time walk in a leading-edge trigger is shown to be reduced for signals with shorter risetimes and for signals that greatly exceed the threshold level of the discriminator.

Jitter is another major source of error in time-pickoff techniques. Jitter is the term applied to timing uncertainty caused by statistical fluctuations in the detector signal and by noise. The noise can be present on the detector signal; it can be generated by the processing electronics; or it can be generated by the discriminator itself. Noise on the input signal to a leading-edge discriminator causes an uncertainty in the time at which the signal crosses the discriminator threshold level. This uncertainty is illustrated in Figure 2.5.

An estimate of the noise-induced timing uncertainty in a leading-edge trigger can be accomplished for input signals that are approximately linear in the region of threshold crossing. A linear input signal to an ideal leading-edge discriminator is shown in Figure 2.5 and can be represented by Equation (2.1). Let E_n be the root mean-square (RMS)

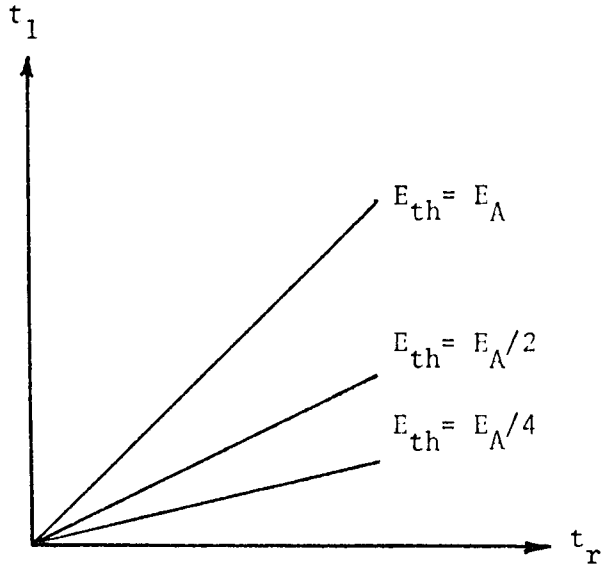


Figure 2.3. Leading-edge time-to-threshold versus risetime for linear, fixed amplitude signals and various threshold levels.

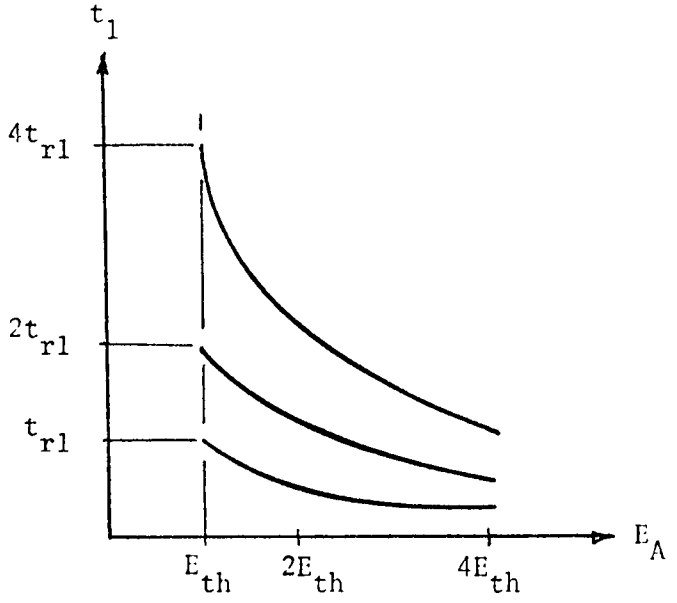


Figure 2.4. Leading-edge time-to-threshold versus signal amplitude for linear, fixed risetime signals for various risetimes.

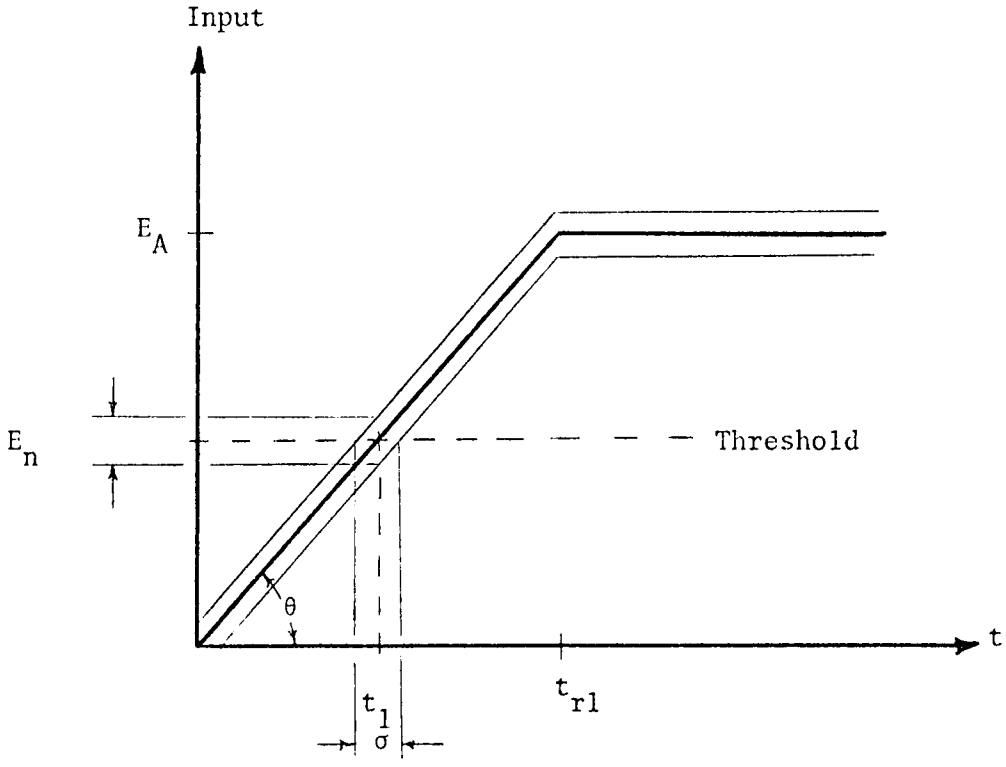


Figure 2.5. Jitter in a leading-edge discriminator.

value of the noise envelope riding on the input signal, and let $\tan\theta$ be the slope of the leading edge of the input signal. The RMS uncertainty in the time of the threshold crossing of $e_i(t)$ is

$$\sigma = \left.\frac{E_n}{\tan\theta}\right|_{t=t_1} . \tag{2.4}$$

For a more generalized input signal shape the RMS timing jitter is

$$\sigma = \left.\frac{E_n}{de_i(t)/dt}\right|_{t=t_1} , \tag{2.5}$$

where $e_i(t)$ is the input signal. In obtaining this expression, the input signal is assumed to be approximately linear in the region of threshold crossing. Additionally, the discriminator threshold level is assumed to be removed from both the zero level and the peak amplitude of the signal by at least the width of the noise band.[3,5,15] Equation (2.5) indicates that a faster input signal (i.e. one with a greater slope) produces less timing error due to jitter for a given noise component than does a slower input signal. When using the leading-edge technique, the best timing resolution is often found by experimenting with different threshold levels.[3]

One source of timing error not mentioned specifically in Chapter I is charge sensitivity. Charge sensitivity is a term used to describe the timing error due to the finite charge that is required to trigger a physically realizable threshold or crossover detecting device. This source of error is illustrated for a leading-edge discriminator in

Figure 2.6. After an input signal passes the discriminator threshold level, a small additional amount of charge is required to actually trip the discriminating element. Charge sensitivity introduces changes in the effective threshold level and changes in the effective sensing time of the leading-edge discriminator. In Figure 2.6 the times t_{10}, t_{20} and t_{30} are the times at which the discriminator output signals actually occur, relative to times t_1, t_2 and t_3, respectively, at which the input signals cross the threshold level.

To characterize the effects of charge sensitivity shown in Figure 2.6, let the linear input signal to a leading-edge discriminator be described by Equation (2.1), page 15. Let k be the area under the input signal curve that is related to the additional charge required to trigger the discriminator after threshold has been crossed. Referring to Figure 2.6, the triangular area k is the integral of the input signal from the threshold crossing time t_1 to the time t_{10} at which the discriminator actually triggers, or

$$k = \int_{t_1}^{t_{10}} e_i(t)dt = \frac{E_A(\Delta t_k)^2}{2t_{rl}} . \qquad (2.6)$$

The time required to accumulate the additional charge is Δt_k, or

$$\Delta t_k = t_{10}-t_1 . \qquad (2.7)$$

The effective threshold level for the discriminator is

$$E_{th(eff)} = E_{th}+\Delta E_{th} , \qquad (2.8)$$

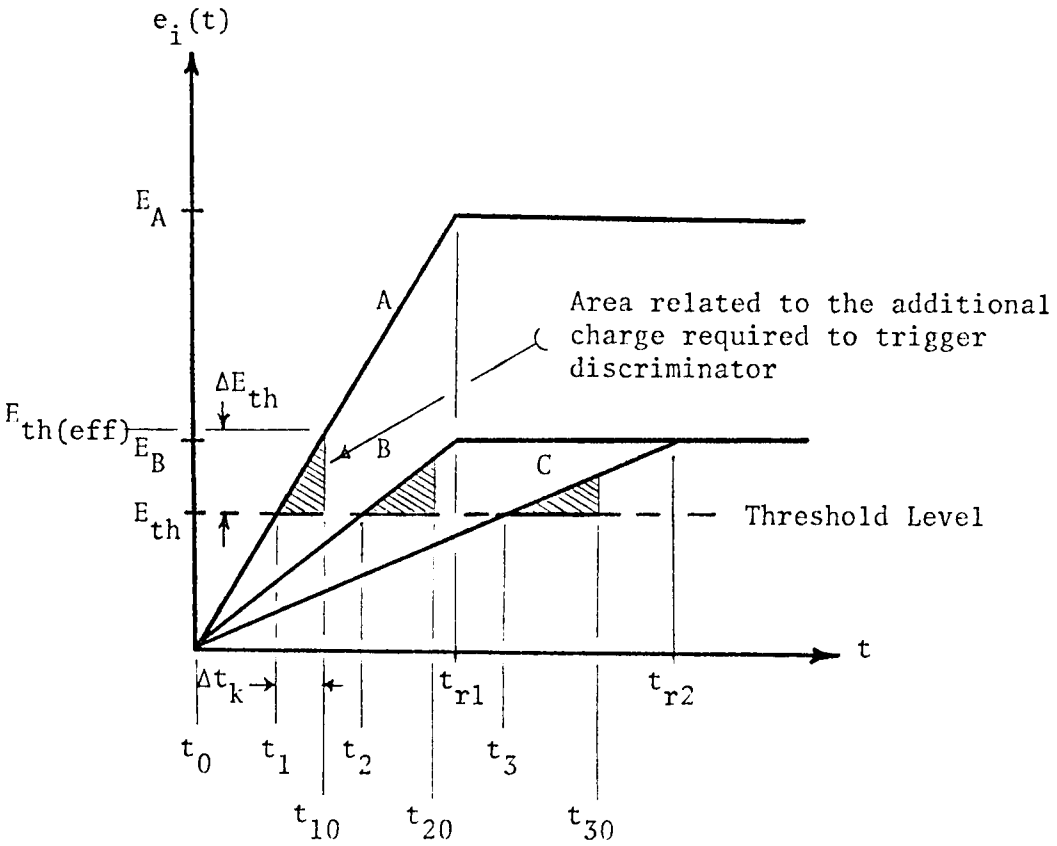


Figure 2.6. Timing error of a leading-edge discriminator due to charge sensitivity of the discriminating element.

where E_{th} is the dc threshold level and ΔE_{th} is the additional signal amplitude required to produce the required charge. From Equation (2.6) the Δ-change in effective discriminator sensing time is

$$\Delta t_k = \sqrt{\frac{2kt_{rl}}{E_A}} . \tag{2.9}$$

The Δ-change in effective threshold level is related to the Δ-change in sensing time by the slope of the input signal, or

$$\Delta E_{th} = \frac{E_A \Delta t_k}{t_{rl}} . \tag{2.10}$$

Equations (2.9) and (2.10) can be combined to yield another expression for the Δ-change in threshold level, or

$$\Delta E_{th} = \sqrt{\frac{2kE_A}{t_{rl}}} . \tag{2.11}$$

For more generalized input signals, the slope of the input signal at the time of threshold crossing may be used in place of the slope for the linear signal. Thus,

$$\frac{E_A}{t_{rl}} = \left.\frac{de_i(t)}{dt}\right|_{t=t_1} \tag{2.12}$$

can be used in Equations (2.6) through (2.11), if $e_i(t)$ is approximately linear in the region of threshold crossing.

The Δ-changes in effective threshold level and effective threshold crossing time represent the amount of departure from the ideal leading-edge discriminator. If the charge-related area, k, is considered to be constant for all types of input signals, the Δ-change in effective threshold crossing time is reduced by fast signals that greatly exceed threshold, thus reducing time-pickoff error due to charge sensitivity. Those input signal conditions that improve timing, however, increase the change in effective threshold level.

In general, leading-edge timing should be used only in applications involving a narrow dynamic range of input signals. Time slewing is severe for a leading-edge discriminator with input signals of widely varying amplitudes and risetimes. Timing errors due to noise-induced jitter, walk and charge sensitivity are reduced in the leading-edge technique for input signals with shorter risetimes.

Constant-Fraction Technique

Several publications indicate that there is a particular fraction of detector pulse amplitude at which a time-pickoff signal should be generated in order to produce optimum timing resolution.[7,8,11,16-20] This fraction varies with the type of detector being used. The constant-fraction-of-pulse-height trigger was originally developed to provide time-pickoff triggering at the same fraction of input pulse height for every input signal, regardless of its amplitude.[7,8]

A functional representation of a constant-fraction trigger is shown in Figure 2.7. An input pulse is delayed, and a fraction of the undelayed pulse is subtracted from it. This produces a bipolar pulse

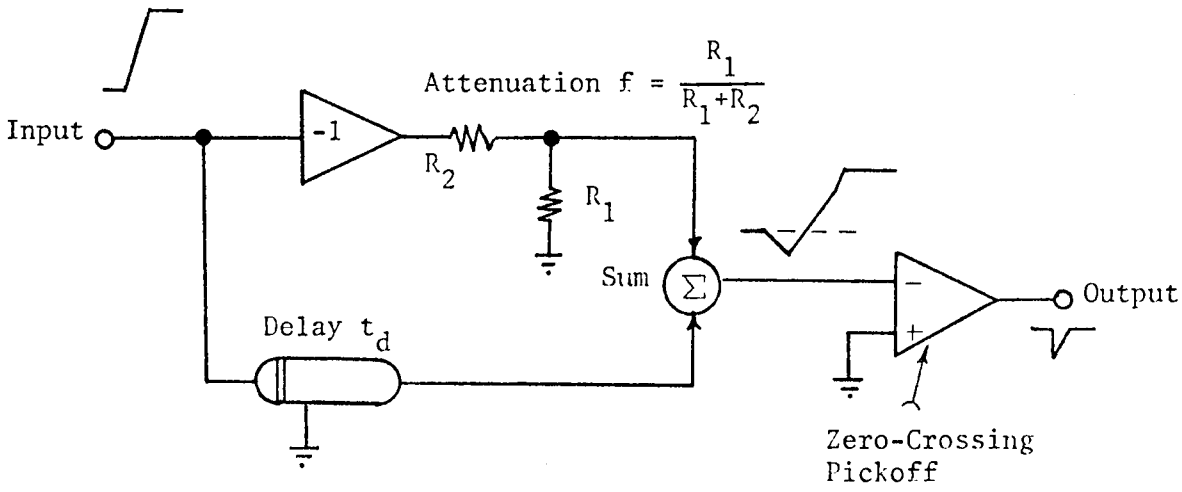


Figure 2.7. Functional representation of a constant-fraction trigger.

with a zero-crossing time that is ideally independent of input pulse amplitude. The amplitude independence of the constant-fraction zero-crossing time is shown for the linear signals A and B in Figure 2.8. From signals B and C the zero-crossing time is seen to be dependent on the risetime of the input signal.

Expressions for the zero-crossing time of a constant-fraction signal can be readily obtained for cases involving linear signals. Let a linear input signal to an ideal constant-fraction trigger be described by

$$U(t) = \begin{cases} 0 & t < 0 \\ 1 & t > 0 \end{cases}$$

$$e_i(t) = \frac{E_p t U(t)}{t_r} - \frac{E_p (t-t_r) U(t-t_r)}{t_r}, \qquad (2.13)$$

where E_p is the maximum amplitude of the pulse and t_r is its risetime. This signal is delayed by a fixed time t_d in one constant-fraction signal path, and it is inverted and attenuated by a factor f in the other path. From Equation (2.13) the delayed input pulse is

$$e_d(t) = e_i(t-t_d) = \frac{E_p (t-t_d) U(t-t_d)}{t_r} - \frac{E_p (t-t_d-t_r) U(t-t_d-t_r)}{t_r}, \qquad (2.14)$$

and the inverted, attenuated input pulse is

$$e_a(t) = -f e_i(t) = -\frac{f E_p t U(t)}{t_r} + \frac{f E_p (t-t_r) U(t-t_r)}{t_r}. \qquad (2.15)$$

Summing Equations (2.14) and (2.15) yields the bipolar constant-fraction signal

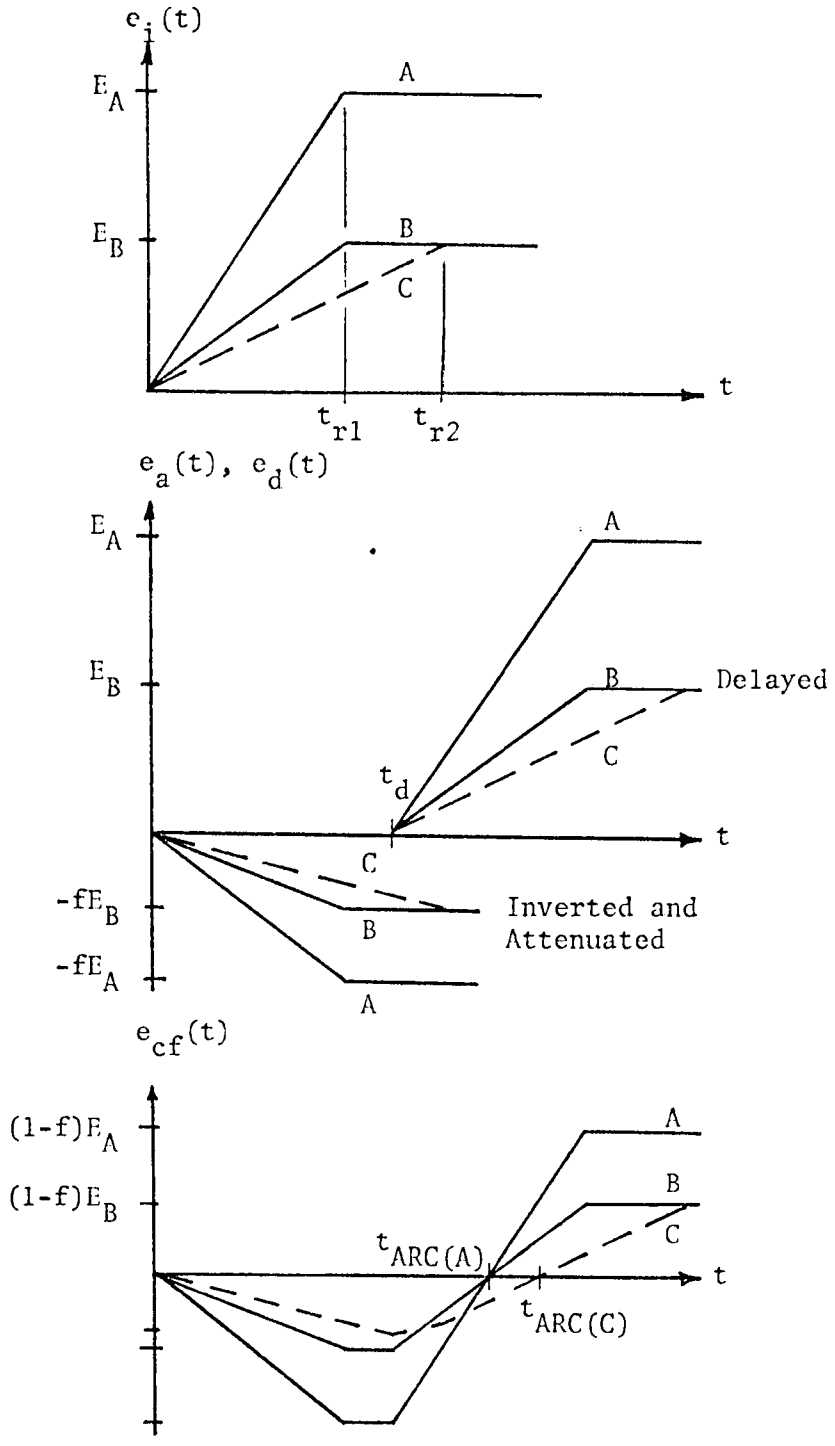


Figure 2.8. Signal formation in an ideal constant-fraction trigger, for linear input signals, with t_d selected for true constant-fraction operation.

$$e_{cf}(t) = e_d(t) + e_a(t) \ , \tag{2.16}$$

or

$$e_{cf}(t) = -\frac{fE_p tU(t)}{t_r} + \frac{E_p(t-t_d)U(t-t_d)}{t_r} +$$

$$+ \frac{fE_p(t-t_r)U(t-t_r)}{t_r} - \frac{E_p(t-t_d-t_r)U(t-t_d-t_r)}{t_r} \ . \tag{2.17}$$

Two cases must be considered in determining the zero-crossing time of the constant-fraction signal. The first case is for true constant-fraction (TCF) timing, and the second case is for amplitude-and-risetime-compensated (ARC) timing. In the TCF case the time of zero-crossing occurs after the attenuated signal has reached its full amplitude, or

$$t_{TCF} > t_r \ . \tag{2.18}$$

To solve for the TCF crossover time, set Equation (2.17) to zero for the condition of Equation (2.18); thus

$$e_{cf}(t_{TCF}) = -\frac{fE_p t_{TCF}}{t_r} + \frac{E_p(t_{TCF}-t_d)}{t_r} + \frac{fE_p(t_{TCF}-t_r)}{t_r} = 0 \ . \tag{2.19}$$

for $t_{TCF} < t_r + t_d$

Solving for t_{TCF} gives

$$t_{TCF} = t_d + ft_r \ . \tag{2.20}$$

This equation shows that the true constant-fraction (TCF) zero-crossing time, t_{TCF}, is independent of input signal amplitude but dependent on input signal risetime. Incorporating Equation (2.20) into the inequality

in (2.18) yields the limiting value of the fixed delay time t_d for true constant-fraction (TCF) triggering; thus

$$t_d > (1-f)t_{r(max)} , \tag{2.21}$$

where $t_{r(max)}$ is the maximum expected input signal risetime.

In the ARC case the constant-fraction zero-crossing occurs before the attenuated detector signal has reached its full amplitude, or

$$t_{ARC} < t_r . \tag{2.22}$$

To solve for the ARC crossover time, set Equation (2.17) to zero for the condition of Equation (2.22); thus

$$e_{cf}(t_{ARC}) = -\frac{fE_p t_{ARC}}{t_r} + \frac{E_p(t_{ARC}-t_d)}{t_r} = 0 . \tag{2.23}$$

Solving for t_{ARC} gives

$$t_{ARC} = \frac{t_d}{1-f} . \tag{2.24}$$

From this equation the zero-crossing time for ARC timing is seen to be independent of both input signal amplitude and input signal risetime. Incorporating Equation (2.24) into the inequality in (2.22) yields the limiting value of the fixed delay time t_d for ARC timing; thus

$$t_d < (1-f)t_{r(min)} , \tag{2.25}$$

where $t_{r(min)}$ is the minimum expected input signal risetime. Signal formation in an ideal constant-fraction discriminator that is operating in the ARC mode is shown in Figure 2.9, for linear input signals. The amplitude and risetime independence of the crossover point is illustrated in this figure.

For linear signals, time walk can be reduced and ideally eliminated by employing the ARC form of the constant-fraction time-pickoff technique. TCF and ARC timing can, therefore, be used in applications involving much wider dynamic ranges of input signal amplitudes and risetimes than can leading-edge timing.

Jitter due to noise and to statistical fluctuations in the detector is a major source of timing error in all time-pickoff techniques. As mentioned previously, the constant-fraction trigger was developed to provide a time-pickoff signal at the fraction of input pulse amplitude at which timing error due to jitter is minimized.

In ARC timing the effective fraction of the input pulse amplitude at which the time-pickoff logic signal is generated differs from that for the true constant-fraction (TCF) pickoff. If the discriminator is operating in the TCF mode, zero-crossing occurs after the attenuated signal has reached its full amplitude. Therefore, the pickoff signal is generated at a fraction f of the input pulse height that is determined by the resistive attenuator placed in the constant-fraction signal path. This attenuator is composed of resistors R_1 and R_2 in Figure 2.7, page 24. The attenuation factor is

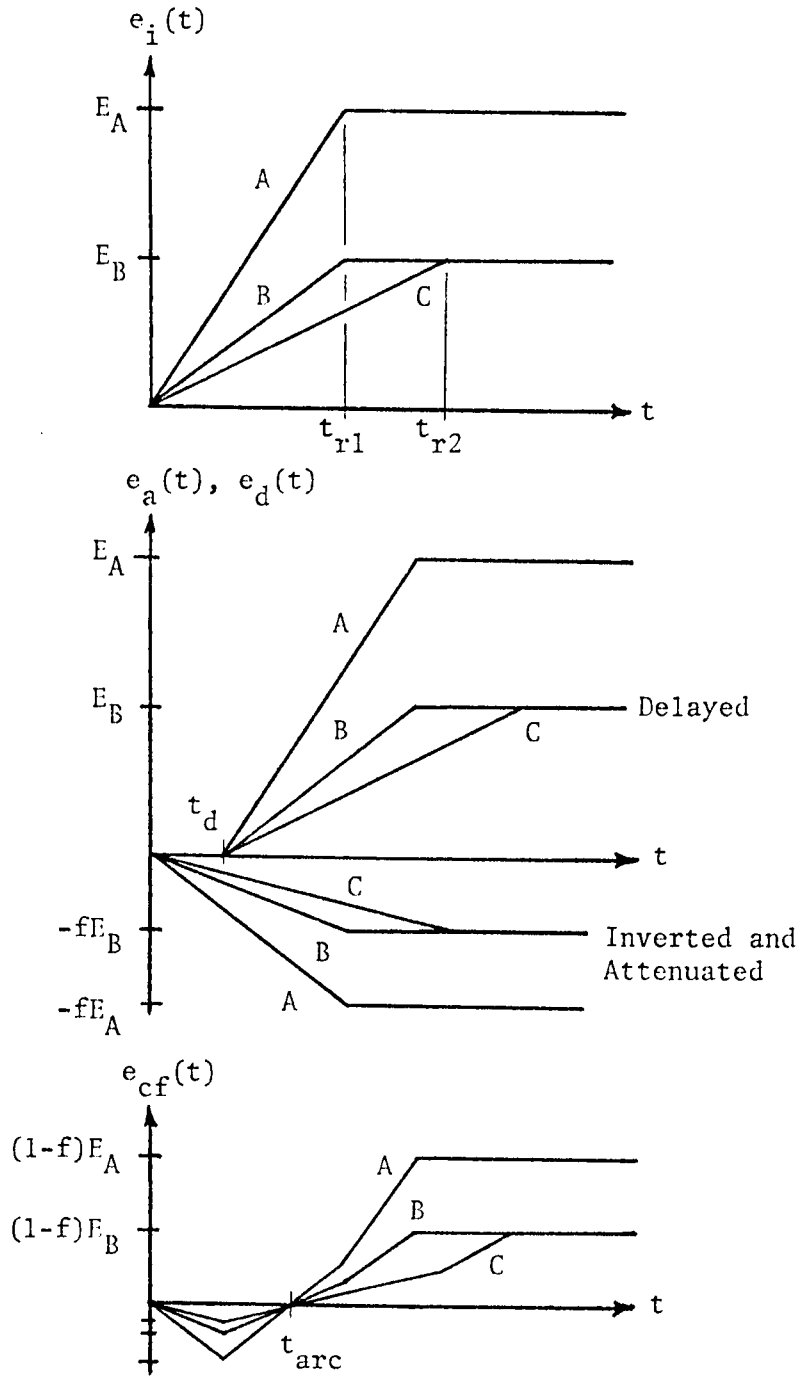


Figure 2.9. Signal formation in an ideal constant-fraction trigger, for linear input signals, with t_d selected for ARC operation.

$$f_{TCF(eff)} = f = \frac{R_1}{R_1+R_2} . \tag{2.26}$$

For ARC timing, zero-crossing occurs before the attenuated detector signal has reached its full amplitude. Therefore, the effective fraction of the input signal at which an ARC pickoff logic pulse is generated is dependent upon the portion of the attenuated signal which has occurred at the zero-crossing time. Using Equations (2.22) and (2.24) in Equation (2.15), page 25, yields the ARC timing effective fraction; thus

$$-e_a(t_{ARC}) = f_{ARC(eff)}E_p , \tag{2.27}$$

or

$$f_{ARC(eff)} = \frac{ft_d}{(1-f)t_r} . \tag{2.28}$$

The effective fraction for ARC timing is always less than the fixed attenuation factor f, and it is dependent on the input signal risetime. The effective triggering fraction is the parameter that must be optimized for the ARC timing technique in order to achieve best resolution.

To illustrate jitter due to noise in constant-fraction timing, let $e_n(t)$ be the input noise signal to the ideal constant-fraction trigger shown in Figure 2.7, page 24. The composite noise voltage from the constant-fraction summing junction is

$$e_{ncf}(t) = -fe_n(t) + e_n(t-t_d) . \tag{2.29}$$

The mean-square value of the composite noise signal is defined by

$$\overline{e^2_{ncf}(t)} = \int_{-\infty}^{\infty} e^2_{ncf}(t)p(e_{ncf})de_{ncf} , \qquad (2.30)$$

where $p(e_{ncf})$ is the probability density function of the constant-fraction noise voltage. Squaring the composite noise signal in Equation (2.29) and using the squared value in Equation (2.30) yields

$$\overline{e^2_{ncf}(t)} = \int_{-\infty}^{\infty}\int_{-\infty}^{\infty} \{[f^2e^2_n(t) + e^2_n(t-t_d) +$$

$$- 2fe_n(t)e_n(t-t_d)]p[e_n(t),e_n(t-t_d),t_d]\}d[e_n(t)]d[e_n(t-t_d)], \qquad (2.31)$$

using the joint probability density function of $e_n(t)$ and $e_n(t-t_d)$. From the definition for mean-square, the preceding equation becomes

$$\overline{e^2_{ncf}(t)} = f^2\,\overline{e^2_n(t)} + \overline{e^2_n(t-t_d)} - 2f\,\overline{e_n(t)e_n(t-t_d)} . \qquad (2.32)$$

For a time stationary process the mean-square value of the input noise is independent of the time at which it is determined;[21] thus, in Equation (2.32)

$$\overline{e^2_n(t-t_d)} = \overline{e^2_n(t)} . \qquad (2.33)$$

The last term in Equation (2.32) involves a function known as the autocorrelation function of the input noise,[21,22] or

$$\phi(t_d) = \overline{e_n(t)e_n(t-t_d)} . \qquad (2.34)$$

Furthermore, the magnitude of the autocorrelation function is always less than or equal to the mean-square value of the input noise, or

$$|\phi(t_d)| \leq \overline{e_n^2(t)} \ . \tag{2.35}$$

Incorporating Equations (2.33) and (2.34) into (2.32) yields

$$\overline{e_{ncf}^2(t)} = (1+f^2)\ \overline{e_n^2(t)} - 2f\phi(t_d) \ , \tag{2.36}$$

or rearranging terms

$$\overline{e_{ncf}^2(t)} = \overline{e_n^2(t)} \left[1+f^2 - \frac{2f\phi(t_d)}{\overline{e_n^2(t)}}\right] \ . \tag{2.37}$$

The root mean-square (RMS) value of the constant-fraction composite noise is the square root of Equation (2.37), or

$$E_{ncf} = E_n \sqrt{1+f^2 - \frac{2f\phi(t_d)}{\overline{e_n^2(t)}}} \ , \tag{2.38}$$

where E_n is the RMS value of the input noise. This equation is a general expression relating the RMS value of the composite noise signal from the constant-fraction summing junction to the RMS value of the input noise.

From Equation (2.35) the limits on the value of the autocorrelation function can be written as

$$-1 \leq \frac{\phi(t_d)}{e_n^2(t)} \leq 1 \ . \tag{2.39}$$

Therefore, for an attenuation factor f, such that

$$0 < f < 1 \ , \tag{2.40}$$

limits can be set on the RMS value of the composite constant-fraction noise, relative to the RMS value of the input noise; or, from Equations (2.38), (2.39) and (2.40)

$$(1-f)E_n \leq E_{ncf} \leq (1+f)E_n \ . \tag{2.41}$$

Equation (2.41) indicates that the RMS value of the noise on the constant-fraction signal is greater than the RMS value of the input noise, for uncorrelated noise. The constant-fraction composite noise is uncorrelated if $\phi(t_d)$ is negligibly small for the selected value of the delay t_d. This case implies that there is no orderly relationship between the input noise, $e_n(t)$, and the delayed input noise, $e_n(t-t_d)$.

Time jitter in an ideal constant-fraction discriminator due to the RMS value of the composite noise E_{ncf} is illustrated in Figure 2.10. Assuming linearity of the composite constant-fraction signal in the region of zero-crossing, the RMS uncertainty in zero-crossing time is represented in general by

$$\sigma_{cf} = \frac{E_{ncf}}{de_{cf}(t)/dt\big|_{t=t_{cf}}} \ . \tag{2.42}$$

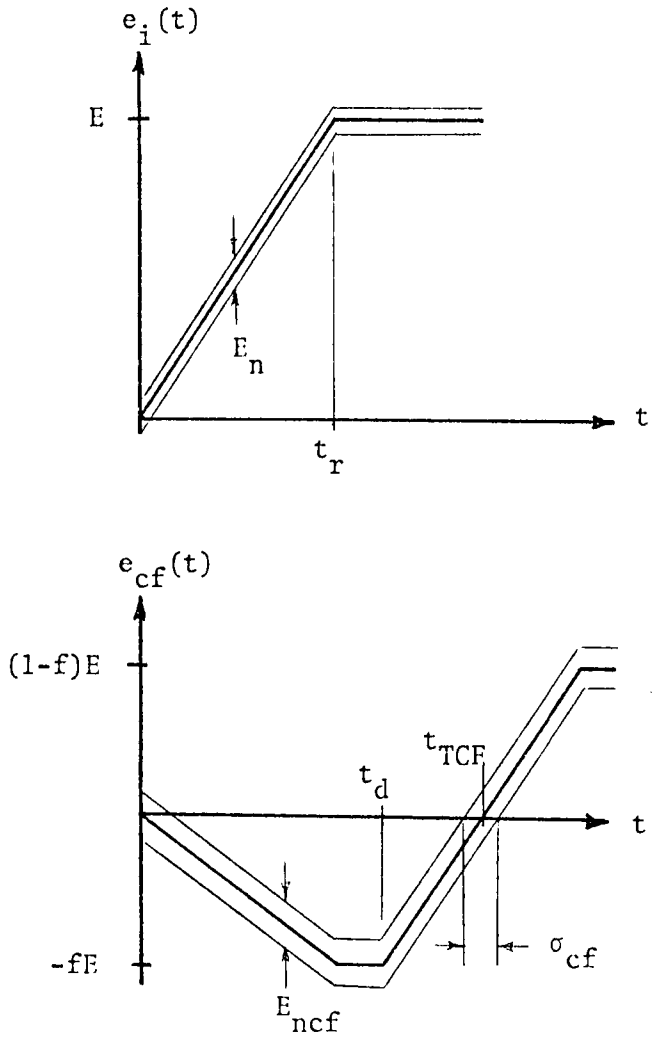


Figure 2.10. Jitter in a constant-fraction discriminator.

Substituting the slope of the signal in Equation (2.17), page 27, at TCF zero-crossing, into Equation (2.42) gives the noise-induced RMS time jitter from the TCF discriminator for the linear input signal of Equation (2.13), page 25; thus,

$$\sigma_{TCF} = \frac{E_{ncf}t_r}{E_p} . \tag{2.43}$$

Using a similar approach an expression for the noise induced RMS time jitter in ARC timing is

$$\sigma_{ARC} = \frac{E_{ncf}t_r}{E_p(1-f)} . \tag{2.44}$$

Crossover uncertainty from jitter due to noise is reduced for bipolar signals with greater slopes at zero-crossing.

For an extremely narrow dynamic range of input signals, the threshold of a leading-edge discriminator can be set at the optimum fraction of input pulse heights for minimum jitter. Applying identical input signals with equal RMS values of noise to the leading-edge and the constant-fraction discriminators, the noise-induced RMS time jitter of the two types of time pickoffs can be compared from Equation (2.5), page 19, and Equations (2.43) and (2.44). For uncorrelated noise, the leading-edge trigger can provide better time resolution than the constant-fraction trigger. From the standpoint of jitter, the advantage of constant-fraction timing is that a time-pickoff signal can be produced at the optimum fraction of input pulse height for a wide dynamic range of pulse amplitudes.

Timing error due to charge sensitivity has been illustrated for a leading-edge discriminator in Figure 2.6, page 21. Since the zero-crossing of a constant-fraction bipolar signal must be detected by some real discriminating element, charge sensitivity produces timing error in a constant-fraction discriminator also. To characterize charge sensitivity for a zero-crossing detector, let k be the area under the constant-fraction signal curve that is related to the small additional amount of charge which is required to trip the zero-crossing detector after true zero-crossing has occurred. The triangular area k is the integral of the constant-fraction signal from the actual zero-crossing time to the time at which the discriminator fires; thus,

$$k = \int_{t_{cf}}^{t_{cf}+\Delta t_c} e_{cf}(t)dt \simeq \frac{1}{2}\left[\frac{de_{cf}(t)}{dt}\right]_{t=t_{cf}} (\Delta t_c)^2 . \qquad (2.45)$$

The constant-fraction signal, $e_{cf}(t)$, is assumed to be linear in the region of zero-crossing. The charge sensitivity error, Δt_c, in zero-crossing time is then

$$\Delta t_c = \sqrt{\frac{2k}{\left.\frac{de_{cf}(t)}{dt}\right|_{t=t_{cf}}}} . \qquad (2.46)$$

Assuming linear signals in a constant-fraction discriminator, and substituting the signal slope at zero-crossing of the bipolar pulse of Equation (2.17), page 27, into Equation (2.46) gives the zero-crossing error due to charge sensitivity for TCF timing as

$$\Delta t_{c(TCF)} = \sqrt{\frac{2kt_r}{E_p}}, \tag{2.47}$$

and for ARC timing as

$$\Delta t_{c(ARC)} = \sqrt{\frac{2kt_r}{(1-f)E_p}}. \tag{2.48}$$

Equations (2.46), (2.47) and (2.48) indicate that, in general, timing error due to charge sensitivity is worse for signals with lower slopes. For a given input signal risetime, the charge sensitivity error is worse for ARC timing than it is for true constant-fraction timing.

Summary

Chapter II illustrates some of the advantages and disadvantages of the TCF and ARC timing technique relative to the leading-edge timing technique. A leading-edge discriminator offers the advantage of simplicity and may also provide the best timing resolution for a very narrow dynamic range of input signal amplitudes if the timing error due to jitter is caused by uncorrelated noise sources. Time walk in a leading-edge discriminator is severe for a wide range of input signal amplitudes and risetimes.

A constant-fraction discriminator is usually difficult to implement. However, by using the ARC mode of a constant-fraction trigger, time walk due to variations in input signal amplitudes and risetimes can ideally be eliminated for a wide range of linear signals. Furthermore, a time-pickoff signal can be generated at the fraction of input pulse height that provides optimum time resolution for a wide range of input

signal amplitudes. The constant fraction technique may provide worse time resolution than the leading-edge technique for a very narrow dynamic range of input signals if the jitter is due to uncorrelated noise.

CHAPTER III

SIGNAL FORMATION FOR TIMING

A system used in processing signals for constant-fraction timing applications with Ge(Li) detectors is shown in this chapter, and a simplified transfer function for the system is derived. An approximation for the constant-fraction zero-crossing time is derived for this timing system, assuming an exponential current pulse shape from the detector. The constant-fraction zero-crossing time is shown to be a function of the charge collection time in the Ge(Li) detector.

The charge collection time variations for Ge(Li) coaxial detectors have been reported in the current literature. Based on these studies three signals are chosen to represent the pulse shape variations at the input of a constant-fraction discriminator, due to variations in the charge collection time in a detector. True constant-fraction and ARC zero-crossing times and expressions for time jitter due to noise are derived for these input pulse shapes.

Transfer Function of the Signal Shaping System

The block diagram of a signal processing system used in timing applications with Ge(Li) detectors is shown in Figure 3.1. A semiconductor detector produces a current pulse with a charge that is proportional to the energy of the detected radiation. This current pulse is integrated by a charge-sensitive preamplifier to produce an output voltage signal with a peak amplitude that is proportional to the

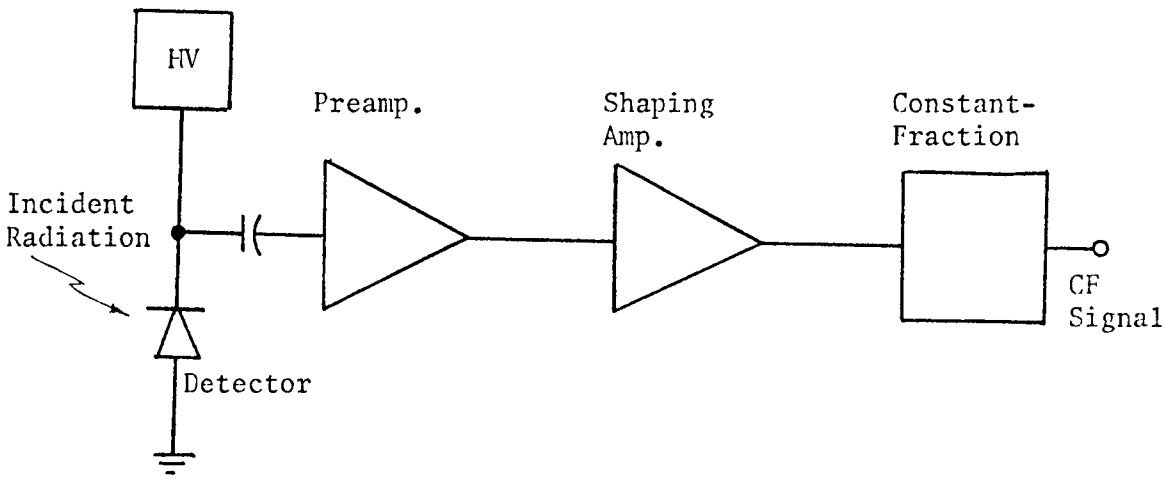


Figure 3.1. Block diagram of a signal processing system for timing with Ge(Li) detectors.

charge liberated in the detector. Timing applications usually require further amplification and shaping of the output signal from the preamplifier. In Figure 3.1 pulse shaping is accomplished by CR differentiation followed by RC integration. Differentiation effectively reduces the long decay time of the preamplifier signal to avoid signal pile-up. Integration improves the signal-to-noise ratio by reducing the high-frequency components of the noise. Timing information in this system is obtained from the shaped signal by using a constant-fraction discriminator as described in Chapter II.

To obtain a transfer function for the system in Figure 3.1, the circuit model shown in Figure 3.2 is used. The impedance of the semiconductor detector and the input impedance of the preamplifier are represented by R_d and C_d. Amplifier A_1, capacitor C_f and resistor R_f comprise the circuit model of the preamplifier. The shaping amplifier is represented by differentiator C_1 and R_1, buffer amplifier A_2, and integrator R_2 and C_2. The remainder of the circuitry in Figure 3.2 is for constant-fraction shaping. All of the amplifiers are assumed to be ideal voltage amplifiers with infinite bandwidth, infinite input impedance and zero output impedance.

The current-to-voltage transfer function of the detector and preamplifier combination in Figure 3.2 can be determined by summing the Laplace transformed currents at the input node of the system. In the s-domain this current summation is

$$I_d(s) = E_{ip}(s)\left(\frac{1}{R_d} + sC_d\right) + \left(E_{ip}(s) - E_{op}(s)\right)\left(\frac{1}{R_f} + sC_f\right) . \qquad (3.1)$$

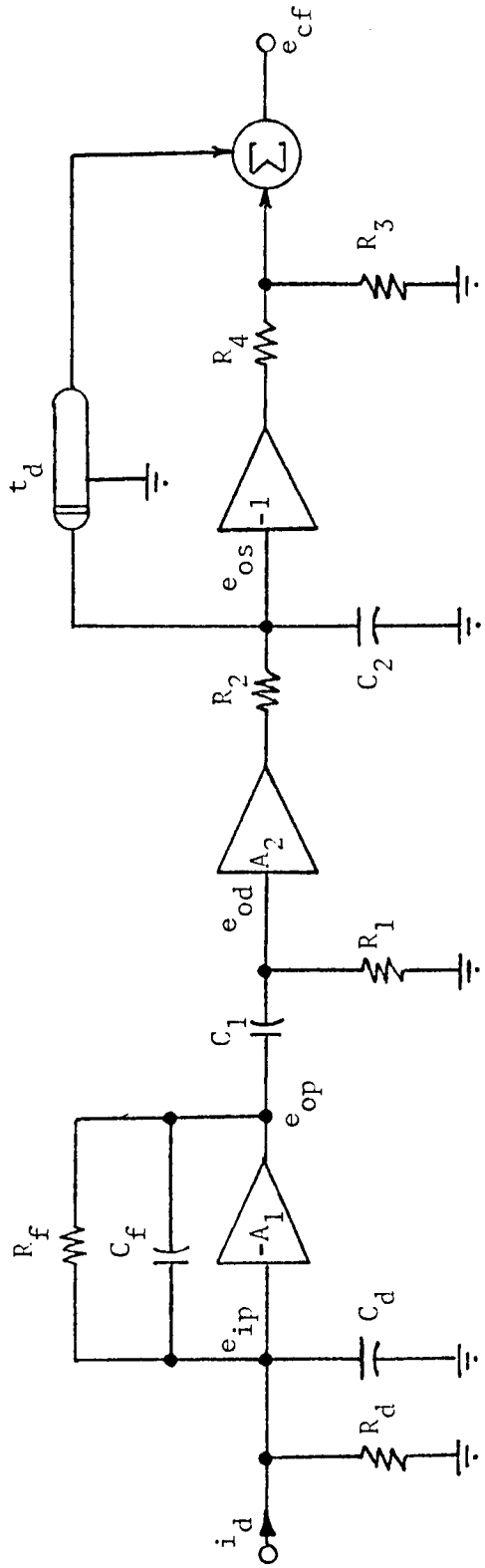


Figure 3.2. Simplified circuit model of the signal processing system.

Now the voltage transfer function of the ideal voltage amplifier A_1 is given by

$$E_{op}(s) = -A_1 E_{ip}(s) \ . \tag{3.2}$$

Combining Equations (3.1) and (3.2), the expression for the current sum is

$$I_d(s) = -\frac{E_{op}(s)}{A_1}\left[\frac{1+sC_dR_d}{R_d} + \frac{1+sC_fR_f}{R_f}\right] - E_{op}(s)\left[\frac{1+sC_fR_f}{R_f}\right] \ . \tag{3.3}$$

Rearranging terms and simplifying this equation gives

$$I_d(s) = -\frac{E_{op}(s)}{A_1R_dR_f}\left[s[C_dR_dR_f + C_fR_fR_d(1+A_1)] + R_f + R_d(1+A_1)\right] \ . \tag{3.4}$$

If the gain of amplifier A_1 satisfies the criterion

$$|A_1| >> 1 \ , \tag{3.5}$$

then the transfer impedance of the detector and preamplifier combination can be determined from Equation (3.4), and

$$\frac{E_{op}(s)}{I_d(s)} \simeq \frac{-R_f||[R_d(1+A_1)]}{s[C_f + C_d/(1+A_1)]R_f||[R_d(1+A_1)] + 1} \ . \tag{3.6}$$

Equation (3.6) can be written in the simplified form

$$\frac{E_{op}(s)}{I_d(s)} \simeq \frac{-K_p}{s\tau_p+1} = \frac{-K_p\omega_p}{s+\omega_p} \ , \tag{3.7}$$

where K_p is the dc gain of the detector and preamplifier combination, or

$$K_p \approx R_f || [R_d(1+A_1)] \ , \tag{3.8}$$

and τ_p is the dominant integration time constant of the circuit, or

$$\tau_p = \frac{1}{\omega_p} \approx \left[C_f + \frac{C_d}{1+A_1}\right] R_f || [R_d(1+A_1)] \ . \tag{3.9}$$

Voltage division can be used to find the voltage transfer function of the shaping amplifier. Referring to Figure 3.2, page 43, voltage division for the shaping amplifier yields the s-domain expression

$$E_{os}(s) = E_{op}(s) \left(\frac{R_1}{R_1+1/sC_1}\right)[A_2]\left(\frac{1/sC_2}{R_2+1/sC_2}\right) \ . \tag{3.10}$$

The transfer function of the shaping amplifier is found by rearranging terms in the preceding equation to give

$$\frac{E_{os}(s)}{E_{op}(s)} = \frac{A_2 sC_1R_1}{(sC_1R_1+1)(sC_2R_2+1)} \ . \tag{3.11}$$

Equation (3.11) can be written in the simplified form

$$\frac{E_{os}(s)}{E_{op}(s)} = \frac{A_2 s\tau_1}{(1+s\tau_1)(1+s\tau_2)} = \frac{A_2 s\omega_2}{(s+\omega_1)(s+\omega_2)} \ , \tag{3.12}$$

where τ_1 is the differentiation time constant of the shaping amplifier, or

$$\tau_1 = \frac{1}{\omega_1} = R_1 C_1 \ , \tag{3.13}$$

and τ_2 is the integration time constant, or

$$\tau_2 = \frac{1}{\omega_2} = R_2 C_2 \ . \tag{3.14}$$

The transfer function for the ideal constant-fraction circuit in Figure 3.2, page 43, can be found by time-domain analysis. Summing the attenuated, inverted signal and the delayed signal at the constant-fraction summing junction yields the bipolar timing signal as a function of time, or

$$e_{cf}(t) = -fe_{os}(t)U(t) + e_{os}(t-t_d)U(t-t_d) \ . \tag{3.15}$$

A Laplace transformation of Equation (3.15) gives

$$E_{cf}(s) = -fE_{os}(s) + E_{os}(s)\varepsilon^{-st_d} \ . \tag{3.16}$$

From this equation the transfer function of the constant-fraction circuit is

$$\frac{E_{cf}(s)}{E_{os}(s)} = \varepsilon^{-st_d} - f \ , \tag{3.17}$$

where f is the attenuation factor

$$f = \frac{R_3}{R_3+R_4} \ , \tag{3.18}$$

and t_d is the fixed shaping delay.

The response of the total system shown in Figure 3.2, page 43, is described by the system transfer function,[23] which is equal to the product of the transfer functions of its individual subsystems. Thus, from Equations (3.7), (3.12) and (3.17) the total transfer function of the timing system is the transfer impedance

$$\frac{E_{cf}(s)}{I_d(s)} = \frac{-sK_pA_2\tau_1(\epsilon^{-st_d}-f)}{(s\tau_p+1)(s\tau_1+1)(s\tau_2+1)} . \qquad (3.19)$$

Rearranging terms in this equation gives

$$\frac{E_{cf}(s)}{I_d(s)} = \frac{-sK_pA_2\omega_p\omega_2(\epsilon^{-st_d}-f)}{(s+\omega_p)(s+\omega_1)(s+\omega_2)} . \qquad (3.20)$$

Approximate Time Response of the Signal Shaping System

From Equation (3.20) the time response of the system in Figure 3.2, page 43, can be derived if an expression for the current signal i_d, from the detector, is known. The zero-crossing time for the constant-fraction signal can then be determined by setting the expression for the constant-fraction signal to zero.

Determining the signal shape for the current from a typical semiconductor detector is very difficult.[24] A first order approximation for the signal shape is an exponential;[3,24] that is,

$$i_d(t) = I\,\epsilon^{-t/T_c} , \qquad (3.21)$$

where T_c is a measure of the charge collection time in the detector. The peak detector current, I, is related to the charge Q, that is collected in the detector for a particular event; thus, the expression for current can be integrated to give the charge, or

$$Q = \int_0^\infty I\varepsilon^{-t/T_c}\, dt \ . \tag{3.22}$$

Evaluating this integral yields

$$Q = I\,T_c \ , \tag{3.23}$$

and solving for the peak current gives

$$I = \frac{Q}{T_c} \ . \tag{3.24}$$

From Equations (3.21) and (3.24) an expression for the detector current as a function of the charge collection time, T_c, can be obtained, or

$$i_d(t) = \frac{Q}{T_c}\,\varepsilon^{-t/T_c} \ . \tag{3.25}$$

A Laplace transformation of this expression for detector current yields

$$I_d(s) = \frac{Q}{sT_c+1} \ , \tag{3.26}$$

or

$$I_d(s) = \frac{Q\omega_c}{s+\omega_c} \ , \tag{3.27}$$

where

$$\omega_c = \frac{1}{T_c} . \tag{3.28}$$

Incorporating Equation (3.27) into Equation (3.20) yields the Laplace transform expression for the time response of the timing system to an exponential detector current. This s-domain expression for the constant-fraction signal is

$$E_{cf}(s) = \frac{-sK_pA_2\omega_p\omega_2\omega_c Q(\varepsilon^{-st_d}-f)}{(s+\omega_c)(s+\omega_p)(s+\omega_1)(s+\omega_2)} . \tag{3.29}$$

Heaviside's expansion theorem[23] allows Equation (3.29) to be rewritten as

$$E_{cf}(s) = (\varepsilon^{-st_d}-f)\left[\frac{B_1}{s+\omega_c} + \frac{B_2}{s+\omega_p} + \frac{B_3}{s+\omega_1} + \frac{B_4}{s+\omega_2}\right] , \tag{3.30}$$

where the constants in Equation (3.30) are defined by

$$B_1 = \frac{K_pA_2\omega_p\omega_2\omega_c^2 Q}{(\omega_p-\omega_c)(\omega_1-\omega_c)(\omega_2-\omega_c)} , \tag{3.31}$$

$$B_2 = \frac{K_pA_2\omega_p^2\omega_2\omega_c Q}{(\omega_c-\omega_p)(\omega_1-\omega_p)(\omega_2-\omega_p)} , \tag{3.32}$$

$$B_3 = \frac{K_pA_2\omega_p\omega_1\omega_2\omega_c Q}{(\omega_c-\omega_1)(\omega_p-\omega_1)(\omega_2-\omega_1)} , \tag{3.33}$$

and

$$B_4 = \frac{K_p A_2 \omega_p \omega_2^2 \omega_c Q}{(\omega_c-\omega_2)(\omega_p-\omega_2)(\omega_1-\omega_2)} \cdot \tag{3.34}$$

The time expression for the constant-fraction bipolar signal for an exponential detector current can be obtained by finding the inverse Laplace transform of Equation (3.30), or

$$e_{cf}(t) = -f\left[B_1\varepsilon^{-\omega_c t} + B_2\varepsilon^{-\omega_p t} + B_3\varepsilon^{-\omega_1 t} + B_4\varepsilon^{-\omega_2 t}\right]U(t) +$$

$$+ \left[B_1\varepsilon^{-\omega_c(t-t_d)} + B_2\varepsilon^{-\omega_p(t-t_d)} + B_3\varepsilon^{-\omega_1(t-t_d)} + B_4\varepsilon^{-\omega_2(t-t_d)}\right]U(t-t_d) \cdot \tag{3.35}$$

By setting Equation (3.35) to zero, the constant-fraction zero-crossing time can be obtained. To aid in finding an approximate solution for the crossover time, each exponential term of Equation (3.35) is replaced by the first two terms of its power series. Consequently, setting

$$e_{cf}(t_{cf}) = 0 \tag{3.36}$$

in Equation (3.35) yields

$$0 = -f\left(B_1(1-\omega_c t_{cf}) + B_2(1-\omega_p t_{cf}) + B_3(1-\omega_1 t_{cf}) + B_4(1-\omega_2 t_{cf})\right) +$$

$$+ \left(B_1[1-\omega_c(t_{cf}-t_d)] + B_2[1-\omega_p(t_{cf}-t_d)] + B_3[1-\omega_1(t_{cf}-t_d)] +\right.$$

$$\left. + B_4[1-\omega_2(t_{cf}-t_d)]\right) \cdot \tag{3.37}$$

Solving for the crossover time from this equation gives

$$t_{cf} = \frac{t_d}{1-f} + \frac{B_1 + B_2 + B_3 + B_4}{B_1\omega_c + B_2\omega_p + B_3\omega_1 + B_4\omega_2} . \qquad (3.38)$$

From this equation the approximate zero-crossing time is equal to the ARC crossover time for linear signals, from Equation (2.24), page 28, plus an error term. The error term is a function of the charge collection time, T_c, in the detector.

In the timing system shown in Figure 3.2, page 43, all gains and time constants are fixed, except the charge collection time of the semiconductor detector. Variations in the charge collection time for a Ge(Li) detector result in pulse-shape variations at the input of the constant-fraction circuit.[11,12,25] These pulse-shape variations introduce time walk of the constant-fraction crossover.[11,25] The time walk is indicated by the error term in Equation (3.38). In Ge(Li) systems, timing error due to walk of the zero-crossing is usually more dominant than timing uncertainty due to noise-induced jitter.[11]

Charge Collection Time Variations in a Ge(Li) Detector

White and McDonald,[11,12] among others,[9,13,25-27] have studied the variations in the charge collection time of Ge(Li) detectors. An interaction in the sensitive region of a detector releases a large number of hole-electron pairs which are separated and collected by the electric field present in the depleted region.[11] The Ge(Li) detector pulse shape depends on the charge transit time which is influenced by

the electric field as a function of position in the detector, by electron and hole mobilities and by the distribution of charge created by the detected radiation.[11,27] Other sources of variations in charge collection time are charge trapping due to crystal defects or impurities and the plasma effect.[11,27] The curves in Figure 3.3 illustrate the collection of charge as a function of time at seven different interaction positions for an ideal, double-open-end coaxial detector. The curves are normalized to the total charge Q, collected for events of a given energy, and to time T_{max}, representing the maximum charge collection time due to interaction near one of the electrodes.[11] This section shows that the risetimes of these curves can also represent the risetimes of the signals applied to the constant-fraction circuit.

The risetime variations of the charge curves of Figure 3.3 are representative of the risetime variations of the output signals from the charge-sensitive preamplifier in Figure 3.2, page 43. This point may be illustrated as follows. Applying the Laplace transform of an input current to the transfer function of the detector and preamplifier combination, as given by Equation (3.6), page 44, yields the s-domain expression for the preamplifier output signal as

$$E_{op}(s) = \frac{-I_d(s)R_f||[R_d(1+A_1)]}{s\left(C_f + \frac{C_d}{1+A_1}\right)R_f||[R_d(1+A_1)] + 1} \qquad (3.39)$$

The equivalent circuit represents a true integrator in the preceding equation for those frequencies that satisfy the condition

$$|s|\ \tau_p >> 1\ . \qquad (3.40)$$

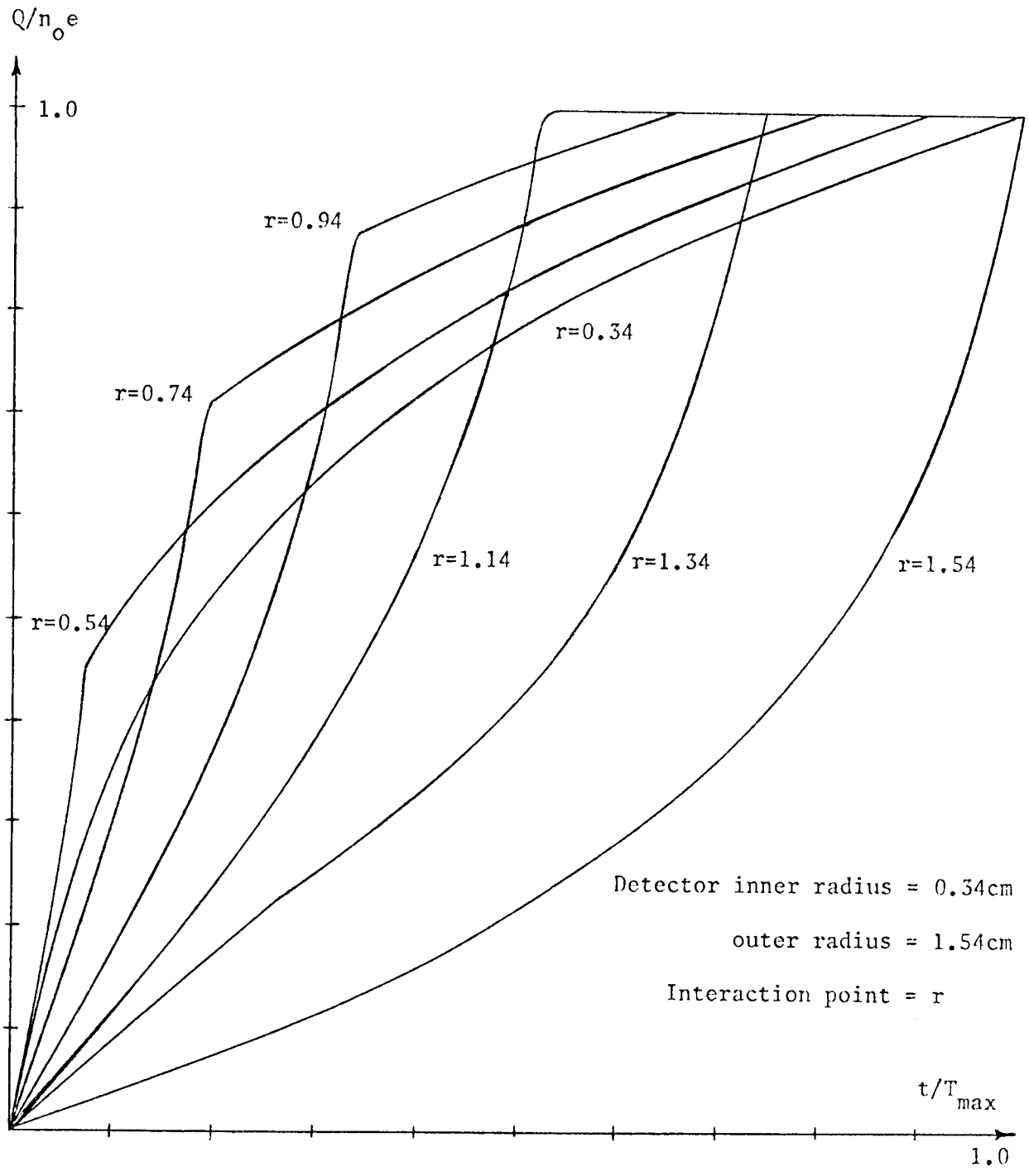


Figure 3.3. Normalized curves for charge collection as a function of time at seven interaction positions for an ideal double-open-end Ge(Li) coaxial detector. Taken from White and McDonald.[11]

Under this condition the Laplace transform of the output voltage pulse from the preamplifier becomes

$$E_{op}(s) \simeq \frac{-I_d(s)}{s\left(C_f + \frac{C_d}{1+A_1}\right)} . \tag{3.41}$$

Performing an inverse Laplace transformation on $E_{op}(s)$ yields the time domain expression for the output signal;[23] thus

$$e_{op}(t) = \frac{-1}{C_f + \frac{C_d}{1+A_1}} \int_o^t i_d(t)dt . \tag{3.42}$$

In this expression $i_d(t)$ is the time derivative of the charge collection function in the Ge(Li) detector for a particular event. Therefore, the output pulse from the preamplifier can be written as

$$e_{op}(t) = \frac{-1}{C_f + \frac{C_d}{1+A_1}} \int_o^t \frac{dq(t)}{dt} dt . \tag{3.43}$$

By evaluating the integral in the preceding equation, the expression for the output voltage pulse from the preamplifier becomes

$$e_{op}(t) = \left(\frac{-1}{C_f + \frac{C_d}{1+A_1}}\right)[q(t) - q(o)] = \frac{-q(t)}{C_f + C_d/1+A_1} . \tag{3.44}$$

The foregoing discussion indicates that the risetime variations of the output signals from the preamplifier are equivalent to the risetime variations of the charge collection curves for the Ge(Li) detector if

$$\tau_p >> T_{c(max)} \cdot \tag{3.45}$$

In this equation τ_p is the integration time constant of the detector-preamplifier circuit, and $T_{c(max)}$ is the maximum expected charge collection time of the detector.

The risetimes shown in Figure 3.3, page 53, for charge accumulation in the detector, are shown to be the same as those of the output signals of the shaping amplifier if the proper differentiation and integration time constants are chosen. A true differentiator can be described by the equation

$$e_o(t) = \frac{de_i(t)}{dt} \cdot \tag{3.46}$$

A Laplace transformation of the preceding equation yields

$$E_o(s) = sE_i(s) - E_i(0) \ , \tag{3.47}$$

where $E_i(0)$ is the initial voltage condition.[23] If $E_i(0)$ is zero, then the transfer function of a true differentiator is

$$\frac{E_o(s)}{E_i(s)} = s \ . \tag{3.48}$$

Now the transfer function of the C_1R_1 differentiator circuit in Figure 3.2, page 43, is

$$\frac{E_{od}(s)}{E_{op}(s)} = \frac{sC_1R_1}{sC_1R_1+1} \, . \tag{3.49}$$

This equation can be rewritten in the form

$$\frac{E_{od}(s)}{E_{op}(s)} = \frac{s\tau_1}{s\tau_1+1} \, , \tag{3.50}$$

where τ_1 is the differentiation time constant R_1C_1. The C_1R_1 circuit acts as a differentiator in Equation (3.50) for those frequencies that satisfy the condition

$$|s| << 1/\tau_1 \, . \tag{3.51}$$

The transfer function of the C_1R_1 circuit is approximately constant for frequencies that satisfy the condition

$$|s| >> 1/\tau_1 \, . \tag{3.52}$$

If the differentiation time constant R_1C_1 is chosen to be much greater than the maximum expected charge collection time, or

$$\tau_1 >> T_{c(max)} \, , \tag{3.53}$$

then the risetimes of the charge collection functions are preserved through the C_1R_1 differentiator. This differentiator affects only the long decay time of the output pulses from the preamplifier if the inequalities of Equations (3.45) and (3.53) are chosen so that

$$\tau_p >> \tau_1 >> T_{c(max)} \quad . \tag{3.54}$$

Following a similar argument, the pulse risetimes of the charge accumulation curves are preserved through the R_2C_2 integrator in Figure 3.2, page 43, if the integration time constant τ_2 is chosen so that

$$\tau_2 << T_{c(min)} \quad . \tag{3.55}$$

where $T_{c(min)}$ is the minimum expected charge collection time. This choice of τ_2 places the pole caused by the integration network high enough in frequency so that it does not degrade the risetimes of the fastest charge pulses. The network is still capable of reducing high-frequency noise components that degrade time resolution by increasing jitter.

In conclusion, if the time constants in the equivalent circuit in Figure 3.2 are chosen according to Equations (3.54) and (3.55), then the risetimes of the charge collection curves are the same as the risetimes of the signals applied to the constant-fraction shaping circuit. Furthermore, the shaping amplifier still has the desired effects of reducing the decay time of the preamplifier signal and of reducing the high-frequency components of noise.

A constant-fraction circuit derives timing information from the leading edge of each input signal applied to it. From the argument presented in this section, the charge collection curves in Figure 3.3, page 53, can represent the voltage waveforms at the input of the

constant-fraction circuit; therefore, the shapes of these curves are of particular importance. In the next section, three functions are chosen to represent the various shapes of the charge collection curves.

Three Representative Charge Collection Functions

Most constant-fraction discriminators employ an attenuation factor of 0.1 to 0.4, to provide timing at the point of minimum jitter on the leading edge of the input signal. Referring to Figure 3.3, page 53, three general signal shapes can be seen in the range from 0.1 to 0.4 times the maximum pulse amplitude. Many of the pulses are approximately linear at these fractions of the pulse height. The curve corresponding to r = 1.54, however, is concave upward, or its slope increases with increasing time. The curve for r = 0.34 is convex upward, or its slope decreases with increasing time.

Three functions are chosen to represent the general signal shapes described in the preceding paragraph. Plots of these functions are shown in Figure 3.4. As seen from these plots, curve $e_1(t)$ has a decreasing slope, curve $e_2(t)$ has a constant slope, and curve $e_3(t)$ has an increasing slope. In the remainder of this chapter true constant-fraction (TCF) and ARC zero-crossing times and expressions for timing jitter due to noise are derived for the functions illustrated in Figure 3.4.

The first signal shape under consideration, curve $e_1(t)$, has a decreasing slope and is described by

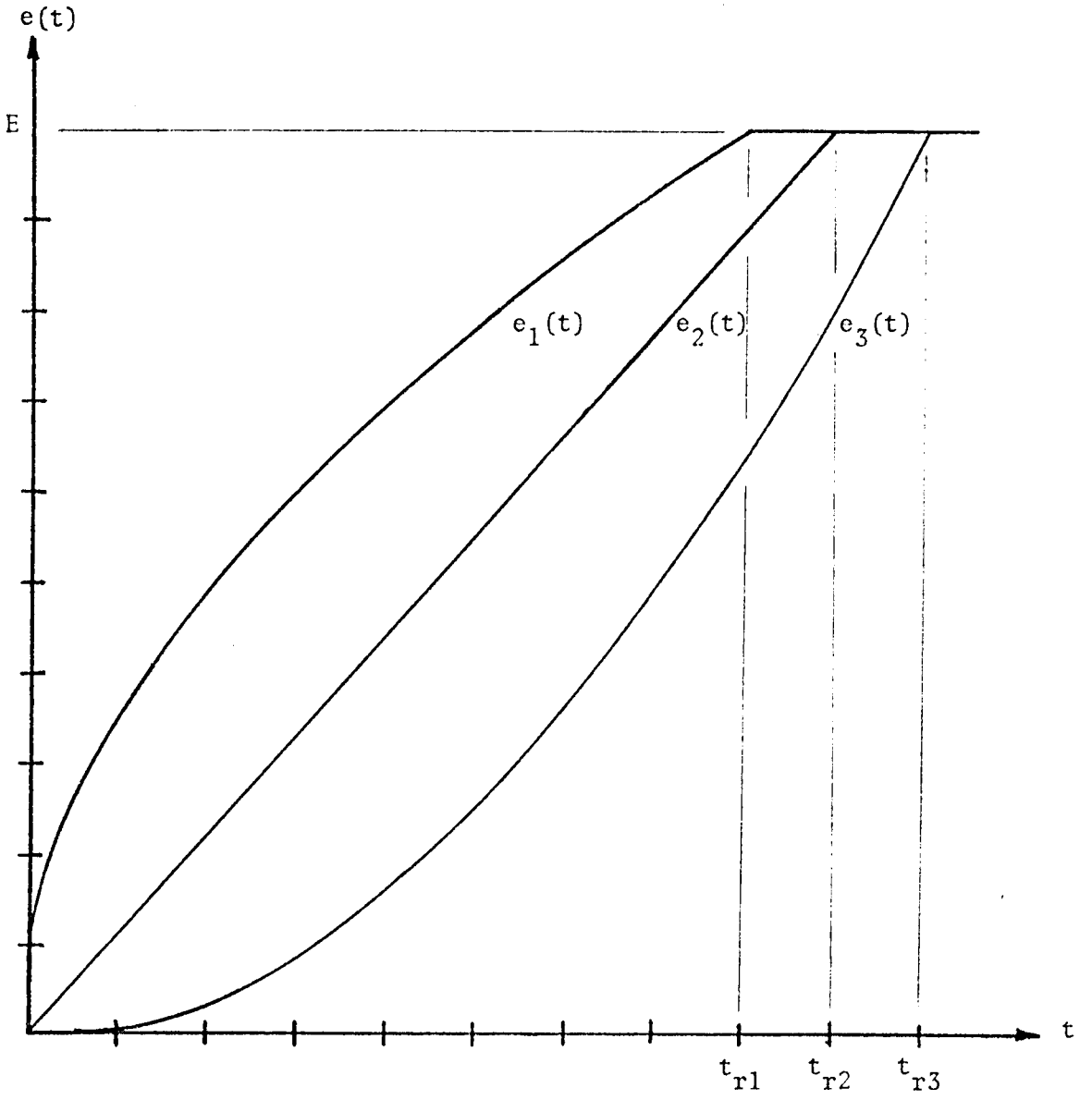


Figure 3.4. Curves representing three different charge accumulation functions for a Ge(Li) coaxial detector.

$$e_1(t) = \frac{E}{\sqrt{t_{r1}}}\sqrt{t}\,U(t) - \frac{E}{\sqrt{t_{r1}}}(\sqrt{t} - \sqrt{t_{r1}})U(t-t_{r1}) \ . \qquad (3.56)$$

From input signal $e_1(t)$, the constant-fraction circuit produces the bipolar timing pulse

$$e_{cf1}(t) = -\frac{fE}{\sqrt{t_{r1}}}\sqrt{t}\,U(t) + \frac{fE}{\sqrt{t_{r1}}}(\sqrt{t} - \sqrt{t_{r1}})U(t-t_{r1}) +$$

$$+\frac{E}{\sqrt{t_{r1}}}(\sqrt{t-t_d})U(t-t_d) - \frac{E}{\sqrt{t_{r1}}}(\sqrt{t-t_d} - \sqrt{t_{r1}})U(t-t_d-t_{r1}) \ , \qquad (3.57)$$

where f is the constant-fraction attenuation factor and t_d is the fixed shaping delay. The zero-crossing time is obtained by solving Equation (3.57) for the time at which the constant-fraction signal becomes zero.

Two cases are considered in solving for the crossover time, the TCF timing case and the ARC timing case. In the true constant-fraction (TCF) case, the zero-crossing occurs after the attenuated pulse has reached its full amplitude, or

$$t_{TCF1} > t_{r1} \ . \qquad (3.58)$$

Solving Equation (3.57) for the time at which the TCF bipolar pulse goes to zero yields

$$t_{TCF1} = t_d + f^2 t_{r1} \ . \qquad (3.59)$$

Substituting this expression for zero-crossing time into Equation (3.58)

gives a limiting condition for TCF timing with the decreasing slope input signal $e_3(t)$, or

$$t_d > (1-f^2)t_{rl(max)} , \tag{3.60}$$

where $t_{rl(max)}$ is the maximum expected risetime of input signals described by $e_3(t)$.

In the ARC timing case the zero-crossing occurs before the attenuated pulse has reached its full amplitude, or

$$t_{ARC1} < t_{rl} . \tag{3.61}$$

Setting Equation (3.57) to zero for ARC timing and solving for the time at which $e_{cf1}(t)$ becomes zero yields the crossover time

$$t_{ARC1} = \frac{t_d}{1-f^2} . \tag{3.62}$$

Substituting this expression for crossover time into Equation (3.61) yields a limiting condition for ARC timing with the decreasing slope input signal $e_3(t)$, or

$$t_d < (1-f^2)t_{rl(min)} , \tag{3.63}$$

where $t_{rl(min)}$ is the minimum expected risetime of input signals described by $e_1(t)$.

An expression for the noise-induced RMS uncertainty in the zero-crossing time for a constant-fraction signal is given in Equation (2.42), page 34, as

$$\sigma_{cf1} = \frac{E_{ncf}}{de_{cf1}(t)/dt\Big|_{t=t_{cf1}}} . \tag{3.64}$$

Now from Equations (3.57) and (3.59), the derivative of the constant-fraction signal, $e_{cf1}(t)$, at the TCF zero-crossing time is

$$\frac{de_{cf1}(t)}{dt}\Bigg|_{t=t_{TCF1}} = \frac{E}{2ft_{r1}} . \tag{3.65}$$

Therefore, for the TCF case the RMS time jitter due to noise on the decreasing slope input signal $e_1(t)$ is

$$\sigma_{TCF1} = \frac{2ft_{r1}E_{ncf}}{E} . \tag{3.66}$$

From Equations (3.57) and (3.62), the derivative of the bipolar signal $e_{cf1}(t)$ at the ARC crossover time is

$$\frac{de_{cf1}(t)}{dt}\Bigg|_{t=t_{ARC1}} = \frac{E}{2ft_{r1}}\left[(1-f^2)\sqrt{\frac{(1-f^2)t_{r1}}{t_d}}\right] . \tag{3.67}$$

Consequently, for the ARC case the RMS time jitter due to noise on the decreasing slope input signal $e_1(t)$ is

$$\sigma_{ARC1} = \frac{2ft_{r1}E_{ncf}}{E}\left[\frac{1}{(1-f^2)}\sqrt{\frac{t_d}{(1-f^2)t_{r1}}}\right] . \tag{3.68}$$

The second charge collection curve under consideration is represented by a linear function of time. Curve $e_2(t)$ in Figure 3.4, page 59, is described by the expression

$$e_2(t) = \frac{E}{t_{r2}} t\, U(t) - \frac{E}{t_{r2}} (t-t_{r2})U(t-t_{r2}) \ . \tag{3.69}$$

Constant-fraction timing for a linear input signal is considered in Chapter II. From Equations (2.20) and (2.21), pages 27 and 28, the TCF zero-crossing time due to the linear input signal $e_2(t)$ is

$$t_{TCF2} = t_d + f t_{r2} \ . \tag{3.70}$$

For the TCF timing case the fixed shaping delay must satisfy the inequality

$$t_d > (1-f) t_{r2(max)} \ , \tag{3.71}$$

where $t_{r2(max)}$ is the maximum expected risetime of input signals described by $e_2(t)$. From Equations (2.24) and (2.25), page 28, the ARC crossover time due to the linear input signal $e_2(t)$ is

$$t_{ARC2} = \frac{t_d}{1-f} \ . \tag{3.72}$$

For the ARC timing case the fixed shaping delay must satisfy the condition

$$t_d < (1-f) t_{r2(min)} \ , \tag{3.73}$$

where $t_{r2(min)}$ is the minimum expected risetime of input signals described by $e_2(t)$.

The noise-induced time jitter of the crossover point for constant-fraction timing is also derived in Chapter II for a linear input signal. From Equations (2.43) and (2.44), page 36, noise on the linear input signal $e_2(t)$ produces RMS timing jitter for TCF timing as described by

$$\sigma_{TCF2} = \frac{t_{r2}E_{ncf}}{E} \tag{3.74}$$

and RMS jitter for ARC timing as described by

$$\sigma_{ARC2} = \frac{t_{r2}E_{ncf}}{(1-f)E} \, . \tag{3.75}$$

The third charge collection curve under consideration has an increasing slope and is shown as $e_3(t)$ in Figure 3.4, page 59. This signal is described by

$$e_3(t) = \frac{Et^2U(t)}{(t_{r3})^2} - \frac{E[t^2-(t_{r3})^2]}{(t_{r3})^2} U(t-t_{r3}) \, . \tag{3.76}$$

From the input pulse $e_3(t)$, the constant-fraction circuit produces the bipolar timing signal

$$e_{cf3}(t) = \frac{E}{(t_{r3})^2} \left(-ft^2U(t) + f[t^2-(t_{r3})^2]U(t-t_{r3}) + \right.$$

$$\left. + (t-t_d)^2U(t-t_d) - [(t-t_d)^2 - (t_{r3})^2]U(t-t_d-t_{r3})\right) \, . \tag{3.77}$$

The constant-fraction zero-crossing time is obtained by solving for the time at which $e_{cf3}(t)$ in this equation becomes zero.

Two cases are considered in solving for the crossover time, the TCF timing case and the ARC timing case. In the true constant-fraction (TCF) case, the zero-crossing occurs after the attenuated pulse has reached its full amplitude, or

$$t_{TCF3} > t_{r3} \cdot \tag{3.78}$$

Solving Equation (3.77) for the time at which the TCF bipolar pulse goes to zero yields

$$t_{TCF3} = t_d + t_{r3}\sqrt{f} \cdot \tag{3.79}$$

Substituting this expression for zero-crossing time into Equation (3.78) gives a limiting condition for TCF timing with the increasing slope input signal $e_3(t)$, or

$$t_d > [t_{r3(max)}](1 - \sqrt{f}) , \tag{3.80}$$

where $t_{r3(max)}$ is the maximum expected risetime of input signals described by $e_3(t)$.

In the ARC timing case, the zero-crossing occurs before the attenuated pulse has reached its full amplitude, or

$$t_{ARC3} < t_{r3} \cdot \tag{3.81}$$

Setting Equation (3.77) to zero for ARC timing and solving for the time at which $e_{cf3}(t)$ becomes zero yields the crossover time

$$t_{ARC3} = \frac{t_d}{1 - \sqrt{f}} \cdot \tag{3.82}$$

Substituting this expression for crossover time into Equation (3.81) yields a limiting condition for ARC timing with the increasing slope input signal $e_3(t)$, or

$$t_d < [t_{r3(min)}](1 - \sqrt{f}) \ , \tag{3.83}$$

where $t_{r3(min)}$ is the minimum expected risetime of input signals described by $e_3(t)$.

A general expression for the noise-induced RMS uncertainty in the zero-crossing time for a constant-fraction signal is given in Equation (2.42), page 34, as

$$\sigma_{cf3} = E_{ncf} \left[\left. \frac{de_{cf3}(t)}{dt} \right|_{t=t_{cf3}} \right]^{-1} \cdot \tag{3.84}$$

Now from Equations (3.77) and (3.79), pages 64 and 65, the derivative of the constant-fraction signal $e_{cf3}(t)$, at the TCF zero-crossing time, is

$$\left. \frac{de_{cf3}(t)}{dt} \right|_{t=t_{TCF3}} = \frac{2E\sqrt{f}}{t_{r3}} \cdot \tag{3.85}$$

Consequently, for the TCF case the RMS time jitter due to noise on the increasing slope input signal $e_3(t)$ is

$$\sigma_{TCF3} = \frac{E_{ncf} t_{r3}}{2E\sqrt{f}} \quad . \tag{3.86}$$

From Equation (3.77) and Equation (3.82), the derivative of the bipolar pulse $e_{cf3}(t)$, at the ARC crossover time, is

$$\left.\frac{de_{cf3}(t)}{dt}\right|_{t=t_{ARC3}} = \frac{2E\sqrt{f}}{t_{r3}} \left(\frac{t_d}{t_{r3}}\right) \quad . \tag{3.87}$$

Therefore, for the ARC case the RMS time jitter due to noise on the increasing slope input signal $e_3(t)$ is

$$\sigma_{ARC3} = \frac{E_{ncf} t_{r3}}{2E\sqrt{f}} \left(\frac{t_{r3}}{t_d}\right) \quad . \tag{3.88}$$

Several observations can be made from the preceding discussion. The TCF and ARC zero-crossing times can be compared for the three selected input signal shapes. For each input signal shape, the time from zero to the crossover of the bipolar timing signal is greater for TCF timing than it is for ARC timing. This conclusion results directly from the definitions of the TCF and ARC cases.

In order to compare the crossover times among all three signal shapes the following conditions are imposed: a single value for the attenuation factor, f, is used for all three signal shapes; the value of f is chosen so that $0 < f < 1$; a single value of the shaping delay, t_d, is selected to give TCF timing with all three input signal shapes; and a different single value of t_d is chosen to give ARC timing with all three types of signals. For a given risetime such that

$$t_{r1} = t_{r2} = t_{r3} = t_r \,, \tag{3.89}$$

the TCF crossover times for the three types of input signals bear the general relationship

$$t_{TCF1} < t_{TCF2} < t_{TCF3} \,. \tag{3.90}$$

These inequalities can be obtained from Equations (3.59), (3.70) and (3.79) of this section. Under the conditions stated previously, the ARC crossover times for the three types of input signals bear the general relationship

$$t_{ARC1} < t_{ARC2} < t_{ARC3} \,. \tag{3.91}$$

These inequalities can be obtained from Equations (3.62), (3.72), and (3.82) of this section.

It is important to note that the ARC crossover time for any one of the selected input signal shapes is independent of both amplitude and risetime. However, the ARC zero-crossing time is dependent on the shape of each input signal. This shape dependency of ARC timing is a major source of error in timing with large Ge(Li) detectors.

Expressions for the noise-induced time jitter for TCF and for ARC timing are given in this section for each of the three input signal shapes. These relationships are presented to more completely describe the contribution of pulse shape to timing error for the constant-fraction technique.

Summary

A signal processing system for timing applications with Ge(Li) detectors is shown in this chapter. The system consists of a detector, a charge-sensitive preamplifier, a shaping amplifier and a constant-fraction discriminator. A simplified transfer function is derived, and an exponential detector current is used in determining the response of the system. The approximate constant-fraction zero-crossing time is derived and is shown to be independent of the amplitude of the detector current but dependent on the charge collection time of the detector.

The risetime variations of the charge collection functions for a Ge(Li) detector are shown to cause the same variations in the risetimes of the input signals to the constant-fraction discriminator, for the system considered. Three signals are chosen to represent these variations in charge collection time: a signal with a decreasing slope, a signal with a constant slope and a signal with an increasing slope. True constant-fraction (TCF) and ARC zero-crossing times are derived for these input signals. Each of the three input signal shapes results in a different TCF or ARC zero-crossing time. Expressions for the noise-induced RMS time jitter at the zero-crossing time are then derived for these input signals for TCF and ARC timing.

CHAPTER IV

REJECTION OF LEADING-EDGE SIGNALS: CRITERIA AND EFFECTS

A simplified representation of the new, third generation constant-fraction discriminator used to obtain the experimental data is shown in this chapter. A functional circuit description is also included. The double threshold circuitry in this discriminator and the optional use of Slow-Risetime-Reject (SRT) circuitry allow elimination of those timing logic signals that are produced by leading-edge timing in the instrument. Circuit criteria are derived in this chapter to insure that ARC timing and not leading-edge timing is provided by the discriminator when the SRT circuitry is employed. These criteria are established for the three representative charge collection functions described in Chapter III. The reduction in the counting efficiency of the discriminator that results from the use of the SRT circuitry is described analytically.

Discussion of Constant-Fraction Implementation

Advances in technology have allowed changes to be made in the circuitry used to implement a constant-fraction discriminator. A first generation discriminator, which used discrete components,[8] can be represented by the block diagram shown in Figure 2.7, page 24. A pulse transformer was often used for inverting the input signal. The attenuated and delayed signals were summed in a low-impedance forward-biased diode. This current summing technique is extremely nonlinear under

large signal conditions. A tunnel diode was used to detect the zero-crossing of the constant-fraction signal. Designs using these devices are often difficult to implement. In addition, characteristics of tunnel diodes can change due to temperature induced drifting of the semiconductor doping profiles.

The block diagram in Figure 4.1 illustrates a typical second generation constant-fraction discriminator, implemented with MECL II emitter-coupled logic circuitry.[10,28] A constant-fraction signal and a leading-edge signal are generated simultaneously by identical MECL II line receivers. The leading-edge signal arms a MECL II AND gate, which acts as a zero-crossing detector for the constant-fraction bipolar pulse. The logic pulse from the zero-crossing detector then triggers a monostable multivibrator, which blocks the logic circuitry for a time period comparable to the width of the input signal. Standardized output logic pulses are shaped from the leading edge of the blocking one-shot pulse.

Leading-edge timing can be produced by the discriminator shown in Figure 4.1, and significant timing error due to walk is thus introduced. Leading-edge timing can be introduced at the zero-crossing AND gate by input pulses that have exceptionally long risetimes or by input pulses that have amplitudes only slightly exceeding the threshold level of the instrument. These input pulses may cross the threshold of the leading-edge arming discriminator after the zero-crossing time of the bipolar timing signal. For these types of input pulses the leading-edge and constant-fraction signals exchange roles at the zero-crossing gate. Thus, the constant-fraction signal arms the AND gate for the detection of the

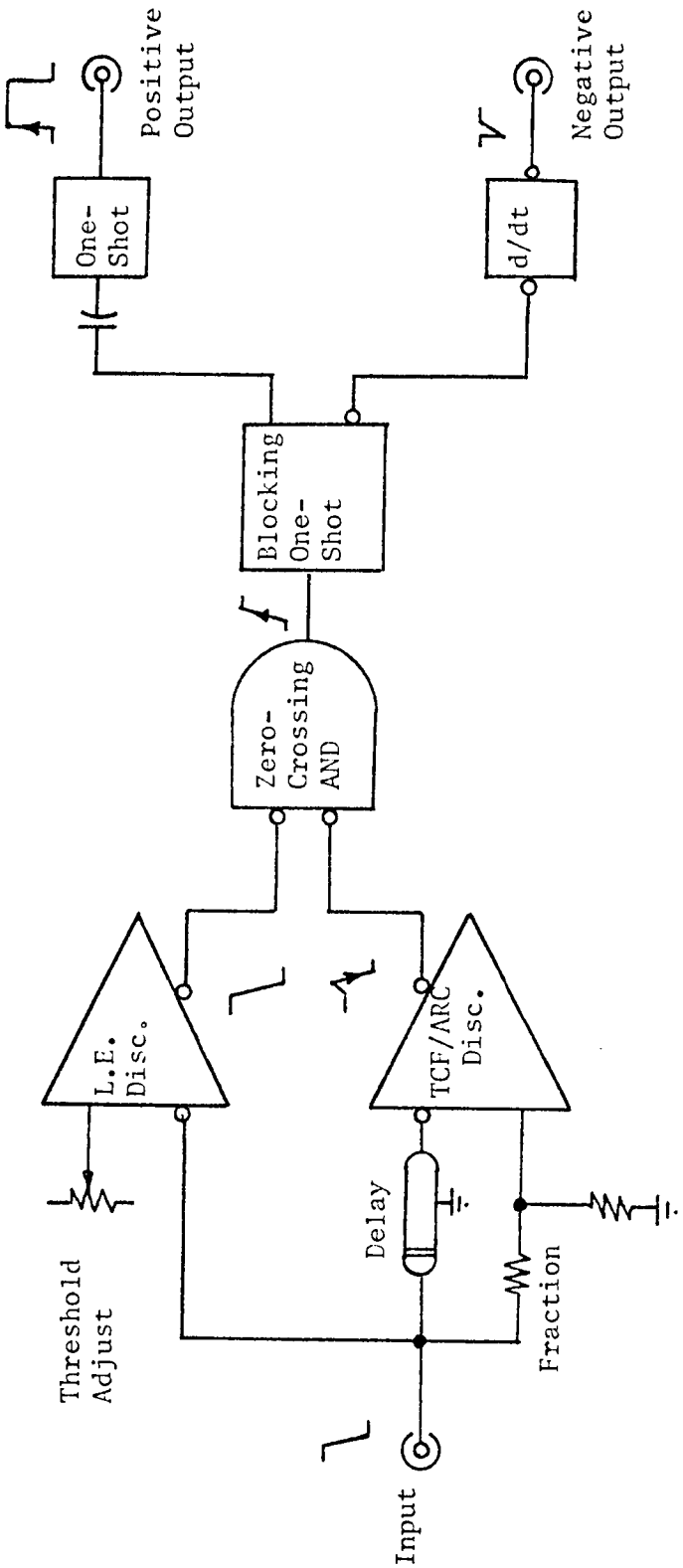


Figure 4.1. Typical second generation constant-fraction discriminator, implemented with MECL II emitter-coupled logic.

leading-edge signal, and timing error due to leading-edge time slewing results.

A third generation constant-fraction discriminator contains circuitry that can be used to eliminate those logic signals that are caused by leading-edge timing.[29] This discriminator was developed in 1974 and is illustrated by a simplified block diagram in Figure 4.2. A circuit diagram of the essential logic components of this discriminator and an accompanying circuit description are presented in Chapter V. The unit is implemented with integrated circuits of the MECL 10,000 emitter-coupled logic series. As in the second generation unit, a leading-edge signal and a constant-fraction bipolar signal are generated simultaneously by identical ECL line receivers. The leading-edge signal arms the ECL AND gate G1, which acts as a zero-crossing detector for the constant-fraction bipolar pulse. However, in the third generation instrument the threshold of the lower-level leading-edge (LLLE) arming discriminator is automatically set at one-half the threshold level required to produce an output pulse from the instrument. This arming technique insures that signals which reach the threshold level of interest exceed the threshold of the arming discriminator by at least a factor of two. Leading-edge walk introduced at the zero-crossing gate is thereby significantly reduced, relative to the arming technique used in the second generation unit.

The threshold for an upper-level leading-edge (ULLE) discriminator determines the minimum input signal amplitude required to produce an output pulse from the instrument. The signal from this leading-edge

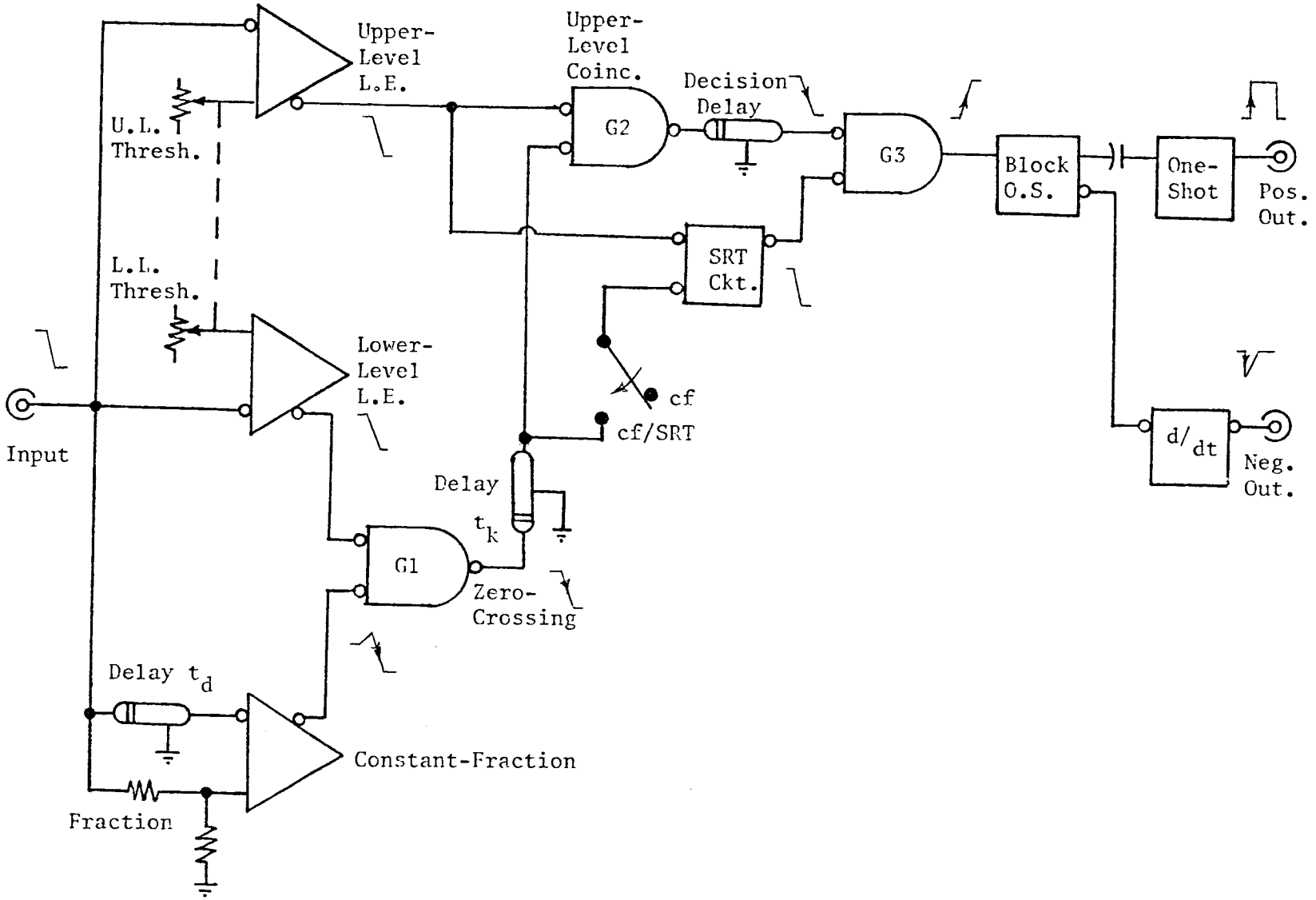


Figure 4.2. Block diagram of a third generation constant-fraction discriminator with double threshold and Slow-Risetime-Reject circuitry; implemented with MECL 10,000 logic.

discriminator arms the ECL AND gate G2, for the detection of the delayed timing logic pulse from the zero-crossing gate, G1.

For input signals that have exceptionally long risetimes or for input signals that have amplitudes only slightly exceeding the instrument threshold, the signal from the ULLE discriminator and the delayed timing logic pulse can exchange roles at AND gate G2. This situation would cause leading-edge timing to be introduced at G2. In the Slow-Risetime-Reject (SRT) mode, the output signal from G2 is delayed while the signal from the ULLE discriminator and the delayed timing logic pulse from G1 are evaluated. The signal from AND gate G2 is accepted and processed if the signal from the upper-level discriminator arrived at the input of the AND gate before the delayed timing logic pulse arrived. Thus, a timing pulse can be rejected if the input signal from which it is derived did not cross the threshold of the upper-level discriminator within a fixed time, t_k, after the TCF or ARC zero-crossing time. Time t_k is the fixed delay in the path of the logic pulse produced at the output of the zero-crossing gate. Further processing circuitry for a signal that is accepted includes a blocking monostable multivibrator and circuitry to shape the output signals.

Circuit Delay Criteria

The output signal from an AND gate is dependent in time on the last true input signal that is applied to it. In the instrument depicted in Figure 4.2, page 74, there are two AND gates in the circuit at which timing error due to leading-edge walk can be produced, zero-crossing gate G1 and upper-level coincidence gate G2. Circuit delay criteria are

derived in this section to allow the Slow-Risetime-Reject (SRT) circuitry in the third generation discriminator to eliminate logic signals resulting from leading-edge timing.

To insure TCF or ARC timing from gate G1, the arming signal from the LLLE discriminator must arrive at the input to gate G1 before the bipolar timing pulse crosses the logic threshold of the gate. In other words, the input signal must rise from zero to the threshold level of the LLLE discriminator in a time less than the zero-crossing time of the bipolar timing pulse, or

$$t_{LL} < t_{cf} \cdot \tag{4.1}$$

Similarly the input signal must meet the constraint in Equation (4.1) and must rise from zero to the threshold level of the ULLE discriminator in a time less than the zero-crossing time plus the fixed delay time t_k, or

$$t_{UL} < t_{cf} + t_k \cdot \tag{4.2}$$

This criterion insures that leading-edge walk is not introduced at gate G2 by the signal from the ULLE discriminator.

If all input signals meet the criteria of Equations (4.1) and (4.2), leading-edge timing will not be introduced at either gate G1 or gate G2. Signals with very long risetimes, such as those from Ge(Li) detectors (20 nsec. to 200 nsec.), often violate these criteria. In such cases leading-edge walk can be introduced at the zero-crossing gate, G1, and at the upper-level coincidence gate, G2. Both of the input signal

conditions described in this paragraph are illustrated in Figure 4.3. This illustration is a partial timing diagram for ARC timing with linear signals and for the constant-fraction discriminator depicted in Figure 4.2, page 74. The input signal A satisfies both the lower-level and the upper-level constraints of Equations (4.1) and (4.2). Thus, the signals applied to gates G1 and G2 occur in the proper sequences, and the output logic pulse is produced by ARC timing. The input signal B, in this figure, violates both the lower-level and the upper-level criteria of Equations (4.1) and (4.2). Consequently, both gate G1 and gate G2 are armed in the improper sequence, and leading-edge timing is produced at both gates. If the SRT circuitry were employed, signal B would produce no output pulse.

For the decreasing slope, constant slope and increasing slope charge collection functions, $e_1(t)$, $e_2(t)$ and $e_3(t)$, respectively, the delay time t_k can be chosen to insure that input signals that cross the upper-level threshold of the instrument and cause leading-edge walk at gate G1 also cause leading-edge walk at gate G2. Now the leading-edge timing signals from G2 can be eliminated by the Slow-Risetime-Reject (SRT) circuitry. Consequently, all timing logic signals resulting from input signals described by $e_1(t)$, $e_2(t)$ or $e_3(t)$ that cross the upper-level threshold and produce leading-edge timing at either gate G1 or gate G2 can be eliminated. In the remainder of this section, criteria are established for the fixed delay time t_k. These criteria insure that the SRT circuitry can be used to eliminate logic signals resulting from leading-edge timing.

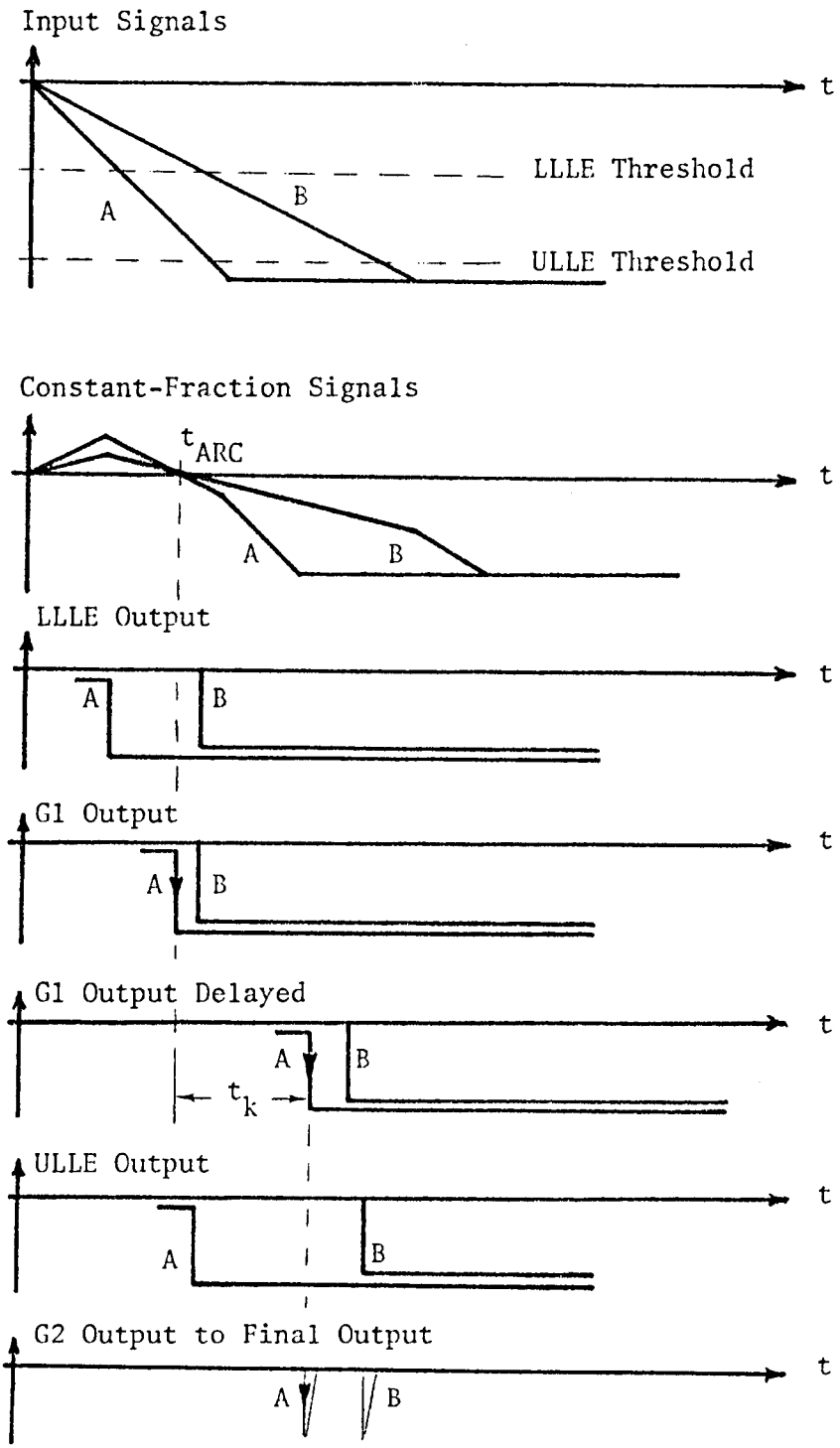


Figure 4.3. Timing diagram for the third generation constant-fraction discriminator operating in the ARC mode with linear signals.

From Chapter III, the first charge accumulation function is chosen to represent a charge collection curve with a decreasing slope. From Equation (3.56), page 60, this input signal to the constant-fraction discriminator is

$$e_1(t) = \frac{E}{\sqrt{t_{r1}}}\sqrt{t}\,U(t) - \frac{E}{\sqrt{t_{r1}}}(\sqrt{t} - \sqrt{t_{r1}})U(t-t_{r1}) \quad . \tag{4.3}$$

The TCF and ARC zero-crossing times due to the decreasing slope input signal $e_1(t)$ are, respectively,

$$t_{TCF1} = t_d + f^2 t_{r1} \tag{4.4}$$

and

$$t_{ARC1} = \frac{t_d}{1-f^2} \quad , \tag{4.5}$$

from Equation (3.59), page 60, and Equation (3.62), page 61. The time from zero to the upper-level threshold for $e_1(t)$ can be found by setting Equation (4.3) equal to the threshold voltage for the upper-level discriminator. Solving for the time at which $e_1(t)$ crosses the upper-level threshold yields

$$t_{UL1} = t_{r1}\left(\frac{E_{th}}{E}\right)^2 \quad . \tag{4.6}$$

Since the LLLE threshold is half the ULLE threshold, then the time from zero to the crossing of the lower-level threshold for $e_1(t)$ can be obtained from the preceding equation, or

$$t_{LL1} = t_{r1}\left(\frac{E_{th}}{2E}\right)^2 = \frac{t_{UL1}}{4} . \tag{4.7}$$

Equations (4.4) through (4.7) are used to establish criteria for the fixed delay t_{k1}, for $e_1(t)$.

Referring to Equation (4.1), page 76, the decreasing slope input signal, $e_1(t)$, produces TCF or ARC timing and not leading-edge timing at zero-crossing gate G1, if it crosses the LLLE threshold before the zero-crossing of the bipolar timing signal; thus

$$t_{LL1} < t_{cf1} . \tag{4.8}$$

Incorporating Equation (4.7) and Equation (4.4) or (4.5), respectively, into Equation (4.8) yields the following inequalities: for TCF timing with $e_1(t)$,

$$t_{r1}\left(\frac{E_{th}}{2E}\right)^2 < t_d + f^2 t_{r1}; \tag{4.9}$$

and for ARC timing with $e_1(t)$,

$$t_{r1}\left(\frac{E_{th}}{2E}\right)^2 < \frac{t_d}{1-f^2} . \tag{4.10}$$

Rearranging the terms in Equations (4.9) and (4.10) restates the lower-level constraints for the decreasing slope input signal as

$$t_{r1}\left(\frac{E_{th}}{E}\right)^2 < 4(t_d + f^2 t_{r1}) \tag{4.11}$$

for TCF timing and as

$$t_{r1}\left(\frac{E_{th}}{E}\right)^2 < \frac{4t_d}{1-f^2} \tag{4.12}$$

for ARC timing. A decreasing slope input signal described by $e_1(t)$ that meets the constraints expressed in Equations (4.8) through (4.12) does not introduce leading-edge timing at the zero-crossing gate, G1.

Referring to Equation (4.2), page 76, the decreasing slope input signal $e_1(t)$ does not introduce leading-edge timing at gate G2, if it crosses the upper-level threshold in a time less than the zero-crossing time plus the fixed delay time t_{k1}; thus,

$$t_{UL1} < t_{cf1} + t_{k1} \cdot \tag{4.13}$$

This expression presupposes that $e_1(t)$ also meets the conditions of Equations (4.11) and (4.12). Incorporating Equation (4.6) and Equation (4.4) or (4.5), respectively, into Equation (4.13) yields the following upper-level constraints: for TCF timing with $e_1(t)$,

$$t_{r1}\left(\frac{E_{th}}{E}\right)^2 < t_d + f^2 t_{r1} + t_{k1} , \tag{4.14}$$

and for ARC timing with $e_1(t)$,

$$t_{r1}\left(\frac{E_{th}}{E}\right)^2 < \frac{t_d}{1-f^2} + t_{k1} \cdot \tag{4.15}$$

A decreasing slope input signal described by $e_1(t)$ that meets the

constraints of Equations (4.11), (4.12), (4.14) and (4.15) does not introduce leading-edge timing at the upper-level coincidence gate, G2.

If leading-edge timing signals are to be eliminated by the SRT circuitry, then decreasing slope input signals that result in leading-edge timing at gate G1 must also produce leading-edge timing at gate G2. The upper-level constraints in Equations (4.14) and (4.15) must, therefore, be more restrictive than the lower-level constraints of Equations (4.11) and (4.12). These conditions can be combined to yield constraints for the fixed delay t_{k1}. For TCF timing the combined conditions yield

$$t_d + f^2 t_{r1(min)} + t_{k1} < 4[t_d + f^2 t_{r1(min)}] \cdot \tag{4.16}$$

Simplifying this expression gives

$$t_{k1} < 3[t_d + f^2 t_{r1(min)}] \tag{4.17}$$

or

$$t_{k1} < 3t_{TCF1(min)} \cdot \tag{4.18}$$

Note that $t_{r1(min)}$ is the minimum expected risetime for signals described by $e_1(t)$. For ARC timing, combining the upper-level and lower-level constraints yields

$$\frac{t_d}{1-f^2} + t_{k1} < \frac{4t_d}{1-f^2} \cdot \tag{4.19}$$

Simplifying this expression gives

$$t_{k1} < \frac{3t_d}{1-f^2} \tag{4.20}$$

or

$$t_{k1} < 3t_{ARC1} \ . \tag{4.21}$$

Equations (4.16) through (4.21) guarantee that all of the decreasing slope input signals described by $e_1(t)$ that cross the upper-level threshold and cause leading-edge timing at gate G1 also produce leading-edge timing at G2. Since leading-edge timing signals introduced at G2 can be eliminated, then all leading-edge timing pulses due to input signals described by $e_1(t)$ can be eliminated by the SRT circuitry.

The second charge collection function chosen in Chapter III is linear. From Equation (3.69), page 63, this input pulse to the constant-fraction discriminator is described by

$$e_2(t) = \frac{Et}{t_{r2}} U(t) - \frac{E}{t_{r2}} (t-t_{r2})U(t-t_{r2}) \ . \tag{4.22}$$

The TCF and ARC zero-crossing times due to the linear input signal $e_2(t)$ are, respectively,

$$t_{TCF2} = t_d + ft_{r2} \tag{4.23}$$

and

$$t_{ARC2} = \frac{t_d}{1-f} \ , \tag{4.24}$$

from Equations (3.70) and (3.72), page 63. For $e_2(t)$ the time from zero

to the threshold level for the upper-level discriminator can be found by setting Equation (4.22) equal to the threshold voltage. Solving for the crossing time of the upper-level threshold yields

$$t_{UL2} = \frac{E_{th}}{E} t_{r2} \cdot \tag{4.25}$$

Since the threshold of the LLLE discriminator is half the threshold for the upper-level discriminator, then the time from zero to the lower-level threshold for $e_2(t)$ can be obtained from the preceding equation, or

$$t_{LL2} = \frac{E_{th} t_{r2}}{2E} = \frac{t_{UL2}}{2} \cdot \tag{4.26}$$

Equations (4.23) through (4.26) are used in establishing criteria for the fixed delay t_{k2}, for $e_2(t)$.

The linear input signal $e_2(t)$ produces TCF or ARC timing and not leading-edge timing at zero-crossing gate G1, if it crosses the lower-level threshold before the zero-crossing of the bipolar timing pulse, or

$$t_{LL2} < t_{cf2} \cdot \tag{4.27}$$

Incorporating Equation (4.26) and Equation (4.23) or (4.24), respectively, into Equation (4.27) yields the following inequalities: for TCF timing with $e_2(t)$,

$$\frac{E_{th} t_{r2}}{2E} < t_d + f t_{r2} \; ; \tag{4.28}$$

and for ARC timing with $e_2(t)$,

$$\frac{E_{th}t_{r2}}{2E} < \frac{t_d}{1-f} \cdot \tag{4.29}$$

Rearranging the terms in Equations (4.28) and (4.29) restates the lower-level constraints for the linear input signal as

$$\frac{E_{th}t_{r2}}{E} < 2(t_d + ft_{r2}) \tag{4.30}$$

for TCF timing and as

$$\frac{E_{th}t_{r2}}{E} < \frac{2t_d}{1-f} \tag{4.31}$$

for ARC timing. A linear input signal described by $e_2(t)$ that meets the constraints expressed in Equations (4.30) and (4.31) does not introduce leading-edge timing at the zero-crossing gate, G1.

Referring to Equation (4.2), page 76, the linear input signal $e_2(t)$ does not introduce leading-edge timing at gate G2, if it crosses the upper-level threshold in a time less than the zero-crossing time plus the fixed delay time t_{k2}; thus,

$$t_{UL2} < t_{cf2} + t_{k2} \cdot \tag{4.32}$$

This expression presupposes that $e_2(t)$ also meets the conditions of Equations (4.30) and (4.31). Including Equation (4.25) and Equation (4.23) or (4.24), respectively, in Equation (4.32) yields the following

inequalities to insure that leading-edge timing is not introduced at gate G2 by $e_2(t)$: for TCF timing

$$\frac{E_{th}t_{r2}}{E} < t_d + ft_{r2} + t_{k2} \; ; \tag{4.33}$$

and for ARC timing

$$\frac{E_{th}t_{r2}}{E} < \frac{t_d}{1-f} + t_{k2} \; . \tag{4.34}$$

If all leading-edge timing signals are to be eliminated by the SRT circuitry, then linear input signals described by $e_2(t)$ that cross the upper-level threshold and that do result in leading-edge timing at G1 must also produce leading-edge timing at G2. The upper-level constraints in Equations (4.33) and (4.34) must, therefore, be more restrictive than the lower-level constraints of Equations (4.30) and (4.31). These conditions can be combined to yield the following constraints on the fixed delay t_{k2}. For TCF timing the combined conditions give

$$t_d + ft_{r2(min)} + t_{k2} < 2[t_d + ft_{r2(min)}] \; . \tag{4.35}$$

Simplifying this expression gives

$$t_{k2} < t_d + ft_{r2(min)} \tag{4.36}$$

or

$$t_{k2} < t_{TCF2(min)} \; , \tag{4.37}$$

where $t_{r2(min)}$ is the minimum expected risetime of an input signal

described by $e_2(t)$. For ARC timing, combining the upper-level and lower-level constraints yields

$$\frac{t_d}{1-f} + t_{k2} < \frac{2t_d}{1-f} . \tag{4.38}$$

Simplifying this expression gives

$$t_{k2} < \frac{t_d}{1-f} \tag{4.39}$$

or

$$t_{k2} < t_{ARC2} . \tag{4.40}$$

Equations (4.35) through (4.40) guarantee that all of the linear input signals described by $e_2(t)$ that cross the upper-level threshold and cause leading-edge timing at the zero-crossing gate, G1, also produce leading-edge timing at the upper-level coincidence gate, G2. Since leading-edge timing signals introduced at G2 can be eliminated, then all leading-edge timing pulses due to input signals described by $e_2(t)$ can be eliminated by the SRT circuitry.

The third representative charge collection function chosen in Chapter III has an increasing slope. From Equation (3.76), page 64, this input pulse to the constant-fraction discriminator is

$$e_3(t) = \frac{Et^2U(t)}{(t_{r3})^2} - \frac{E}{(t_{r3})^2}[t^2-(t_{r3})^2]U(t-t_{r3}) . \tag{4.41}$$

The TCF and ARC zero-crossing times due to the increasing slope input signal $e_3(t)$ are, respectively,

$$t_{TCF3} = t_d + t_{r3}\sqrt{f} \tag{4.42}$$

and

$$t_{ARC3} = \frac{t_d}{1-\sqrt{f}}, \tag{4.43}$$

from Equation (3.79), page 65, and Equation (3.82), page 66. The time from zero to the threshold level of the upper-level discriminator for $e_3(t)$ can be found by setting Equation (4.41) equal to the threshold voltage. Solving for the crossing time of the upper-level threshold yields

$$t_{UL3} = t_{r3}\sqrt{\frac{E_{th}}{E}}. \tag{4.44}$$

Since the threshold level of the LLLE discriminator is half the upper-level threshold, then the time from zero to the lower-level threshold for $e_3(t)$ can be obtained from the preceding equation, or

$$t_{LL3} = t_{r3}\sqrt{\frac{E_{th}}{2E}} = \frac{t_{UL3}}{\sqrt{2}}. \tag{4.45}$$

Equations (4.42) through (4.45) are used in determining criteria for the fixed delay t_{k3}, for $e_3(t)$.

Referring to Equation (4.1), page 76, the increasing slope input signal $e_3(t)$ produces TCF or ARC timing and not leading-edge timing at the zero-crossing gate, G1, if it crosses the lower-level threshold before the zero-crossing of the bipolar timing pulse, or

$$t_{LL3} < t_{cf3} \cdot \tag{4.46}$$

Incorporating Equation (4.45) and Equation (4.42) or (4.43), respectively, into Equation (4.46) yields the following inequalities: for TCF timing with $e_3(t)$,

$$t_{r3}\sqrt{\frac{E_{th}}{2E}} < t_d + t_{r3}\sqrt{f} \; ; \tag{4.47}$$

and for ARC timing with $e_3(t)$,

$$t_{r3}\sqrt{\frac{E_{th}}{2E}} < \frac{t_d}{1-\sqrt{f}} \cdot \tag{4.48}$$

An increasing slope input signal described by $e_3(t)$ that meets the constraints given in Equations (4.47) and (4.48) does not introduce leading-edge timing at the zero-crossing gate, G1.

Referring to Equation (4.2), page 76, the input signal $e_3(t)$ does not introduce leading-edge walk at gate G2, if it crosses the upper-level threshold in a time less than the zero-crossing time plus the fixed delay time t_{k3}, or

$$t_{UL3} < t_{cf3} + t_{k3} \cdot \tag{4.49}$$

This relationship presupposes that $e_3(t)$ also meets the conditions of Equations (4.47) and (4.48). Including Equation (4.44) and Equation (4.42) or (4.43), respectively, in Equation (4.49) yields the following inequalities to insure that leading-edge walk is not introduced at gate G2 by $e_3(t)$: for TCF timing

$$t_{r3}\sqrt{\frac{E_{th}}{E}} < t_d + t_{r3}\sqrt{f} + t_{k3} \; ; \tag{4.50}$$

and for ARC timing

$$t_{r3}\sqrt{\frac{E_{th}}{E}} < \frac{t_d}{1-\sqrt{f}} + t_{k3} \; . \tag{4.51}$$

An argument similar to the one leading to Equation (4.36), page 86, and Equation (4.39), page 87, may be made. If t_{k3} is chosen properly, increasing slope input signals described by $e_3(t)$ that cross the upper-level threshold and that result in leading-edge timing at the zero-crossing gate, G1, also cause time slewing at the upper-level coincidence gate, G2. For TCF timing the delay time t_{k3} should be chosen so that

$$t_{k3} < (\sqrt{2} - 1)[t_d + t_{r3(min)}\sqrt{f}] \; , \tag{4.52}$$

or

$$t_{k3} < (\sqrt{2} - 1)t_{TCF3(min)} \; . \tag{4.53}$$

For ARC timing the delay time should be

$$t_{k3} < \frac{(\sqrt{2} - 1)t_d}{1 - \sqrt{f}} \; , \tag{4.54}$$

or

$$t_{k3} < (\sqrt{2} - 1)t_{ARC3} \; . \tag{4.55}$$

Thus, all leading-edge timing signals produced by increasing slope input signals that can be described by $e_3(t)$ can be rejected by the SRT circuitry.

The fixed circuit delay t_k, for the discriminator shown in Figure 4.2, page 74, can be chosen so that the Slow-Risetime-Reject circuitry can be used to block leading-edge timing pulses from reaching the output of the instrument. The limiting criteria are given in this section for the three charge collection functions $e_1(t)$, $e_2(t)$ and $e_3(t)$, chosen in Chapter III. The various criteria for t_k can be compared and a single value of t_k can be chosen to satisfy all of these conditions. In order to compare the limiting criteria for selecting t_k for all three signal shapes, the following conditions are imposed: a single value for the attenuation factor, f, is chosen such that $0 < f < 1$; a single value of the shaping delay, t_d, is selected to give TCF timing with all three signal shapes; and a different, single value of t_d is selected to give ARC timing with all three types of signals. These conditions imply that the minimum risetimes are the same for all three signal shapes, or

$$t_{r1(min)} = t_{r2(min)} = t_{r3(min)} = t_{r(min)} , \qquad (4.56)$$

and that the maximum risetimes are the same for all three types of signals, or

$$t_{r1(max)} = t_{r2(max)} = t_{r3(max)} = t_{r(max)} . \qquad (4.57)$$

For each input signal shape the maximum acceptable value for the delay t_k is less for ARC timing than it is for TCF timing. This conclusion results from applying the definitions for the TCF and ARC cases directly to the criteria given in Equations (4.18) and (4.21), in Equations (4.37) and (4.40), and in Equations (4.53) and (4.55). Thus

the single, maximum acceptable value for t_k must be selected from among the criteria used for ARC timing with the three input signals $e_1(t)$, $e_2(t)$ and $e_3(t)$. By comparing Equations (4.20), (4.39) and (4.54) under the conditions presented in the preceding paragraph, the largest acceptable value for t_k is found to be

$$t_k < \frac{(\sqrt{2}-1)t_d}{1-\sqrt{f}} . \tag{4.58}$$

This limit for t_k corresponds to the limit for the fixed delay t_{k3}, established for ARC timing with the increasing slope signal $e_3(t)$.

In conclusion, the maximum value of the fixed delay t_k, for the discriminator shown in Figure 4.2, page 74, should be chosen according to Equation (4.58). This constraint insures that an input signal described by $e_1(t)$, $e_2(t)$ or $e_3(t)$ that crosses the upper-level threshold of the instrument and causes leading-edge timing at gate G1 also causes leading-edge timing at gate G2. Thus, the SRT circuitry can be employed to reject those pulses caused by leading-edge timing for the decreasing slope, constant slope and increasing slope input signals.

Effects of Slow-Risetime-Reject on Energy Information

The previous section indicates that timing with Ge(Li) detectors can be improved by eliminating those logic signals resulting from leading-edge timing. This improvement in timing information is made at the expense of the counting efficiency of the timing system. Some signals that meet the minimum energy threshold criterion of the discriminator

are rejected due to risetime. This section is an examination of the effects of the Slow-Risetime-Reject circuit on energy information. These effects are described for a random process.

Consider the random input signals to the constant-fraction discriminator in the Ge(Li) timing system described in Chapter III. The amplitude of each input signal is proportional to the energy of the detected radiation. The risetime of each input signal is shown in Chapter III to be equal to the charge collection time in the detector for that event.

Let the input signals to the discriminator range in amplitude from zero to some value E_v. In the simplest case these signals are random in amplitude with no preferred value between zero and E_v. The probability of the amplitude of an input pulse for a particular nuclear event can be described in general by a probability density function. For the case in which there is no preferred value, the probability density function, p(e), for input pulse heights is uniform and can be described by

$$p(e) = \begin{cases} \frac{1}{E_v}, & 0 < e < E_v \\ 0, & \text{elsewhere} \end{cases} . \qquad (4.59)$$

In general, the probability that the amplitude of an input signal to the constant-fraction circuit lies in the range from E_1 to E_2 is described by a probability distribution function, which is the integral of the density function; thus,

$$P(E_1 < e < E_2) = \int_{E_1}^{E_2} p(e)de \ . \tag{4.60}$$

Furthermore, the total area under the p(e) curve must be unity;[21] thus,

$$\int_{-\infty}^{\infty} p(e)de = \int_{0}^{E_v} \frac{1}{E_v} de = 1 \ . \tag{4.61}$$

Input signals to the discriminator in the timing system for Ge(Li) detectors vary widely in risetimes. In the simple example being considered, the risetimes of these signals are random and range in value from T_r to mT_r, with no preferred value. The constant m is positive and is greater than unity. If the risetime of an input signal is assumed to be independent of the energy of the detected radiation, then a uniform probability density function describes the probability of the risetime for a particular input pulse; therefore

$$p(t_r) = \begin{cases} \frac{1}{(m-1)T_r} , & T_r < t_r < mT_r \\ 0 , & \text{elsewhere} \end{cases} . \tag{4.62}$$

The probability distribution function for pulse risetimes is the integral of the density function, or

$$P(T_1) = \int_{-\infty}^{T_1} p(t_r)dt_r \ . \tag{4.63}$$

This equation describes the probability that the risetime of an input

signal to the constant-fraction discriminator is less than T_1. The integral of the density function over the entire range of risetimes is unity; thus,

$$\int_{-\infty}^{\infty} p(t_r)dt_r = \int_{T_r}^{mT_r} \frac{1}{(m-1)T_r} dt_r = 1 . \qquad (4.64)$$

The random nature of both amplitudes and risetimes of the input signals to the constant-fraction unit is described by a joint probability distribution function, or

$$P(E_1,T_1) = \int_{-\infty}^{E_1} \int_{-\infty}^{T_1} p(e,t_r)dt_r de . \qquad (4.65)$$

This distribution is the probability that an input signal to the discriminator has an amplitude less than E_1 and a risetime less than T_1. In the example under consideration, the probability density functions for pulse amplitudes and risetimes are assumed to be independent. The joint probability density function in Equation (4.65) can therefore be expressed as the product of the individual density equations;[21] thus,

$$P(E_1,T_1) = \int_{-\infty}^{E_1} \int_{-\infty}^{T_1} p(e)p(t_r)dt_r de , \qquad (4.66)$$

and changing the order of integration gives

$$P(E_1,T_1) = \int_{-\infty}^{E_1} p(e) \int_{-\infty}^{T_1} p(t_r)dt_r de . \qquad (4.67)$$

Some input signals that cross the upper-level threshold of the constant-fraction discriminator do not produce output pulses because of the SRT circuitry. The joint probability density function can be modified to show this relative loss of efficiency. The remainder of this section describes these modifying effects for the SRT circuitry used in ARC timing with each of the three types of input signals selected in Chapter III.

From Equation (4.2), page 76, input signals to the discriminator shown in Figure 4.2, page 74, must rise from zero to the upper-level threshold in a time less than the zero-crossing time of the bipolar timing pulse plus the fixed delay time t_k. Timing pulses resulting from input signals that do not meet this upper-level constraint are rejected when the SRT circuitry is used. The delay time t_k is chosen according to Equation (4.20), page 83, for decreasing slope input signals; t_k is chosen according to Equation (4.39), page 87, for linear input signals; and t_k is chosen according to Equation (4.54), page 90, for input signals with increasing slopes. The discriminator that was actually used in testing has a constant-fraction shaping delay, t_d, chosen for ARC timing with Ge(Li) detectors. For ARC timing the upper-level constraint in Equation (4.2), page 76, becomes

$$t_{UL} < t_{ARC} + t_k \ , \tag{4.68}$$

where t_{ARC} is the ARC zero-crossing time for the particular type of input signal. Equation (4.68) insures that leading-edge time walk is not introduced at the upper-level coincidence gate, G2.

For the decreasing slope input signal $e_1(t)$, described in Equation (4.3), page 79, the time from zero to the upper-level threshold of the discriminator is

$$t_{UL1} = t_{r1} \left(\frac{E_{th}}{E}\right)^2 , \tag{4.69}$$

from Equation (4.6), page 79. Solving this equation for the risetime of the input pulse yields

$$t_{r1} = t_{UL1} \left(\frac{E}{E_{th}}\right)^2 . \tag{4.70}$$

Combining Equations (4.68) and (4.70) gives the risetime constraint for the decreasing slope input signal to be processed by the discriminator as

$$t_{r1} < t_{b1} \left(\frac{E}{E_{th}}\right)^2 , \tag{4.71}$$

where t_{b1} is defined by

$$t_{b1} = t_{ARC1} + t_k . \tag{4.72}$$

Substituting the ARC zero-crossing time due to the decreasing slope input signal $e_1(t)$ into this equation yields

$$t_{b1} = \frac{t_d}{1-f^2} + t_k . \tag{4.73}$$

Equation (4.71) is the condition the risetime t_{r1}, of a decreasing slope input signal to the third generation discriminator, must meet in order to be accepted and processed by the discriminator when the SRT circuitry is employed. This condition is used to modify the joint probability density function for random input signals to show the efficiency degradation.

The integral with respect to risetime in the joint probability distribution function of Equation (4.67), page 95, can be evaluated, using the constraint in Equation (4.71). Amplitude is then the only variable in the modified joint probability density function. The modified probability distribution function becomes

$$P_{1(\text{mod})}(e) = \int_{-\infty}^{e} p(e) \left[1 - \int_{\left(\frac{e}{E_{th}}\right)^2 t_{b1}}^{\infty} p(t_r)dt_r\right]de \ , \qquad (4.74)$$

under the constraints that the bracketed term is greater than zero and less than unity. The term inside the bracket is the risetime probability distribution that has been modified due to the use of the SRT circuit. The integral within the bracket represents decreasing slope input signals that cross the instrument threshold but produce no output pulses. The equation is general in nature for ARC timing with the discriminator with SRT circuitry, for random decreasing slope input signals. Note that because of the loss in counting efficiency due to the SRT circuitry in the discriminator, the probability of obtaining an output pulse for every input signal above threshold is less than one. Thus, the area under the modified probability density function curve is less than unity.

Evaluating Equation (4.74) for the uniform amplitude and risetime probability density functions of Equation (4.59), page 93, and Equation (4.62), page 94, yields

$$P_{1(mod)}(e) = \int_{o}^{e<E_v} \frac{1}{E_v} \left[1 - \int_{\left(\frac{e}{E_{th}}\right)^2 t_{b1}}^{mT_r} \frac{1}{(m-1)T_r} dt_r \right] de \ . \qquad (4.75)$$

The modified joint probability density function for decreasing slope input signals with independent, uniform amplitude and risetime probability density functions is the integrand of the preceding equation and can be expressed as

$$P_{1(mod)}(e) = \begin{cases} 0 & e < E_{th} \\ \frac{1}{E_v} \left[1 - \frac{m}{(m-1)} \left[1 - \frac{t_{b1}}{mT_r} \left(\frac{e}{E_{th}}\right)^2 \right] \right], & 0 \leq P_{1(mod)}(e) \leq 1 \\ 0 & e > E_v \end{cases} . \qquad (4.76)$$

This modified density equation is valid for ARC timing with the discriminator shown in Figure 4.2, page 74, when the SRT function is used.

Figure 4.4 shows curves for the modified probability density function from Equation (4.76) for various values of the fixed time t_{b1}, as defined in Equation (4.73). These curves are normalized to an amplitude of unity. This figure is an indication of the relative reduction in counting efficiency due to the Slow-Risetime-Reject circuit used in the third generation discriminator. The curve for the uniform density function is for decreasing slope input signals above the

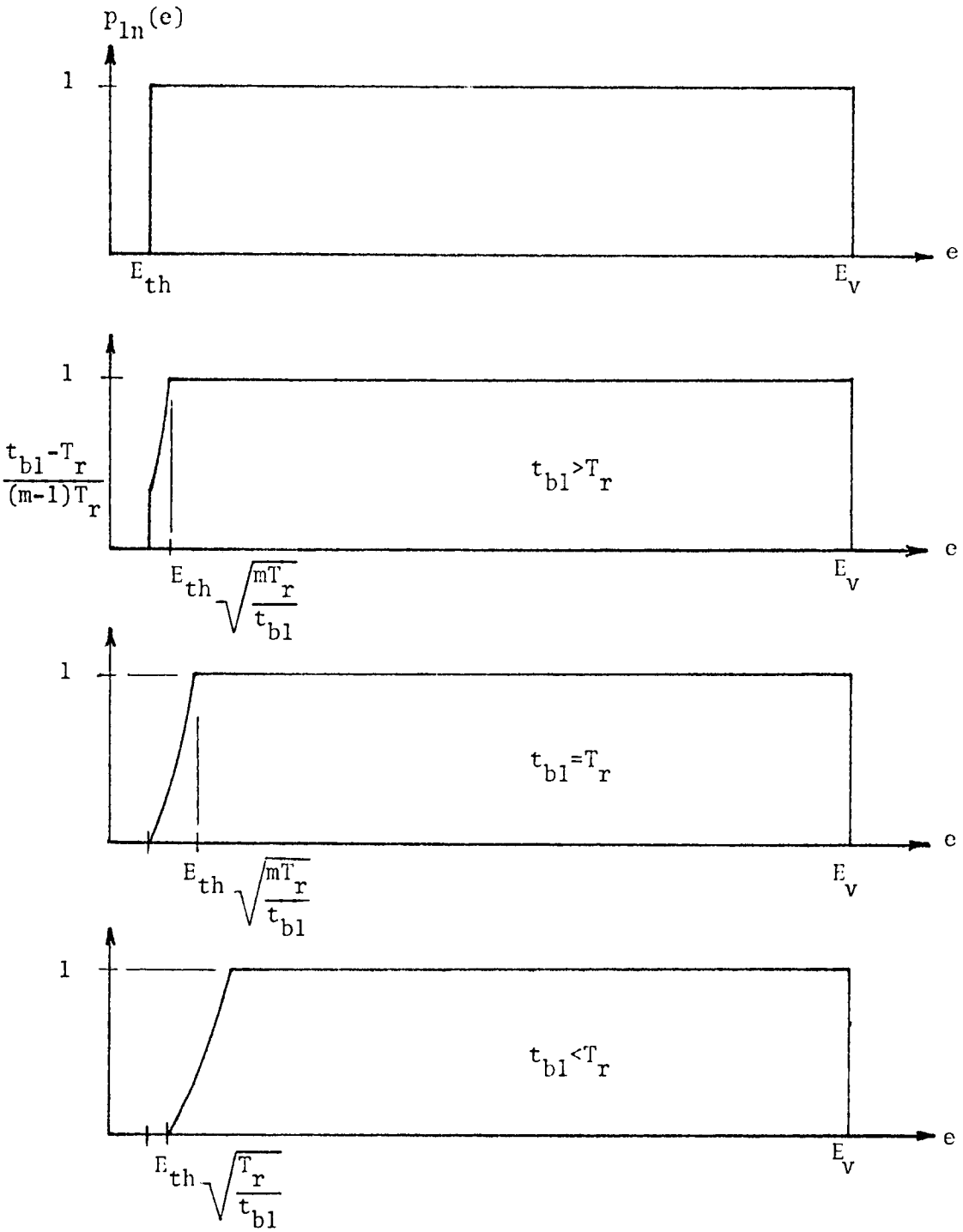


Figure 4.4. Uniform energy probability density function, modified due to rejection of slow risetime, decreasing slope input signals with a uniform risetime probability density.

threshold level that are presented to the input of the discriminator. The curves show that input pulses with amplitudes near the instrument threshold are less likely to produce output pulses from the instrument.

For the linear input signal $e_2(t)$, described by Equation (4.22), page 83, the time from zero to the threshold level of the upper-level discriminator is

$$t_{UL2} = \frac{E_{th} t_{r2}}{E} , \tag{4.77}$$

from Equation (4.25), page 84. Solving this equation for the risetime of the input pulse yields

$$t_{r2} = \frac{E t_{UL2}}{E_{th}} . \tag{4.78}$$

Combining Equation (4.68), page 96, with Equation (4.78) gives the risetime constraint for linear input signals to be processed by the discriminator as

$$t_{r2} < \frac{E t_{b2}}{E_{th}} , \tag{4.79}$$

where t_{b2} is defined by

$$t_{b2} = t_{ARC2} + t_k . \tag{4.80}$$

Substituting the ARC zero-crossing time due to the linear input signal $e_2(t)$ into this equation yields

$$t_{b2} = \frac{t_d}{1-f} + t_k \ . \tag{4.81}$$

Equation (4.79) is the condition the risetime t_{r2}, of a linear input signal to the third generation discriminator, must meet in order to be accepted and processed by the discriminator when the SRT circuitry is employed. This condition is used to modify the joint probability density function for random input signals to show the efficiency degradation.

The integral with respect to risetime in the joint probability distribution function of Equation (4.67), page 95, can be evaluated, using the risetime constraints in Equation (4.79). Amplitude is then the only variable in the modified joint probability density function. The modified probability distribution function becomes

$$P_{2(\text{mod})}(e) = \int_{-\infty}^{e} p(e) \left[1 - \int_{\frac{et_{b2}}{E_{th}}}^{\infty} p(t_r)dt_r\right]de \ , \tag{4.82}$$

under the constraints that the bracketed term is greater than zero and less than unity. The term inside the bracket is the risetime probability distribution that has been modified due to the use of the SRT circuit. The integral within the bracket represents linear input signals that cross the instrument threshold but produce no output pulses. This equation is general in nature for ARC timing with the discriminator with SRT circuitry, for random linear input signals. Note that because of the loss in counting efficiency due to the SRT circuitry in the discriminator, the probability of obtaining an output pulse for every input signal above

threshold is less than one. Thus, the area under the modified probability density function curve is less than unity.

Evaluating Equation (4.82) for the uniform amplitude and risetime probability density functions of Equation (4.59), page 93, and Equation (4.62), page 94, yields

$$P_{2(\text{mod})}(e) = \int_{o}^{e<E_v} \frac{1}{E_v} \left[1 - \int_{\frac{et_{b2}}{E_{th}}}^{mT_r} \frac{1}{(m-1)T_r} dt_r \right] de \ . \qquad (4.83)$$

The modified joint probability density function for linear input signals with independent, uniform amplitude and risetime probability density functions is the integrand of the preceding equation and can be expressed as

$$P_{2(\text{mod})}(e) = \begin{cases} 0, & e < E_{th} \\ \frac{1}{E_v} \left[1 - \frac{m}{(m-1)} \left[1 - \frac{et_{b2}}{mT_r E_{th}} \right] \right], & 0 \leq P_{2(\text{mod})}(e) \leq 1 \ . \\ 0, & e > E_v \end{cases} \qquad (4.84)$$

This modified density equation is valid for ARC timing with the discriminator shown in Figure 4.2, page 74.

Figure 4.5 shows curves for the modified probability density function from Equation (4.84) for various values of the fixed time t_{b2}, as defined in Equation (4.81). These curves are normalized to an amplitude of unity. This figure is an indication of the relative reduction in counting

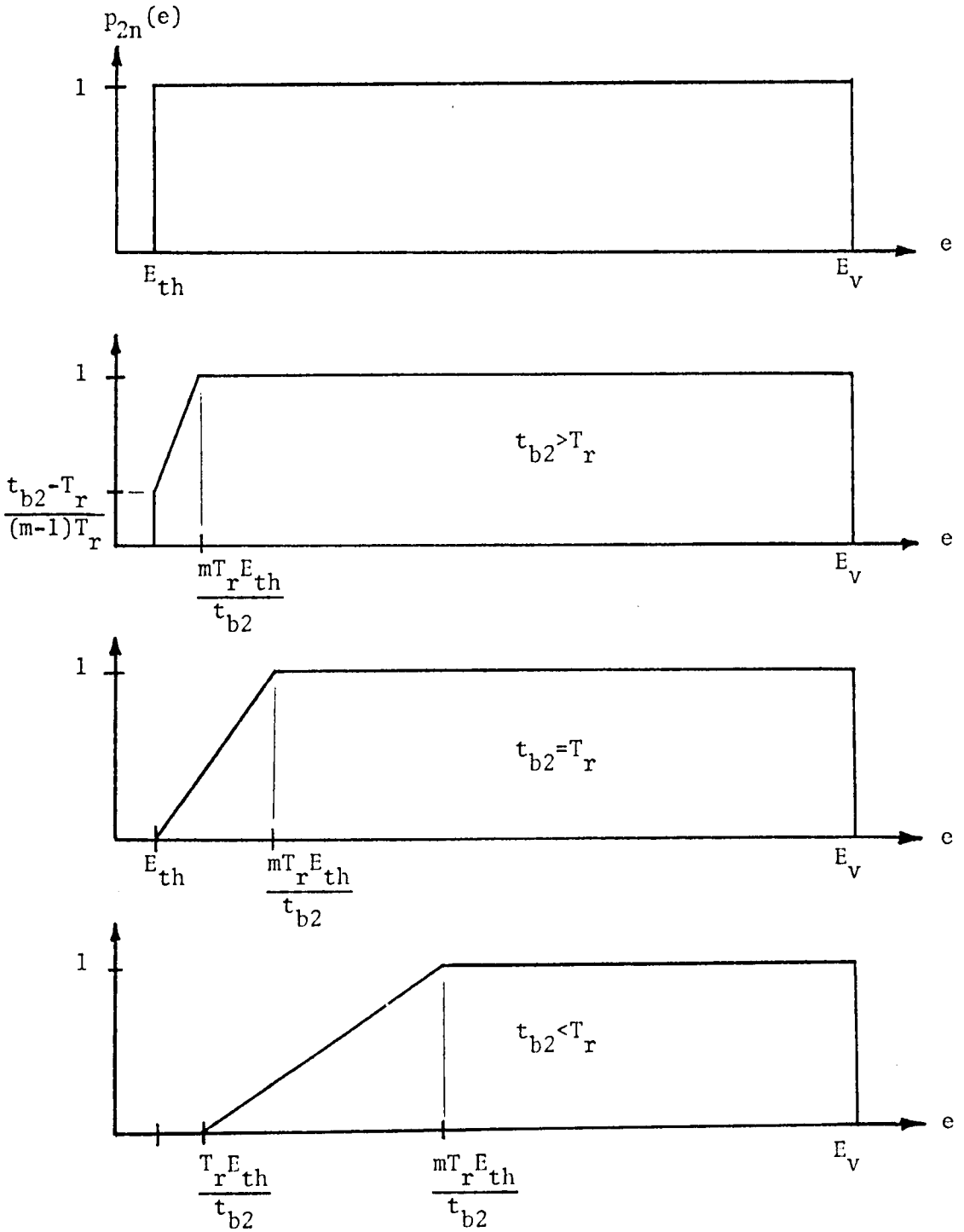


Figure 4.5. Uniform energy probability density function, modified due to rejection of slow risetime linear input signals with a uniform risetime probability density.

efficiency due to the Slow-Risetime-Reject circuit used in the third generation discriminator. The curve for the uniform density function is for linear input signals above the threshold level that are presented to the input of the discriminator. The curves show that input pulses with amplitudes near the instrument threshold are less likely to produce output pulses from the unit.

Now, considering the increasing slope input signal $e_3(t)$, described by Equation (4.41), page 87, the time from zero to the threshold of the ULLE discriminator is

$$t_{UL3} = t_{r3} \sqrt{\frac{E_{th}}{E}} , \tag{4.85}$$

from Equation (4.44), page 88. Solving this equation for the risetime of the input pulse yields

$$t_{r3} = t_{UL3} \sqrt{\frac{E}{E_{th}}} . \tag{4.86}$$

From Equation (4.68), page 96, and Equation (4.43), page 88, the time from zero to the threshold of the upper-level discriminator for $e_3(t)$ must meet the constraint

$$t_{UL3} < t_{b3} , \tag{4.87}$$

where

$$t_{b3} = \frac{t_d}{1-\sqrt{f}} + t_k . \tag{4.88}$$

This inequality must be met by the increasing slope input signal $e_3(t)$, in order to be accepted and processed by the discriminator in the SRT mode. ARC timing is then insured from the instrument for input signals described by $e_3(t)$. Equations (4.86) and (4.87) are combined to modify the joint probability density function for random input signals with increasing slopes.

The integral with respect to risetime in the joint probability distribution function of Equation (4.67), page 95, can be evaluated, using the risetime constraint from Equations (4.86) and (4.87). Amplitude is then the only variable in the modified joint probability density function. The modified distribution function becomes

$$P_{3(\text{mod})}(e) = \int_{-\infty}^{e} p(e) \left[1 - \int_{t_{b3}\sqrt{\frac{e}{E_{th}}}}^{\infty} p(t_r)dt_r \right] de \ , \qquad (4.89)$$

under the constraints that the bracketed term is greater than zero and less than unity. The term inside the bracket is the risetime probability distribution that has been modified due to the SRT circuit. The integral within the bracket represents input signals that cross the upper-level threshold, but do not produce output pulses from the unit. This equation is general in application for ARC timing with random, increasing slope input signals that can be described by $e_3(t)$. Note that because of the loss in counting efficiency due to the SRT circuitry in the discriminator, the probability of obtaining an output pulse for every input signal above threshold is less than one. Thus, the area under the modified probability density function curve is less than unity.

Evaluating Equation (4.89) for the uniform amplitude and risetime probability density functions of Equation (4.59), page 93, and Equation (4.62), page 94, yields

$$P_{3(mod)}(e) = \int_{o}^{e<E_v} \frac{1}{E_v} \left[1 - \int_{t_{b3}\sqrt{\frac{e}{E_{th}}}}^{mT_r} \frac{1}{(m-1)T_r} dt_r \right] de \ . \qquad (4.90)$$

The modified joint probability density function is the integrand of the preceding equation and can be expressed as

$$P_{3(mod)}(e) = \begin{cases} 0, & e < E_{th} \\ \frac{1}{E_v} \left[1 - \frac{m}{(m-1)} \left(1 - \frac{t_{b3}}{mT_r} \sqrt{\frac{e}{E_{th}}} \right) \right], & 0 \leq P_{3(mod)}(e) \leq 1 \ . \\ 0, & e > E_v \end{cases} \qquad (4.91)$$

This modified probability density equation is valid for signals with increasing slopes at the input of the third generation discriminator when the SRT circuit is used. The amplitude and risetime density functions for these pulses are uniform and independent.

Figure 4.6 shows the curves for the modified probability density function from Equation (4.91) for various values of the fixed time t_{b3}. These curves are normalized to unity amplitude. This figure is an indication of the relative reduction in counting efficiency due to the SRT circuitry used in the discriminator of Figure 4.2, page 74. The curve for the uniform density function is for increasing slope input signals, with amplitudes above the instrument threshold, that are

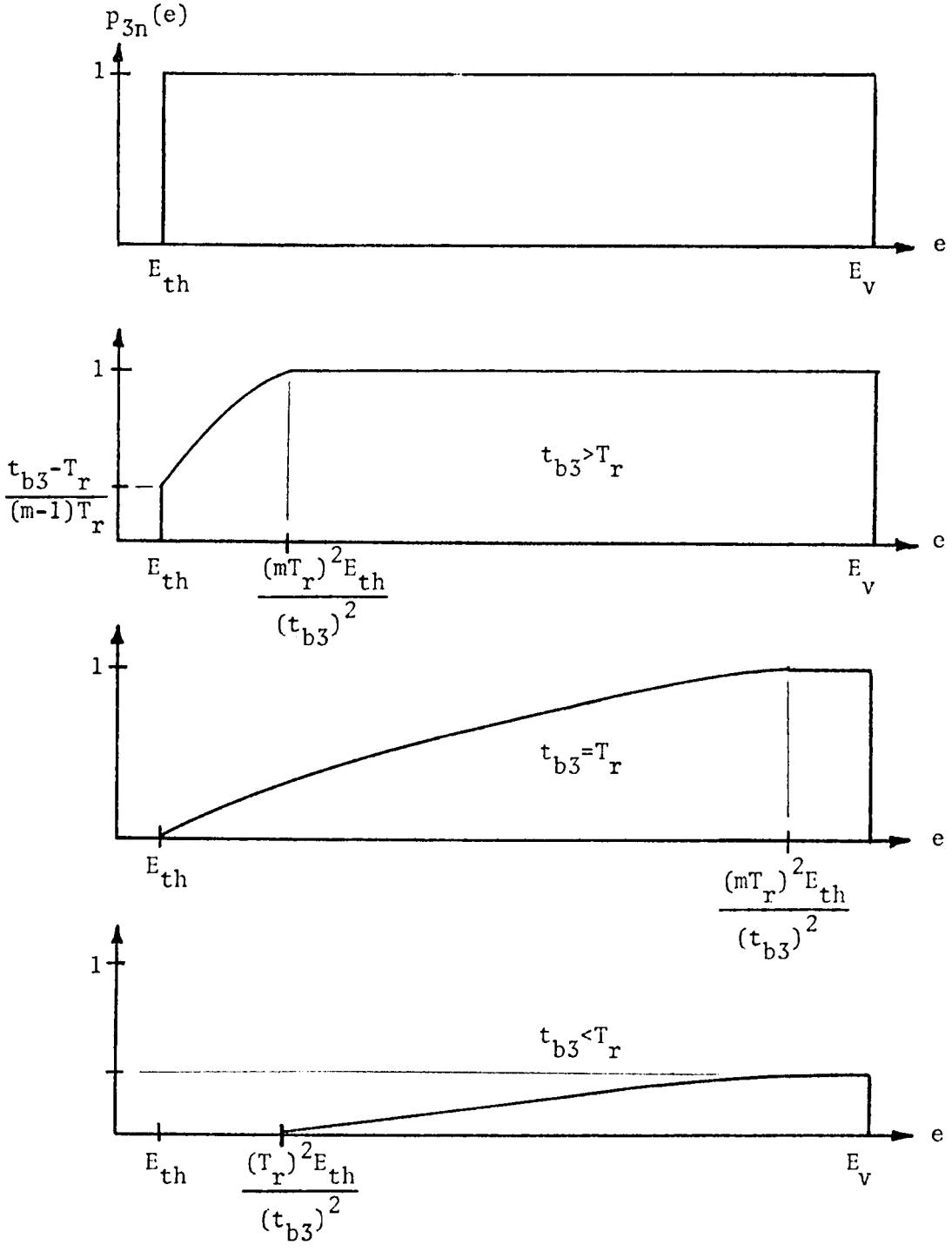


Figure 4.6. Uniform energy probability density function, modified due to rejection of slow risetime, increasing slope input signals with a uniform risetime probability density.

presented to the input of the discriminator. Input pulses with amplitudes near the discriminator threshold are less likely to produce signals when the SRT circuitry is used.

Qualitative comparisons of the effects of the SRT circuitry on energy information can be made for the three representative types of input signals. Comparing the modified probability density functions shown in Figure 4.4, page 100, with those shown in Figure 4.5, page 104, and Figure 4.6 indicates that the SRT circuitry places the greatest constraints on the increasing slope input signals described by $e_3(t)$. Counting efficiency is reduced the least for the decreasing slope input signals described by $e_1(t)$.

The reduction in system counting efficiency at a particular value of input pulse height can be found as a function of threshold level for the decreasing slope, constant slope and increasing slope input signals under consideration. This reduction is a convenient parameter for comparisons of systems, since it can be extracted from measured data. The relative loss in counting efficiency at amplitude E_1 due to rejection of leading-edge timing signals derived from slow, decreasing slope input signals can be found in Equation (4.76), page 99, as

$$P_{1(\text{loss})}(E_{th}) = \begin{cases} 0, & E_{th} < E_1\sqrt{\dfrac{t_{b1}}{mT_r}} \\ \dfrac{m}{(m-1)}\left[1 - \dfrac{t_{b1}}{mT_r}\left(\dfrac{E_1}{E_{th}}\right)^2\right], & 0 \leq P_{1(\text{loss})}(E_{th}) \leq 0 \\ 1, & E_{th} > E_1 \end{cases} . \quad (4.92)$$

This equation represents the risetime probability distribution for decreasing slope input signals that produce no output pulses. The relative loss in counting efficiency at amplitude E_2 due to the rejection of leading-edge timing signals derived from slow linear input signals can be found in Equation (4.84), page 103, as

$$P_{2(loss)}(E_{th}) = \begin{cases} 0, & E_{th} < \dfrac{E_2 t_{b2}}{mT_r} \\ \dfrac{m}{(m-1)}\left[1 - \dfrac{t_{b2}}{mT_r}\left(\dfrac{E_2}{E_{th}}\right)\right], & 0 \leq P_{2(loss)}(E_{th}) \leq 1 \\ 1, & E_{th} > E_2 \end{cases} . \qquad (4.93)$$

This equation represents the risetime probability distribution for linear input signals that produce no output pulses. In Equation (4.91) the relative loss in system counting efficiency at amplitude E_3 due to rejection of leading-edge timing pulses derived from slow, increasing slope input signals is found to be

$$P_{3(loss)}(E_{th}) = \begin{cases} 0, & E_{th} < E_3\left(\dfrac{t_{b3}}{mT_r}\right)^2 \\ \dfrac{m}{(m-1)}\left[1 - \dfrac{t_{b3}}{mT_r}\sqrt{\dfrac{E_3}{E_{th}}}\right], & 0 \leq P_{3(loss)}(E_{th}) \leq 1 \\ 1, & E_{th} > E_3 \end{cases} . \qquad (4.94)$$

Figure 4.7 shows the relative reduction in counting efficiency at input signal amplitude E_2 due to the Slow-Risetime-Reject circuit. This representation is valid for linear input signals with uniform energy and

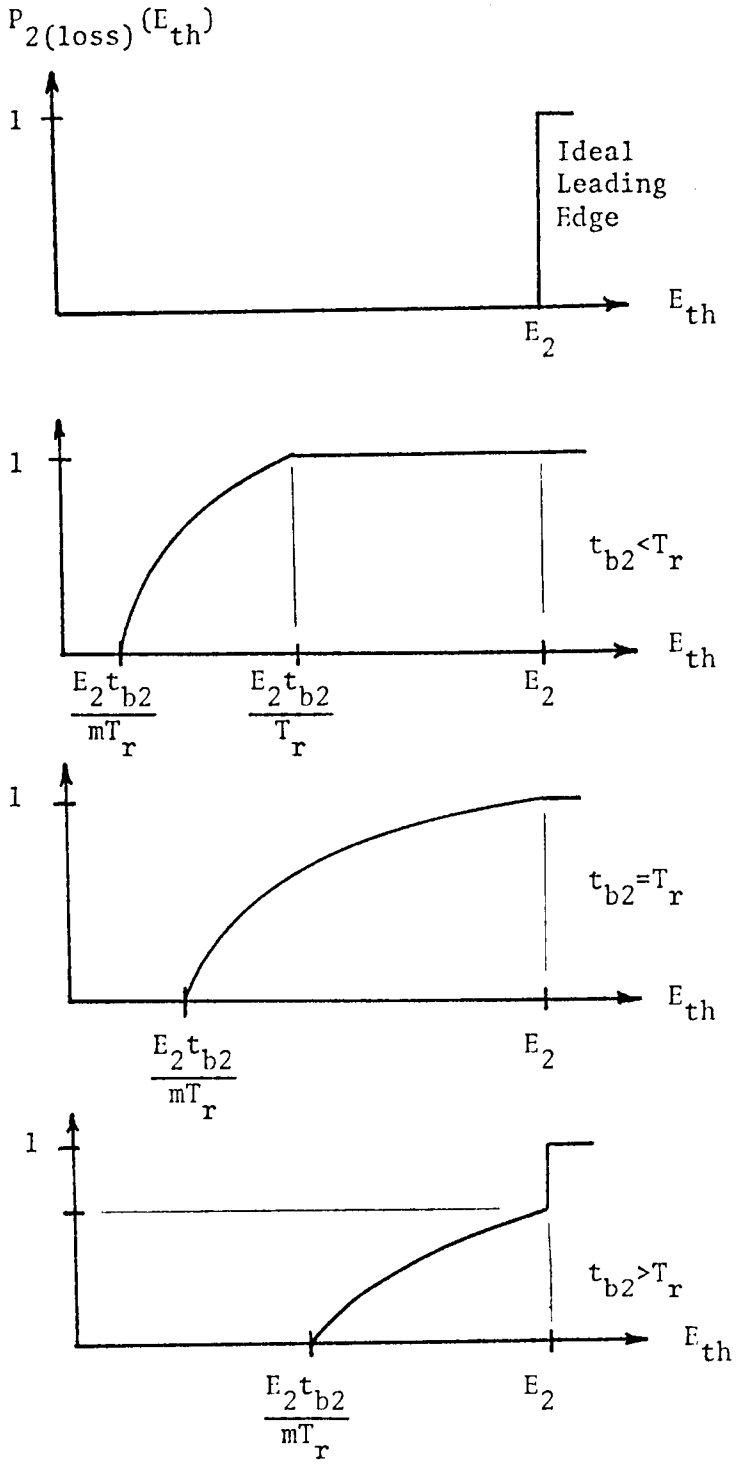


Figure 4.7. Normalized loss in system counting efficiency at energy E_2 due to rejection of valid linear input signals because of Slow-Risetime-Reject circuitry; risetime probability density is uniform.

risetime probability density functions. The loss in efficiency is shown for various values of fixed time t_{b2}, defined in Equation (4.80), page 101. Decreasing t_{b2} causes a significantly greater loss in counting efficiency when the SRT circuit is employed.

Efficiency Loss for Nonuniform Risetime Probability Density

Chapter VI shows an experimentally determined risetime probability density function that is more realistic for most Ge(Li) timing applications than the uniform density function assumed in the previous section. This risetime probability density function can be approximated by a single time constant, decaying exponential and is shown in Chapter VI to be virtually independent of the energy of the event. The probability density function is accumulated for 10 percent to 90 percent risetimes and can be approximated by

$$p(t_R) = \begin{cases} \frac{1}{\tau_R} \varepsilon^{-(t_R - T_R)/\tau_R}, & t_R > T_R \\ 0, & \text{elsewhere} \end{cases} . \qquad (4.95)$$

In this expression, the variable t_R is the 10 percent to 90 percent risetime of the input signals, and T_R is the minimum observed 10 percent to 90 percent risetime. The term τ_R is the exponential decay time constant of the density function and is determined from the experimental data.

No means was implemented to experimentally determine the relative contributions of the decreasing slope, constant slope and increasing

slope input signals to the exponential risetime probability density function. Therefore, as a first order approximation the input signals to the discriminator are all assumed to be linear. The validity of this assumption is discussed in Chapter VI.

For random linear input signals the joint probability distribution function of amplitudes and 10 percent to 90 percent risetimes is

$$P_2(e,t_R) = \int_{-\infty}^{e} p(e) \int_{-\infty}^{t_R} p(t_R)dt_R de \ . \tag{4.96}$$

In order for the density functions to be separable, as indicated in this equation, the amplitude and risetime probability density functions must be independent of each other. This expression is similar to Equation (4.67), page 95, with the exception of the risetime variable t_R. Using the technique outlined in the previous section, the integral with respect to risetime in Equation (4.96) can be modified due to use of the Slow-Risetime-Reject circuitry and then evaluated. By applying Equation (4.79), page 101, the equivalent 10 percent to 90 percent risetime constraint for linear input signals to be processed by the discriminator is seen to be

$$t_{R2} < \frac{0.8\ Et_{b2}}{E_{th}} \ . \tag{4.97}$$

Using this expression to evaluate the second integral in Equation (4.96) yields the modified joint probability distribution function

$$P_{2\varepsilon(\text{mod})}(e) = \int_{-\infty}^{e} p(e) \left[1 - \int_{\frac{0.8\ et_{b2}}{E_{th}}}^{\infty} p(t_R)dt_R\right]de \ , \qquad (4.98)$$

under the constraints that the bracketed term is greater than zero and less than unity. The term inside the bracket is the 10 percent to 90 percent risetime probability distribution that has been modified, due to the use of the SRT circuit. The integral within the bracket represents linear input signals that cross the instrument threshold but produce no output pulses. Note that because of the loss in counting efficiency due to the SRT circuitry in the discriminator, the probability of obtaining an output pulse for every signal above threshold is less than one. Thus, the area under the modified probability density function curve is less than unity.

The modified joint probability density function for linear input signals with independent amplitude and risetime probability density functions is the integrand of Equation (4.98). For the uniform amplitude probability density function of Equation (4.59), page 93, and for the exponential risetime probability density function of Equation (4.95), page 112, the modified joint probability density function becomes

$$p_{2\varepsilon(\text{mod})}(e) = \begin{cases} \dfrac{1}{E_v}\left[1 - \varepsilon^{-\left(\frac{0.8\ et_{b2}}{E_{th}} - T_R\right)/\tau_R}\right], & 0 \leq p_{2\varepsilon(\text{mod})}(e) \leq 1 \ . \\ 0, & e < E_{th} \end{cases} \qquad (4.99)$$

Figure 4.8 shows the modified probability density function from Equation (4.99), for the relative values

$$t_{b2} = 0.91\ T_R \tag{4.100}$$

and

$$\tau_R = 0.76\ T_R\ . \tag{4.101}$$

This curve is normalized to unity amplitude. A method for determining the values of these constants is discussed in Chapter VI. Figure 4.8 is an indication of the relative reduction in counting efficiency caused by the use of the SRT circuitry in the third generation constant-fraction discriminator. The spectrum indicated by the dotted line represents linear signals with amplitudes above the threshold of the instrument that are applied to the input of the discriminator. The solid curve represents the portion of those signals that produce output pulses.

The discussion in the previous section indicates that a parameter of particular interest is the efficiency reduction at a particular value of input pulse height. This quantity can be found as a function of the discriminator threshold level, for the exponential risetime density function under consideration. The relative loss in counting efficiency, due to rejection of slow linear input signals, is found in Equation (4.99) as

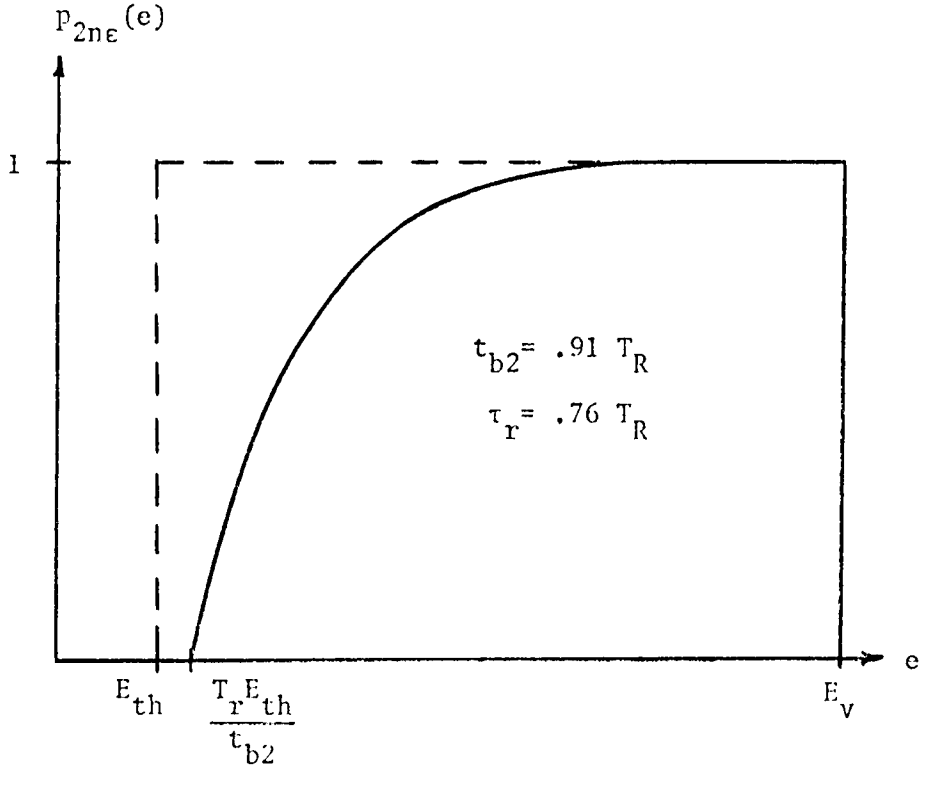


Figure 4.8. Uniform energy probability density function, modified due to rejection of slow risetime linear input signals with an exponential risetime probability density.

$$P_{2\varepsilon(loss)}(E_{th}) = \begin{cases} \varepsilon^{-\left(\frac{0.8\,E_2 t_{b2}}{E_{th}} - T_R\right)/\tau_R}, & 0 \leq P_{2\varepsilon(loss)}(E_{th}) \leq 1 \\ 1, & E_{th} > E_2 \end{cases} \quad . \quad (4.102)$$

This equation represents the probability distribution of 10 percent to 90 percent risetimes for linear input signals resulting in timing pulses that are rejected. Figure 4.9 shows the relative loss in the timing system counting efficiency at input pulse amplitude E_2, due to use of the Slow-Risetime-Reject circuit.

Summary

Chapter IV presents a simplified block diagram in Figure 4.2, page 74, and a general circuit concept description of the third generation constant-fraction discriminator used to obtain experimental data. Criteria for the fixed delay time t_k are established to insure that the Slow-Risetime-Reject circuitry in the unit can be used to eliminate those logic signals resulting from leading-edge timing. These criteria are derived for the decreasing slope, constant slope and increasing slope input signals $e_1(t)$, $e_2(t)$ and $e_3(t)$, respectively, shown in Figure 3.4, page 59, and defined in Chapter III.

A reduction in system counting efficiency is a price paid for improved timing information obtained by using the Slow-Risetime-Reject circuit. The reduction in the counting efficiency of the third generation discriminator is determined analytically for the three representative input signals $e_1(t)$, $e_2(t)$ and $e_3(t)$, assuming that they

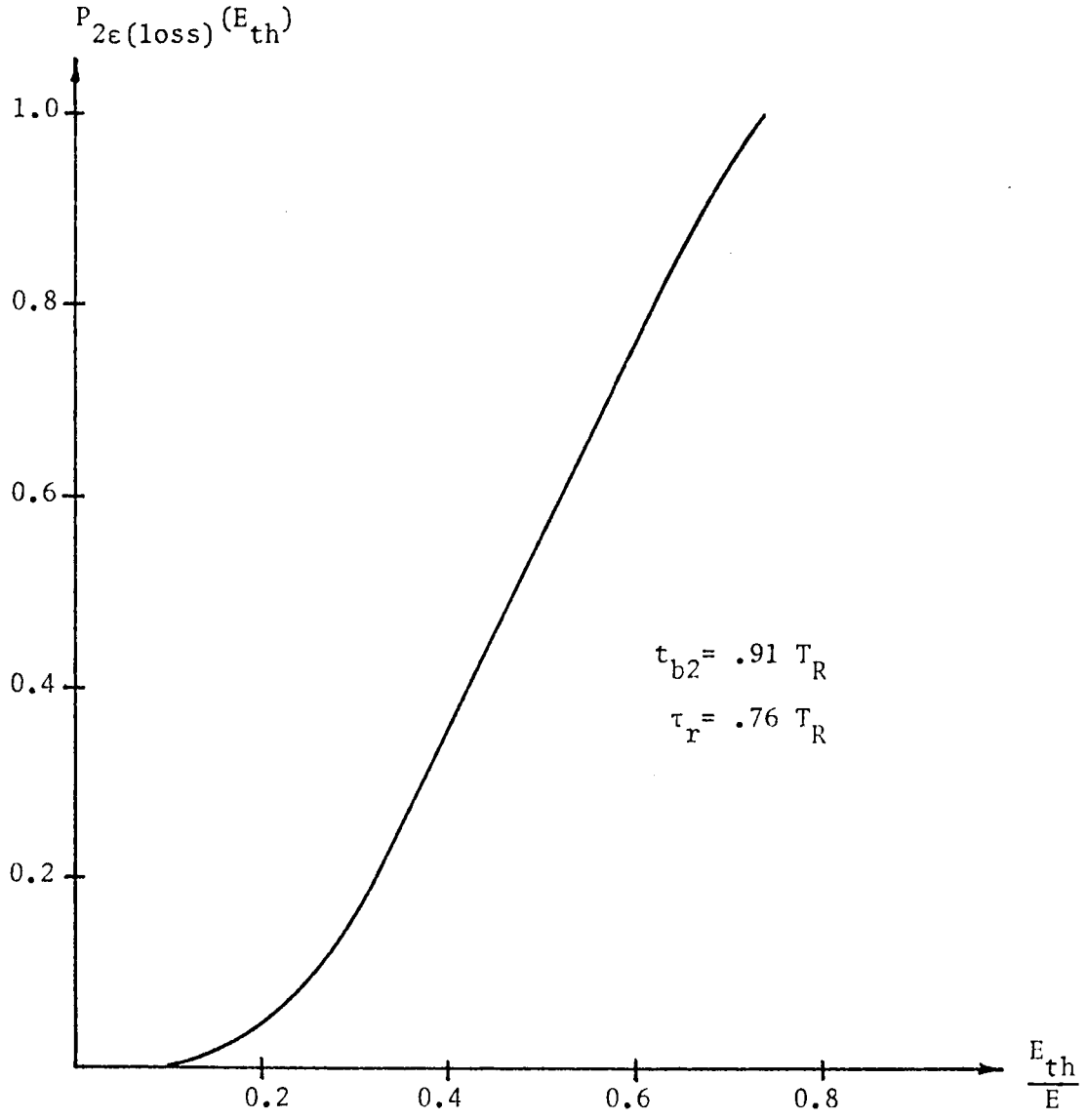


Figure 4.9. Normalized loss in system counting efficiency at energy E_2 as a function of threshold due to Slow-Risetime-Reject circuit; linear input signals with an exponential risetime probability density function.

have uniform risetime and amplitude distributions. Efficiency degradation is also derived for a fixed amplitude of linear input signals with an exponential risetime probability distribution. These latter results are examined experimentally in Chapter VI.

CHAPTER V

A CONSTANT-FRACTION DISCRIMINATOR WITH DUAL THRESHOLD AND SLOW-RISETIME-REJECT CIRCUITRY

A commercially available constant-fraction discriminator, based on the third generation circuit discussed in the previous chapter, is discussed in this chapter. This timing module was used to obtain the experimental data for the dissertation. A diagram of the logic circuitry for the discriminator is shown, a circuit description is given, and some of the important specifications are discussed.

Circuit Description

The circuit diagram of essential logic components for the third generation constant-fraction discriminator used to obtain experimental data is shown in Figure 5.1. This discriminator can be used for TCF or ARC timing with a variety of detectors. The circuit contains three fixed shaping delays, selected for ARC timing with three specific types of detectors, and an external mode to allow the experimenter to choose both fraction and delay. The instrument can operate in the constant-fraction discriminator mode, the Slow-Risetime-Reject mode or the leading-edge discriminator mode.

A negative-going input signal is furnished simultaneously to three discriminator circuits through emitter followers, for buffering and level-shifting. The input signal is attenuated by a factor f, defined by

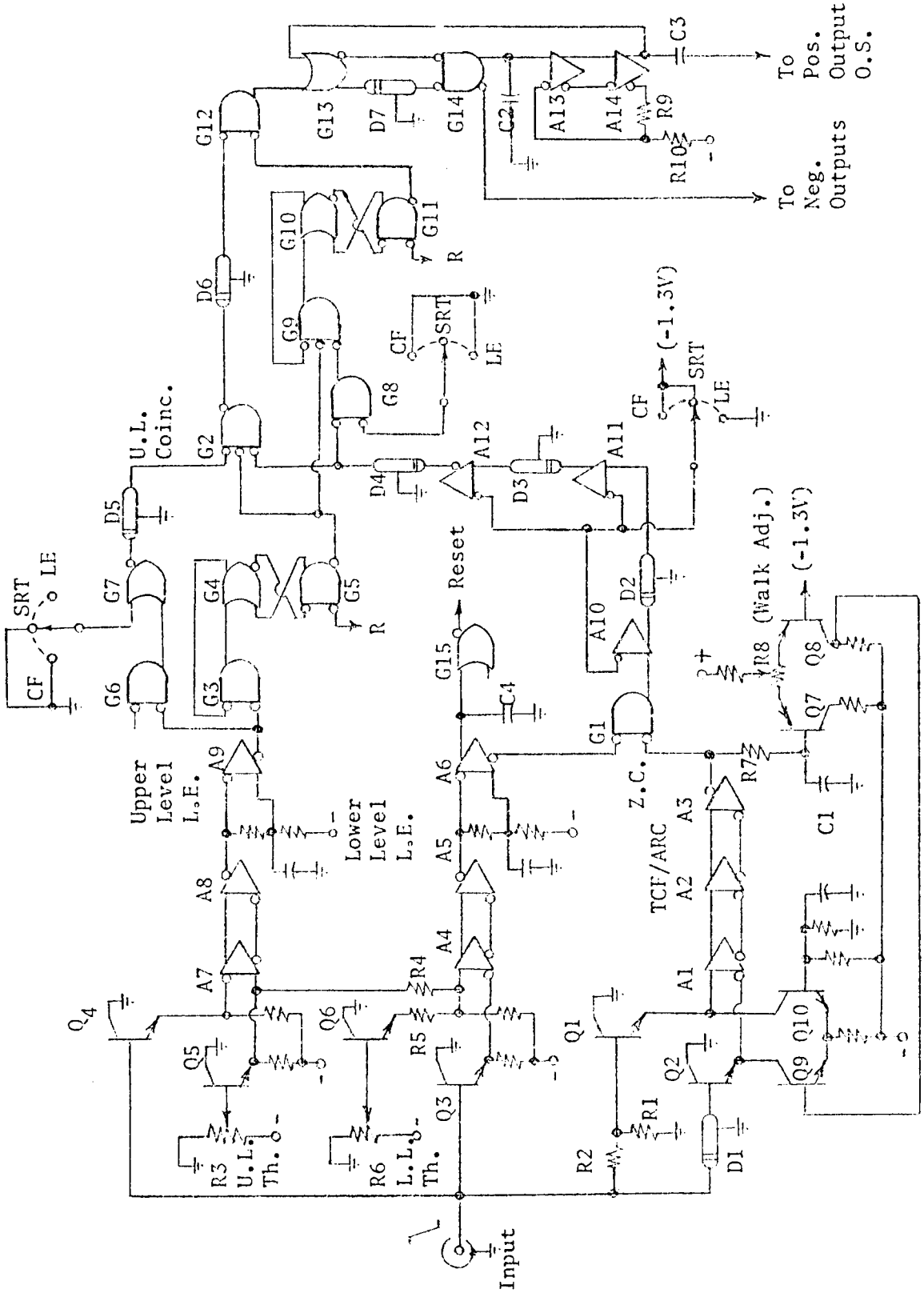


Figure 5.1. Circuit diagram of essential logic components in the third generation constant-fraction discriminator with dual threshold and Slow-Risetime-Reject circuitry.

$$f = \frac{R1}{R1 + R2}, \tag{5.1}$$

and it is delayed with a detector mode switch by using the following selectable 50 ohm delay lines:

$$D1 = \begin{cases} 14 \text{ nsec.}, & \text{Ge(Li) Mode} \\ 1.3 \text{ nsec.}, & \text{Scintillator Mode} \\ 1.9 \text{ nsec.}, & \text{NaI Mode} \\ 3 \text{ nsec. + Ext. del.}, & \text{External Mode} \end{cases}. \tag{5.2}$$

These attenuated and delayed signals are fed through transistors Q1 and Q2, respectively, to the inverting and noninverting inputs of a MECL 10116 differential line receiver. Cascaded amplifiers A1, A2 and A3 invert the attenuated input signal and sum the attenuated and delayed signals to form the bipolar timing pulse at the output of A3. The bipolar pulse is integrated by R7 and C1 and compared to -1.3V. Transistors Q7 through Q10 form a dc, differential feedback amplifier which adjusts the dc levels at the inputs of amplifier A1 to maintain the cascaded line receivers in the linear portion of the MECL range. The nominal dc baseline level at the output of A3 is -1.3V and can be adjusted by the variable resistor R8, to compensate for time walk of the ARC timing signal as it crosses the baseline.

Two leading-edge discriminator circuits are also fed from the input signal. Transistor Q3 provides the input signal to the lower-level arming discriminator, composed of cascaded amplifiers A4, A5 and A6. These amplifiers are in a single MECL 10116 line receiver package to match the propagation delay of the constant-fraction circuit. This

matching prevents the zero-crossing detector from pretriggering on noise on the constant-fraction baseline. Transistor Q4 provides the level-shifted input signal to the upper-level discriminator, composed of cascaded amplifiers A7, A8 and A9 in a single MECL 10116 package.

The upper-level leading-edge discriminator threshold is set by variable resistor R3 through transistor Q5. This threshold level determines the minimum input signal amplitude required to produce an output pulse from the instrument. The minimum input signal requirement can be varied from -50mV to -5V. Resistors R4 and R5 have the same resistance value and set the threshold for the lower-level arming discriminator at nominally half the upper-level threshold. Lower-level trim adjustment is accomplished by variable resistor R6 through transistor Q6.

A partial timing diagram is shown in Figure 5.2 as an aid in illustrating the logic functions in the discriminator shown in Figure 5.1. The timing diagram represents the discriminator operated in the ARC timing mode when the SRT circuitry is employed. In order to simplify the timing diagram, the propagation delays and the transition response times of the individual logic components are neglected.

The lower-level discriminator output signal from A6 enables gate G1, which detects the baseline crossing (zero-crossing) of the bipolar timing signal from A3. A timing logic signal is produced from gate G1 and is delayed approximately 30 nsec. by delay lines D2, D3 and D4 and line receivers A10, A11 and A12 to the input of the upper-level coincidence gate, G2.

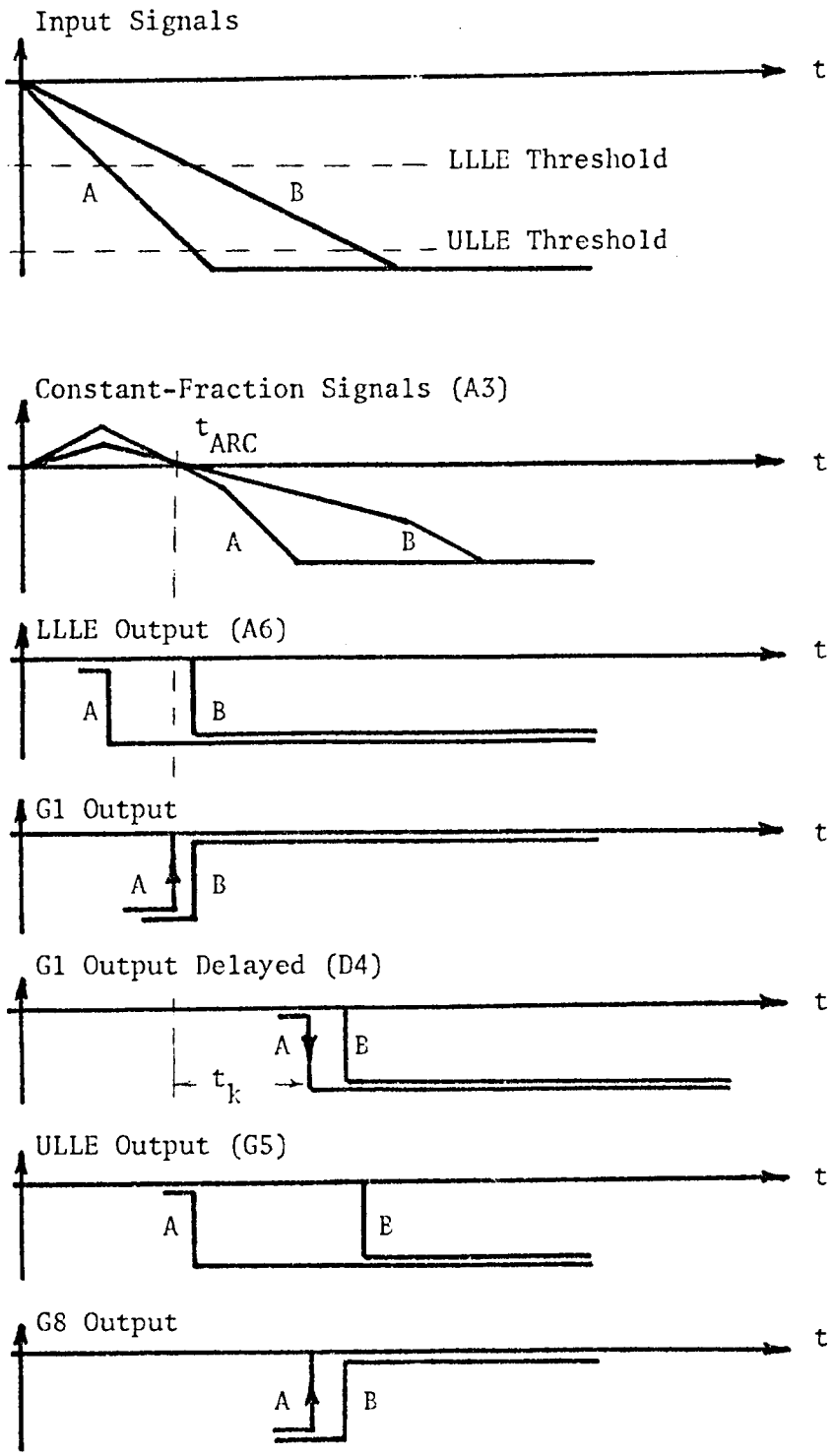


Figure 5.2. Timing diagram for the discriminator operating in the ARC timing mode with the SRT circuitry employed.

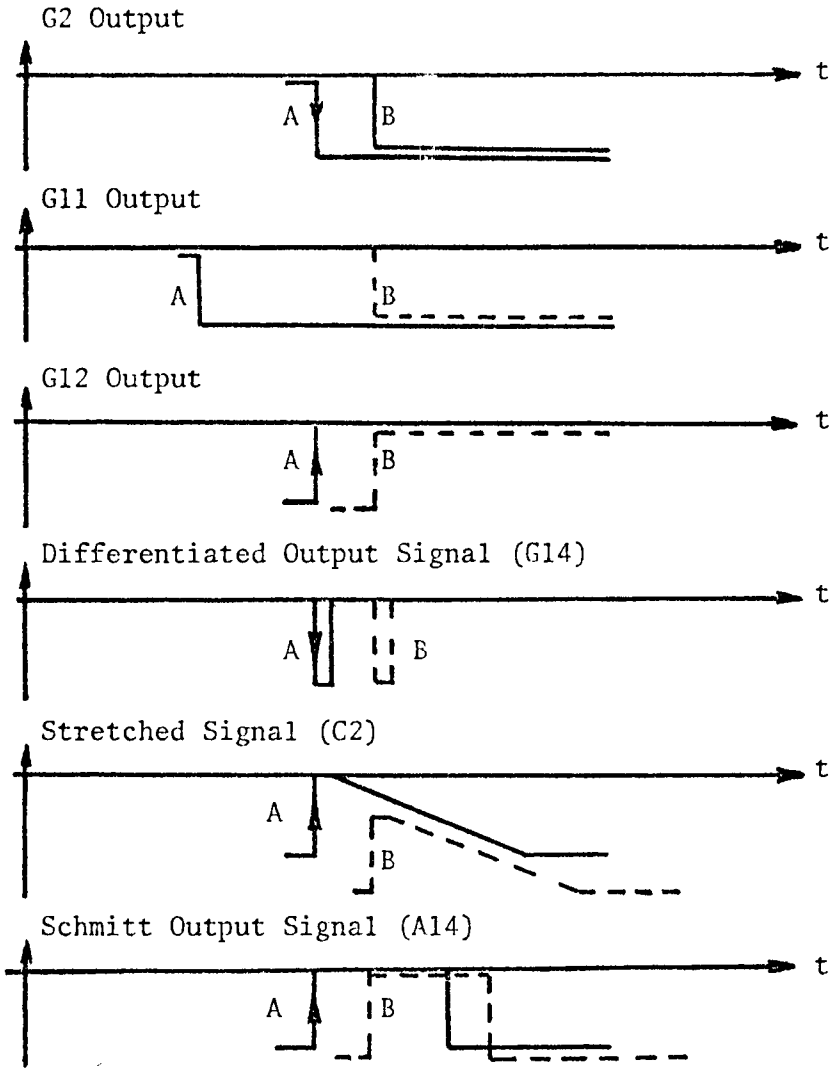


Figure 5.2 (continued)

Gate G2 is enabled for a timing pulse by the output signal from the flip-flop (FF1) comprised of G3, G4 and G5. The positive feedback mechanism of the flip-flop makes a true logic decision for the upper-level leading-edge discriminator. A two-pole, three-position discriminator mode switch allows selection of either leading-edge timing or TCF/ARC timing to be provided at G2. Leading-edge timing is provided through G6, G7 and D5; TCF/ARC timing is provided by the delayed timing logic pulse from G1.

The timing pulse from the upper-level coincidence gate G2 is delayed by D6 during the decision time of the flip-flop (FF2), composed of G9, G10 and G11. When the discriminator mode switch is in the CF or LE position, flip-flop FF2 merely follows the enabling signal for G2, from FF1, and enables gate G12 for every timing signal from G2. When the discriminator mode switch is in the Slow-Risetime-Reject (SRT) position, flip-flop FF2 is set only if the delayed TCF/ARC timing logic pulse from G1 occurs after the upper-level enabling signal from FF1. Thus, in the SRT mode gate G12 is enabled only for those signals that do not introduce leading-edge timing at G2. Both flip-flops FF1 and FF2 are reset through G15 approximately 50 nsec. after the trailing edge of the input signal crosses back through the lower-level threshold.

The timing pulse from G12 is differentiated by gates G13 and G14 and delay line D7 to form a pulse approximately 10 nsec. wide. This pulse drives two current switching pairs to provide the negative output logic pulses. The complement of the differentiated signal is stretched by C2 and shaped by a Schmitt trigger, composed of A13, A14, R9 and R10.

Gate G13 is then blocked to additional timing signals by the output signal from the Schmitt trigger. The blocking time is equal to the period that the stretched signal from G14 is above the Schmitt threshold. Thus, a blocking one-shot multivibrator is formed by the differentiator, stretcher and Schmitt circuitry. The blocking period of this one-shot is chosen to be nominally

$$\text{Blocking Time} = \begin{cases} 50 \text{ nsec., Ge(Li) Mode} \\ 50 \text{ nsec., Scint. Mode} \\ 1 \text{ μsec., NaI Mode} \\ 50 \text{ nsec., Ext. Mode} \end{cases} \tag{5.3}$$

for the various positions of the detector mode switch. The blocking action prevents multiple output pulses from occurring for a single input signal. Capacitor C3 couples the output signal from the Schmitt circuit to a 500 nsec. one-shot, which forms the positive output signal.

All logic components are of the emitter-coupled logic MECL 10,000 series. Risetimes and propagation delays are approximately 2.5 nsec. for each logic element. Printed circuit board layout is extremely critical in preserving good timing information.

Specifications

Ideally there is no time walk in a constant-fraction discriminator operating in the TCF mode for input signals of the same risetime but different amplitudes. However, significant time walk occurs in the discriminator of Figure 5.1, page 121, operating in a TCF mode under these input signal conditions. This time walk is due to the nonlinear response of the MECL line receivers used to form the bipolar timing

signal. The shaping delay for each detector mode switch position is therefore chosen to effectively provide ARC timing to minimize time walk due to the response of the line receivers. These constant-fraction shaping delays are indicated in Equation (5.2), page 122.

A pulse generator is used to determine if the time walk of the ARC timing is within specifications for each unit produced. The test setup is shown in Figure 5.3. Typical pulser walk curves for the scintillator (Scint.) and sodium-iodide (NaI) detector modes are shown in Figure 5.4. Maximum limits for time walk are specified as follows for a 100:1 dynamic range of input signal amplitudes (-50mV to -5V):

$$\text{Walk} \leq \begin{cases} \pm 2 \text{ nsec., Ge(Li) Mode} & (t_r = 40 \text{ nsec.}) \\ \pm 200 \text{ psec., Scint. Mode} & (t_r = 1 \text{ nsec.}) \\ \pm 500 \text{ psec., NaI Mode} & (t_r = 5 \text{ nsec.}) \end{cases} . \qquad (5.4)$$

Some timing experiments require many hours of data accumulation. The temperature stability of the constant-fraction discriminator directly affects the timing resolution of a system for these long-term experiments. The propagation delay stability of the commercial discriminator of Figure 5.1, page 121, is therefore required to be

$$\Delta t_{pd} < 15 \text{ psec./°C, } (10°C \text{ to } 40°C) . \qquad (5.5)$$

The propagation delay temperature stability for four prototype units is shown in Figure 5.5. Note that Δt_{pd} is typically less than 10 psec. per °C in the specified temperature range.

Temperature compensation of the circuit of Figure 5.1 is accomplished by matching the discrete devices that are in the critical timing signal

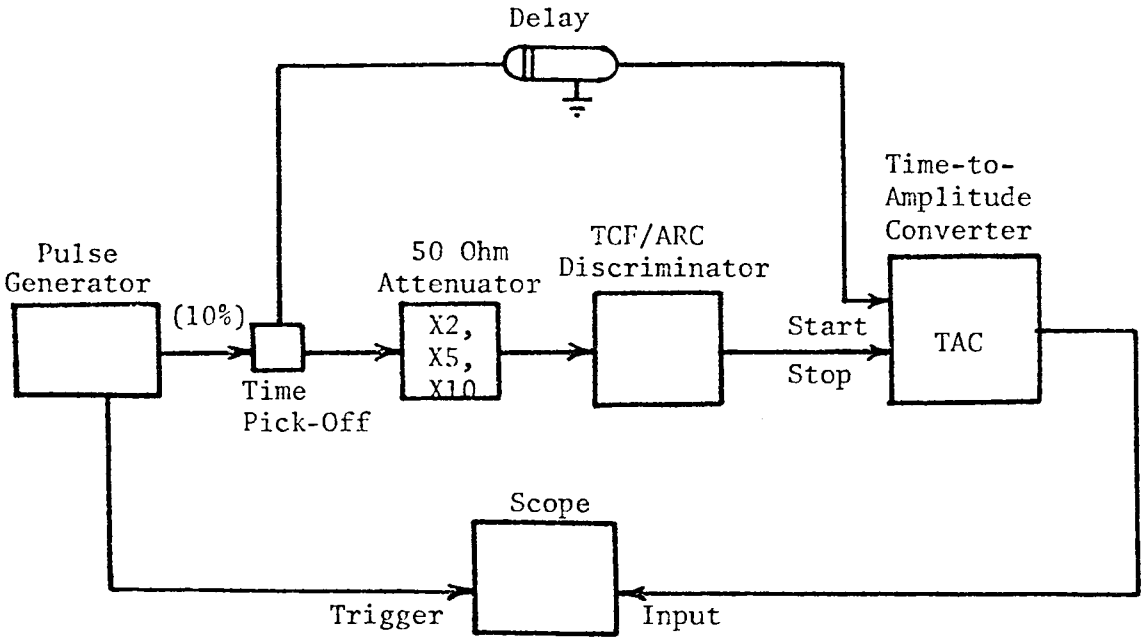


Figure 5.3. Test system for measuring time walk in the discriminator.

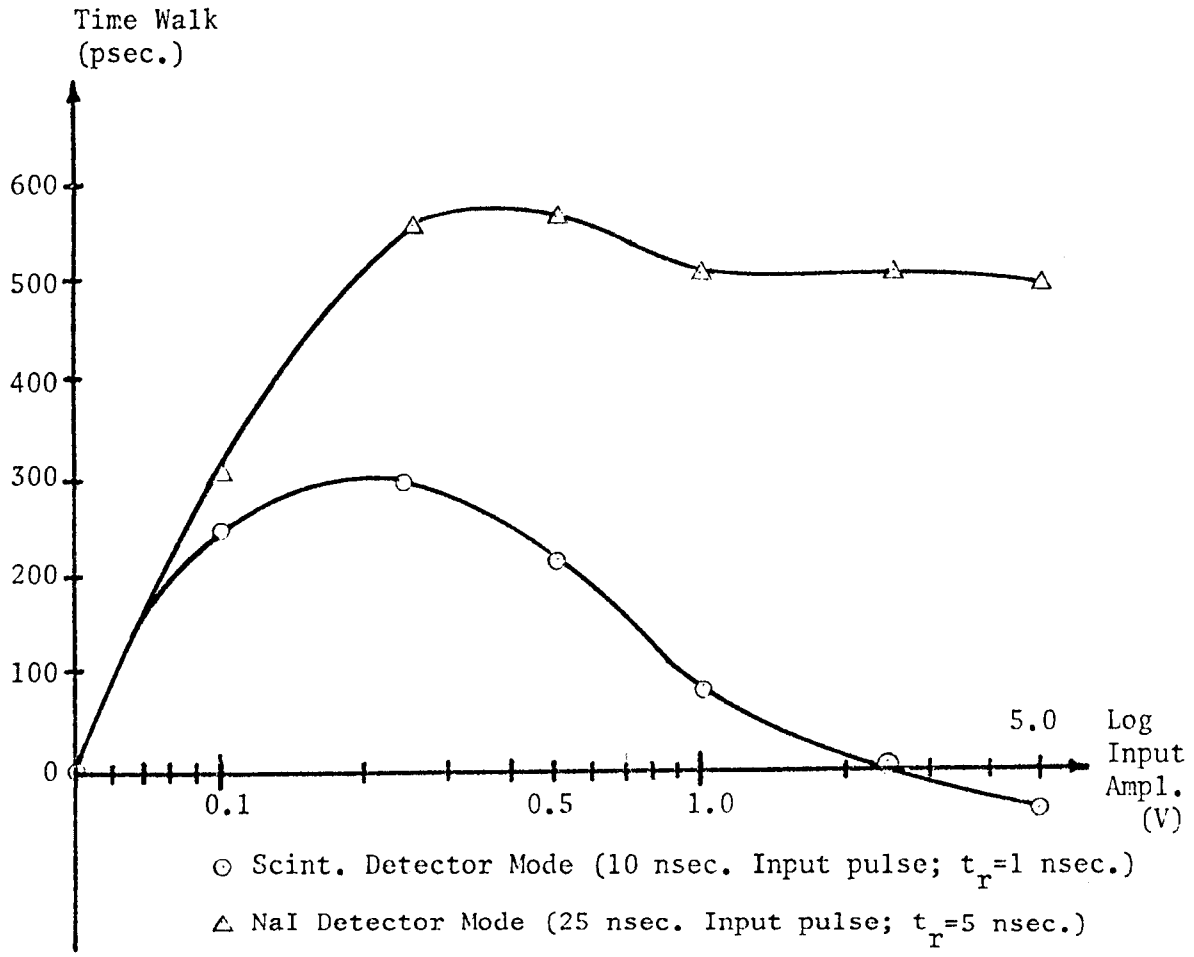


Figure 5.4. Typical time walk curves for the third generation constant-fraction discriminator, with input signals from a pulse generator.

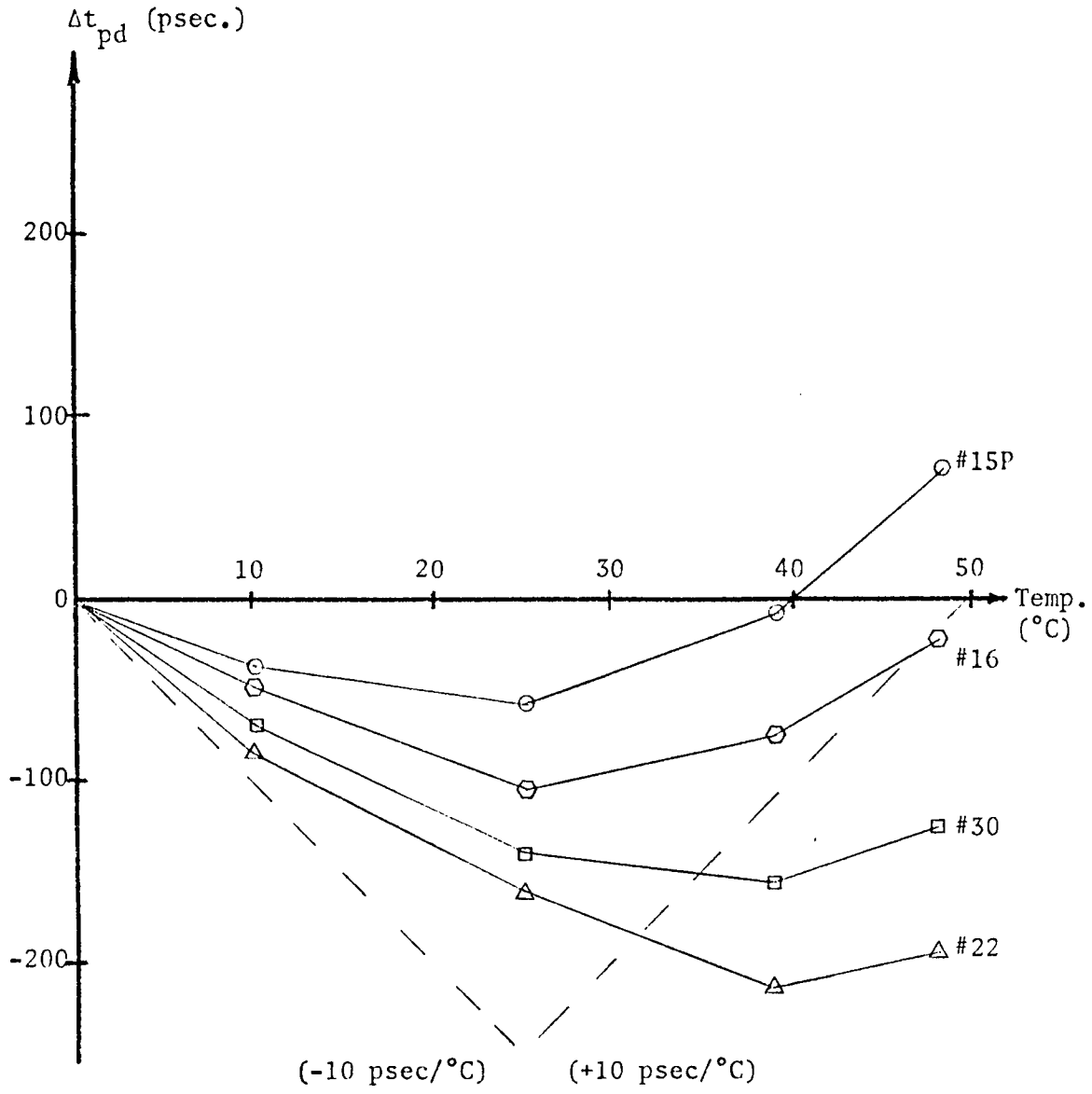


Figure 5.5. Propagation delay variation as a function of temperature for four prototype units.

path and by temperature compensating the reference levels for various MECL line receivers throughout the instrument.

Summary

The constant-fraction discriminator described in this chapter provides ARC timing for a wide variety of detectors. This discriminator can be used with scintillator and photomultiplier detection systems as well as semiconductor detector systems. ARC timing is used to compensate for time walk due to input signal risetimes and to compensate for nonlinearities in the electronics of the constant-fraction circuit. The exceptional temperature stability of the instrument allows it to be used in long-term experiments.

CHAPTER VI

EXPERIMENTAL RESULTS

In this chapter experimental results from a Ge(Li) timing system are given. Timing data are compared for a system in which the Slow-Risetime-Reject (SRT) circuitry is employed and for a system in which it is not used. The SRT circuitry improves timing resolution at the expense of system counting efficiency, by eliminating logic pulses resulting from leading-edge (LE) timing in the ARC discriminator.

A system is shown in this chapter for measuring the distribution of charge pulse risetimes from a Ge(Li) detector. The risetime probability density function for a particular coaxial Ge(Li) detector and amplifier system and for an uncollimated source is shown to be approximately exponential. For this density function, the expression for loss in system county efficiency, derived in Chapter IV, is verified.

Timing Coincidence Measurements

Figure 6.1 shows the system that was used for timing coincidence measurements between gamma-rays detected by a coaxial Ge(Li) detector and those detected by a 1" x 1" cylindrical, KL236 plastic scintillator. Dimensions and other data pertaining to the Ge(Li) detector are given in Appendix A. A ^{22}Na, 10μ Ci source was used for gamma-ray production.

The ^{22}Na isotope decays by positron emission and electron capture through the 1.274 MeV state of ^{22}Ne. Most of these decay events occur with the emission of a positron, which then annihilates to produce a pair

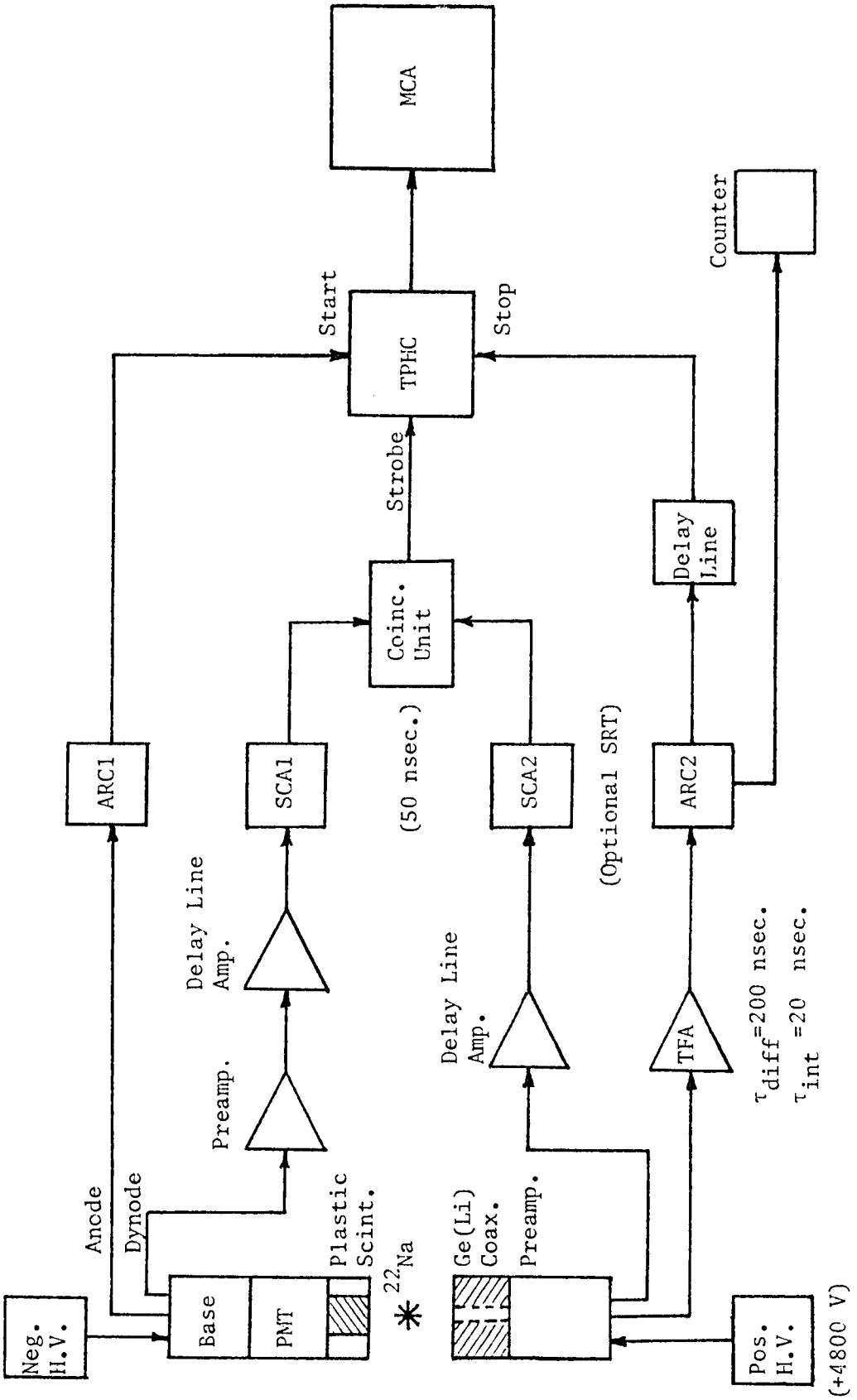


Figure 6.1. Gamma-gamma timing coincidence system, using a Ge(Li) detector and a fast plastic scintillator.

of 0.511 MeV gamma-rays. The two gamma-rays occur virtually simultaneously and propagate from the source with an angular separation of 180 degrees. These rays are then detected by two detectors with a 180 degree physical separation.[30]

Referring to Figure 6.1, light is emitted by the plastic scintillator due to the interaction of one of the pair of 0.511 MeV gamma-rays from the ^{22}Na source. The light is collected by the photo-multiplier tube (PMT), where it is converted to a stream of electrons and amplified. The signal from the anode of the PMT is furnished to the ARC1 timing discriminator, whose output logic pulse is used as the start signal for the time-to-pulse-height converter (TPHC).

The other coincident 0.511 MeV gamma-ray impinges on the coaxial Ge(Li) detector. The detector current signal is integrated by the preamplifier and furnished to the timing-filter amplifier (TFA), where it is shaped and amplified, following the constraints of Equation (3.54), page 57, and Equation (3.55), page 57. The analog output signal from the TFA is provided to the ARC2 timing discriminator, in which the use of the SRT circuitry is optional. The logic signal from this ARC2 discriminator is delayed by a fixed time and used as the stop signal for the TPHC.

A TPHC produces a signal which has an amplitude that is proportional to the time difference between consecutive start and stop input pulses. In the system of Figure 6.1 the timing information in the TPHC is strobed to the output only if the gamma-rays that produced the consecutive start and stop signals were of the desired energy (0.511 MeV) and were

detected simultaneously. These constraints are determined by means of linear side channels. A linear side channel is needed for each detector and is composed of a preamplifier, a shaping amplifier and a single-channel analyzer (SCA). Each SCA selects a range of desired energies around 0.511 MeV and provides a logic signal to the coincidence unit if the energy of the event is within this energy window. The logic signal from the coincidence unit strobes the timing information from the TPHC if the detected gamma-rays were each of the proper energy and if they both occurred within the time window set by the coincidence unit. The latter condition is obtained by matching the propagation delays of the two linear side channels.

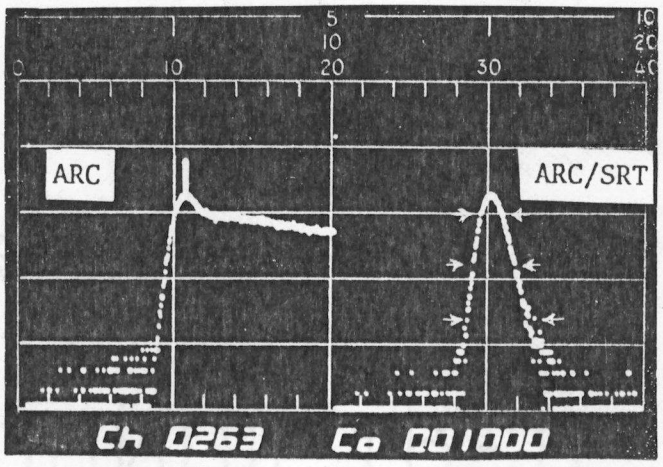
A multichannel analyzer (MCA) is used to accumulate and display the timing information from the TPHC. The display is a probability density function of consecutive start-to-stop time intervals, strobed from the TPHC.

For the system in Figure 6.1, page 134, the time jitter and walk from the plastic scintillator portion of the system is approximately an order of magnitude less than the timing error from the Ge(Li) portion of the system. Thus, the statistical spread in the timing spectra can be attributed to the Ge(Li) timing information.[5]

Figure 6.2 shows six timing spectra obtained with the system in Figure 6.1, for a narrow dynamic range of selected energies (0.511 MeV ± 5%) and for three different threshold settings of the ARC2 discriminator. The spectra on the left were obtained without the use of the SRT circuitry; those on the right were obtained with the use of the SRT circuitry. These

Counts (log)

(a)



FWHM

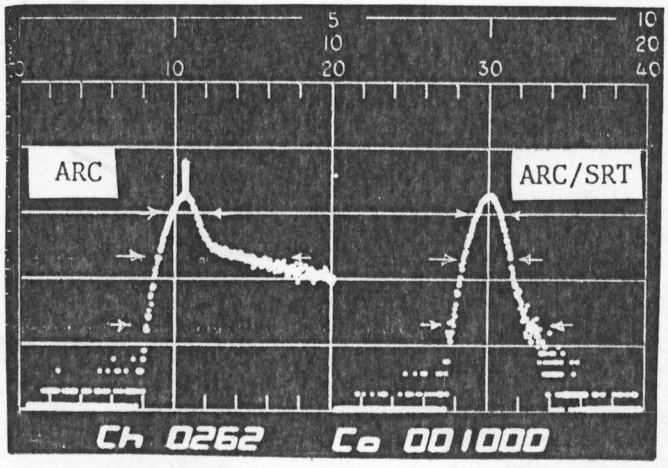
FW(1/10)M

FW(1/100)M

t
(101 psec./ch)

Counts (log)

(b)



FWHM

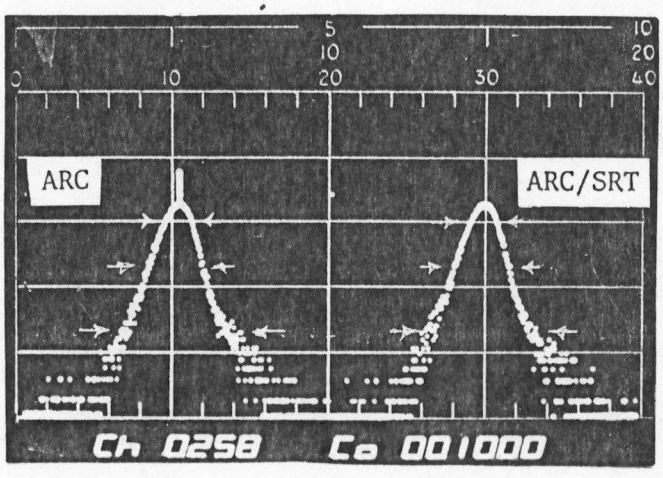
FW(1/10)M

FW(1/100)M

t
(101 psec./ch)

Counts (log)

(c)



FWHM

FW(1/10)M

FW(1/100)M

t
(101 psec./ch)

Figure 6.2. Three decade logarithmic display of timing spectra for an energy window of 0.511 MeV ± 5%: (a) E_{th}=0.35 MeV, (b) E_{th}=0.25 MeV, and (c) E_{th}=0.1 MeV.

spectra are presented for a qualitative view of the effects of the SRT circuitry and the effects of discriminator threshold setting on timing performance. More extensive data are presented later in this section.

The trailing edges of the ARC timing spectra in Figure 6.2 (a) and (b) break away dramatically due to leading-edge timing from the ARC2 discriminator. This phenomenon occurs for a greater percentage of input signals to the ARC2 discriminator as the threshold level is adjusted toward the 0.511 MeV energy level of interest. The input signals that cause leading-edge timing fail to meet the upper-level constraint given by Equation (4.2), page 76, for the ARC2 discriminator. Employing the SRT circuitry eliminates the signal produced by leading-edge timing; the ARC/SRT spectra are approximately normal distribution.

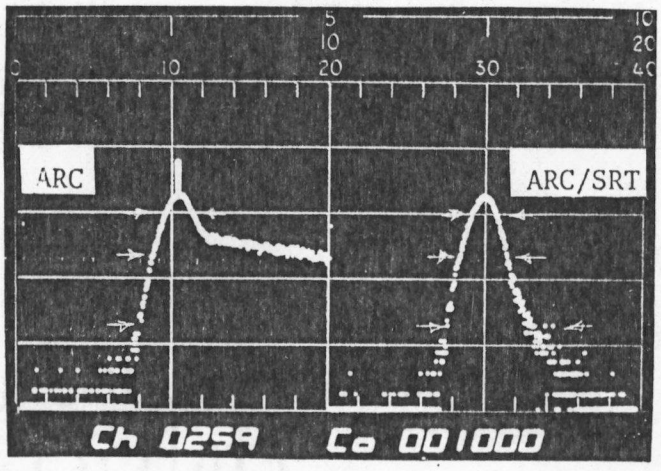
By setting the ARC2 energy discriminator threshold approximately a factor of five below the 0.511 MeV energy level of interest, leading-edge timing is not evident in the ARC timing spectrum of Figure 6.2 (c). Use of the SRT circuitry produces no significant improvement in the timing information for this threshold setting and for the narrow range of energies considered. However, both timing spectra in Figure 6.2 (c) are broader at the full-width at one-half maximum amplitude (FWHM) level than the two previous photographs. This limitation is caused by timing signals generated by noise. The lower-level (LLLE) arming threshold for the ARC2 discriminator is automatically set a factor of two below the energy threshold for the instrument. If the LLLE arming discriminator is allowed to trigger on noise, extraneous timing output signals can be generated.

Figure 6.3 shows similar timing spectra for a 2:1 (0.3 MeV to 0.6 MeV) dynamic range of energies selected by the single-channel analyzers. A greater percentage of input signals to the ARC2 discriminator produce leading-edge timing as the energy threshold level of the discriminator is adjusted toward the energy range of interest. The SRT circuitry can be used to eliminate the pulses caused by leading-edge timing. These spectra indicate worse timing resolution in general than those of Figure 6.2, page 137. This resolution degradation is caused by the increased jitter and walk from the ARC2 timing element, due to the increased range of input signal amplitudes selected for timing.

Figures 6.4 and 6.5 are plots of the timing resolution of the system in Figure 6.1, page 134, as a function of the threshold setting of the ARC2 timing discriminator. These plots are for a 1.1:1 dynamic range of energies (0.511 MeV ± 5%), selected by the side channels. A portion of the data for these plots is shown in the photographs of Figure 6.2, page 137.

The curves of Figure 6.4 were obtained without the use of the SRT circuitry and indicate the degradation of timing resolution due to leading-edge walk in the ARC2 timing discriminator. This timing error increases as the ARC2 discriminator threshold setting nears the 0.511 MeV energy of interest; the increase in error is more evident below the FWHM level. The best timing resolution available from the curves of Figure 6.4 is limited by jitter and by time walk from the constant-fraction element of the ARC2 discriminator, due to risetime variations of the signals from the Ge(Li) detector. At threshold settings of the

Counts (log)



(a)

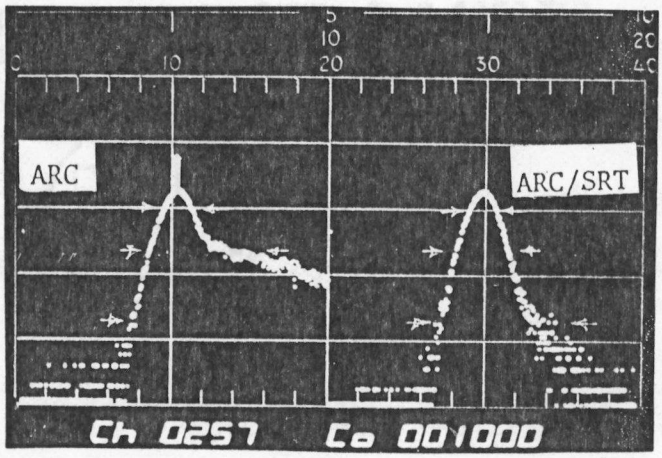
FWHM

FW(1/10)M

FW(1/100)M

t
(101 psec./ch)

Counts (log)



(b)

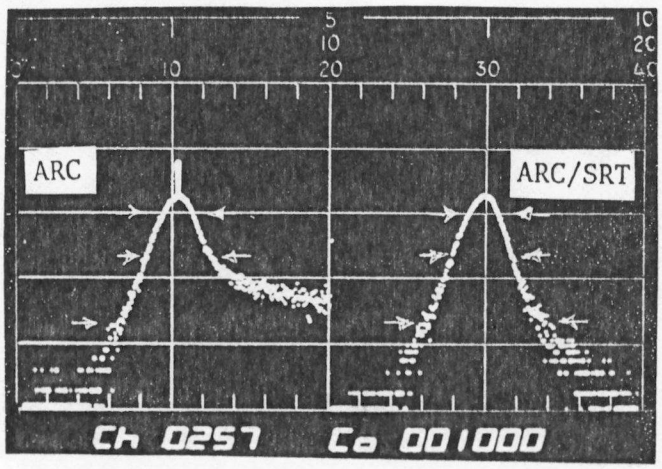
FWHM

FW(1/10)M

FW(1/100)M

t
(101 psec./ch)

Counts (log)



(c)

FWHM

FW(1/10)M

FW(1/100)M

t
(101 psec./ch)

Figure 6.3. Three decade logarithmic display of timing spectra for an energy window of 0.3 MeV to 0.6 MeV and for: (a) E_{th}=0.25 MeV, (b) E_{th}=0.2 MeV, and (c) E_{th}=0.15 MeV.

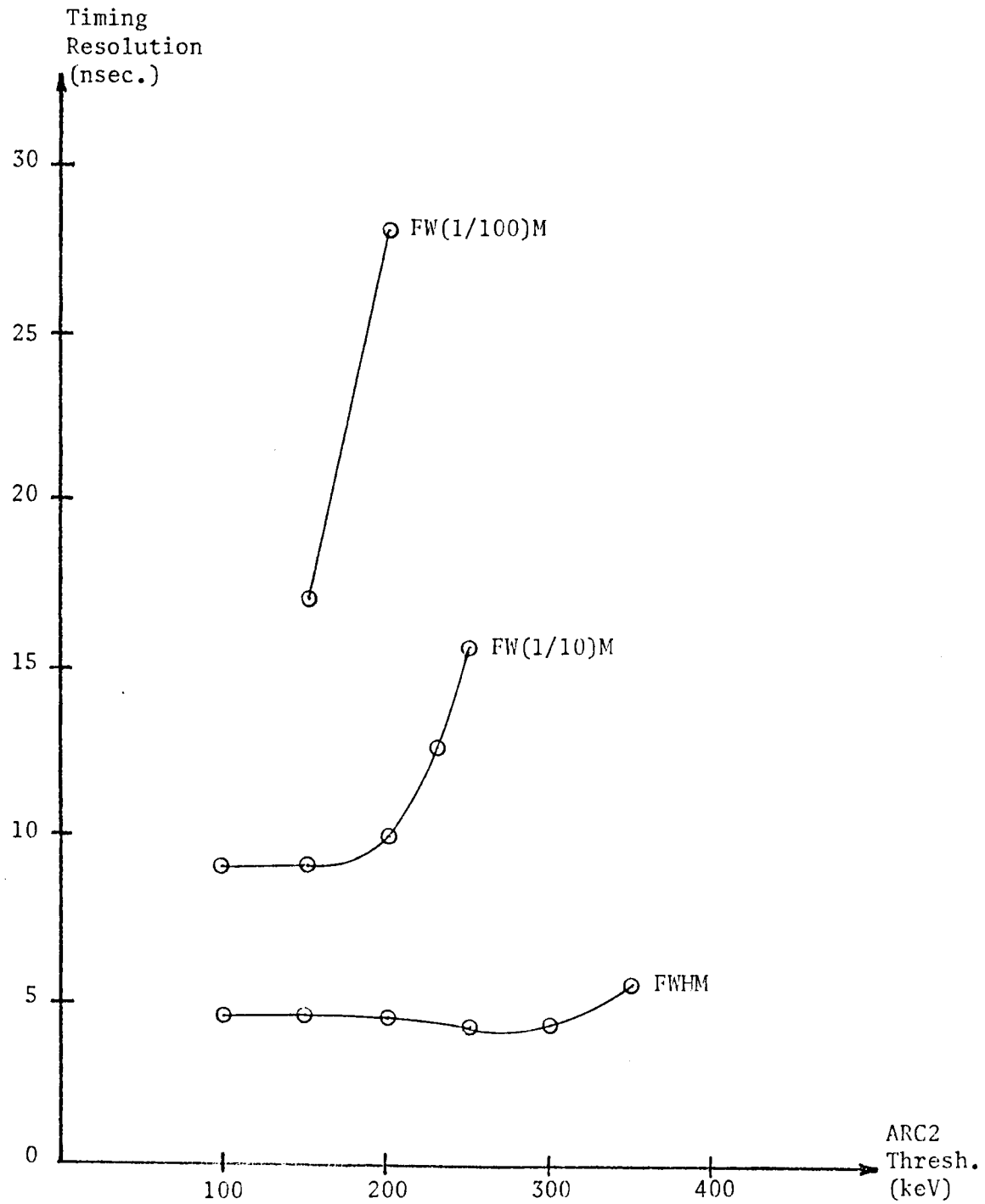


Figure 6.4. System timing resolution as a function of the ARC2 discriminator threshold setting, for a 1.1:1 (0.511 MeV ± 5%) dynamic range of energies; SRT circuitry not employed.

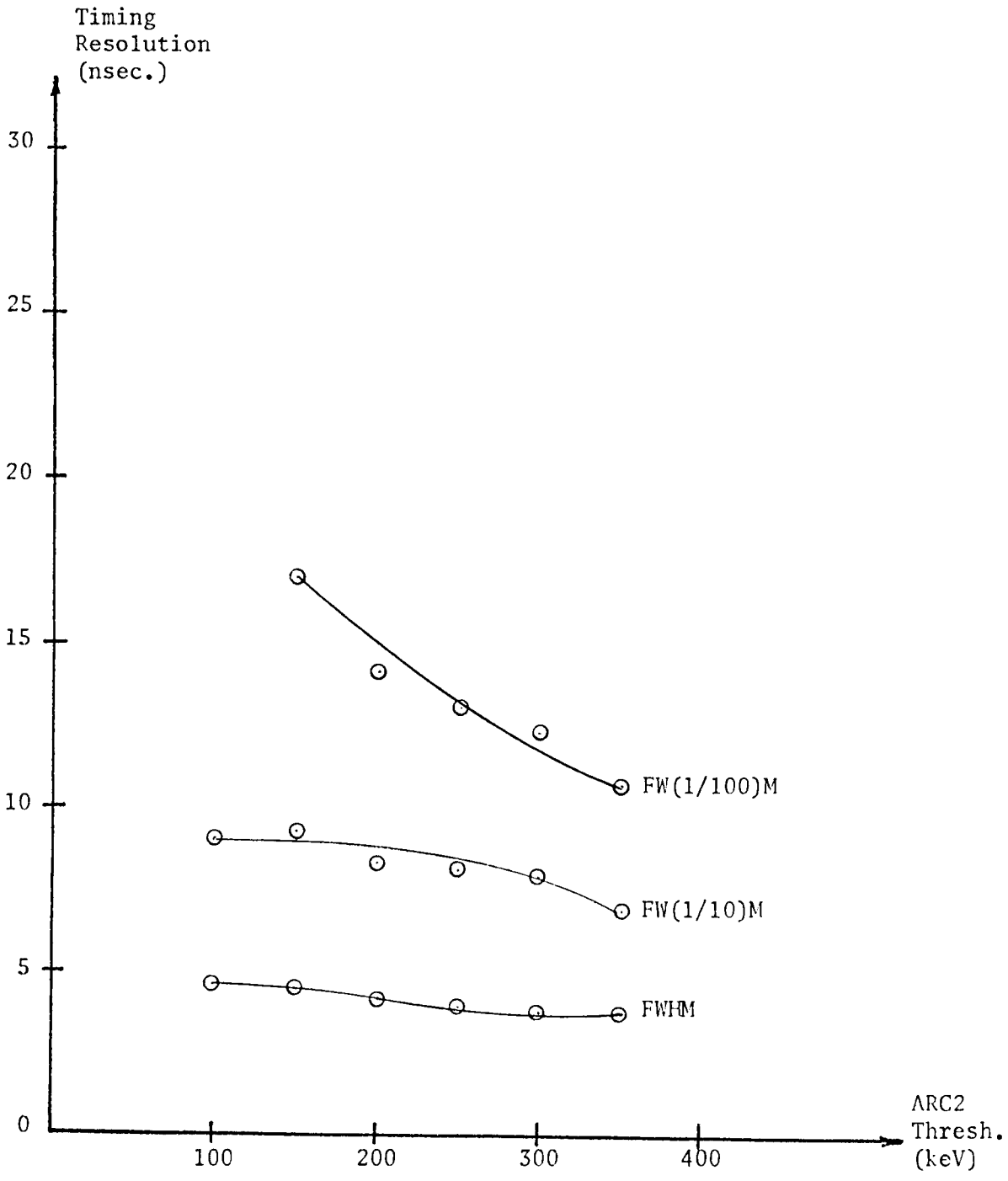


Figure 6.5. System timing resolution as a function of the ARC2 discriminator threshold setting, for a 1.1:1 (0.511 MeV ± 5%) dynamic range of energies; SRT circuitry in use.

ARC2 discriminator below 100 keV, timing resolution is impaired by false triggering of the LLLE arming circuitry and the ARC shaping circuitry on random noise.

The timing resolution curves of Figure 6.5 were obtained with the use of the SRT circuitry. Leading-edge timing signals, which resulted in impaired timing resolution in Figure 6.4, were eliminated. Comparing Figures 6.4 and 6.5 shows that the SRT circuit provides resolution improvement in the full width at one-half maximum amplitude (FWHM) level; this improvement ranges from zero for a 100 keV ARC2 discriminator threshold setting to 33 percent for a 350 keV threshold setting. The resolution improvement in the full width at one-tenth maximum amplitude (FW(1/10)M) level ranges from zero for a 100 keV ARC2 discriminator threshold setting to 48 percent for a 250 keV threshold setting. The SRT circuitry provides an even greater improvement in timing resolution at the full width at one one-hundredth maximum amplitude (FW(1/100)M) level; this improvement rapidly becomes unmeasurable, as evidenced by the photographs of Figure 6.2, page 137.

Figure 6.5 indicates that, when the SRT circuitry is employed, timing resolution improves as the threshold level of the ARC2 discriminator is raised toward the 0.511 MeV energy level of interest. This improvement is the result of the increasing stringency of the risetime constraints placed on the input signals to the ARC2 discriminator by the SRT circuitry. Equation (4.79), page 101, shows that the maximum acceptable risetime, established by the SRT circuitry for a linear input signal, decreases as the threshold level is raised toward the signal

amplitude of interest. Thus, as the acceptable risetime variations of the input signals are reduced, timing error induced by risetime variations is effectively reduced also. In Figure 6.5 the resolution improvement due to increasing the threshold level of the ARC2 discriminator from 150 keV to 350 keV is: (1) 20 percent for the FWHM level, (2) 28 percent for the FW(1/10)M level, and (3) 36 percent for the FW(1/100)M level.

Figures 6.6 and 6.7 are additional plots of timing resolution for the system in Figure 6.1, page 134, as a function of the threshold setting of the ARC2 timing discriminator. These curves represent a 2:1 (0.3 MeV to 0.6 MeV) dynamic range of energies selected by the single-channel analyzers. A portion of the data for these plots is shown in the photographs of Figure 6.3, page 140. Figure 6.6 was obtained without the use of the SRT circuitry, and Figure 6.7 was obtained with the use of the SRT circuitry. The improvements made in timing resolution by using the SRT circuitry and by increasing the ARC2 discriminator threshold, when the SRT circuit was employed, are evident from the plots. Explanations of these improvements follow the same line of reasoning as the explanations for timing improvements given for Figure 6.4, page 141, and Figure 6.5, page 142.

The timing resolution improvements for Figures 6.6 and 6.7 are greater than those for Figures 6.4 and 6.5, over the same range of threshold levels. The wider dynamic range of accepted energies (2:1) and the lower minimum energy of interest (0.3 MeV), used to obtain Figures 6.6 and 6.7, cause greater timing error due to leading-edge walk,

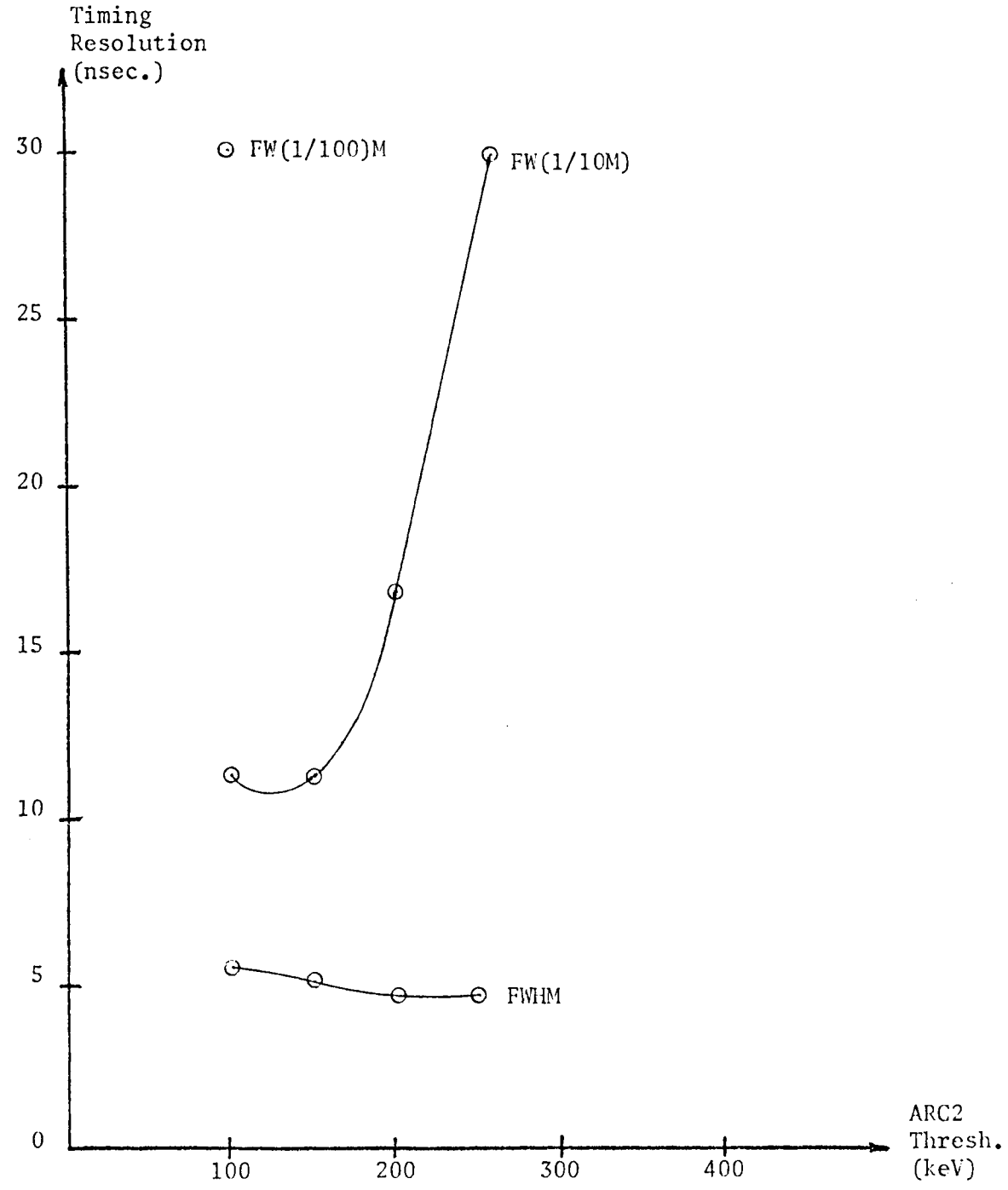


Figure 6.6. System timing resolution as a function of the ARC2 discriminator threshold setting, for a 2:1 (0.3 MeV to 0.6 MeV) dynamic range of energies; SRT circuitry not employed.

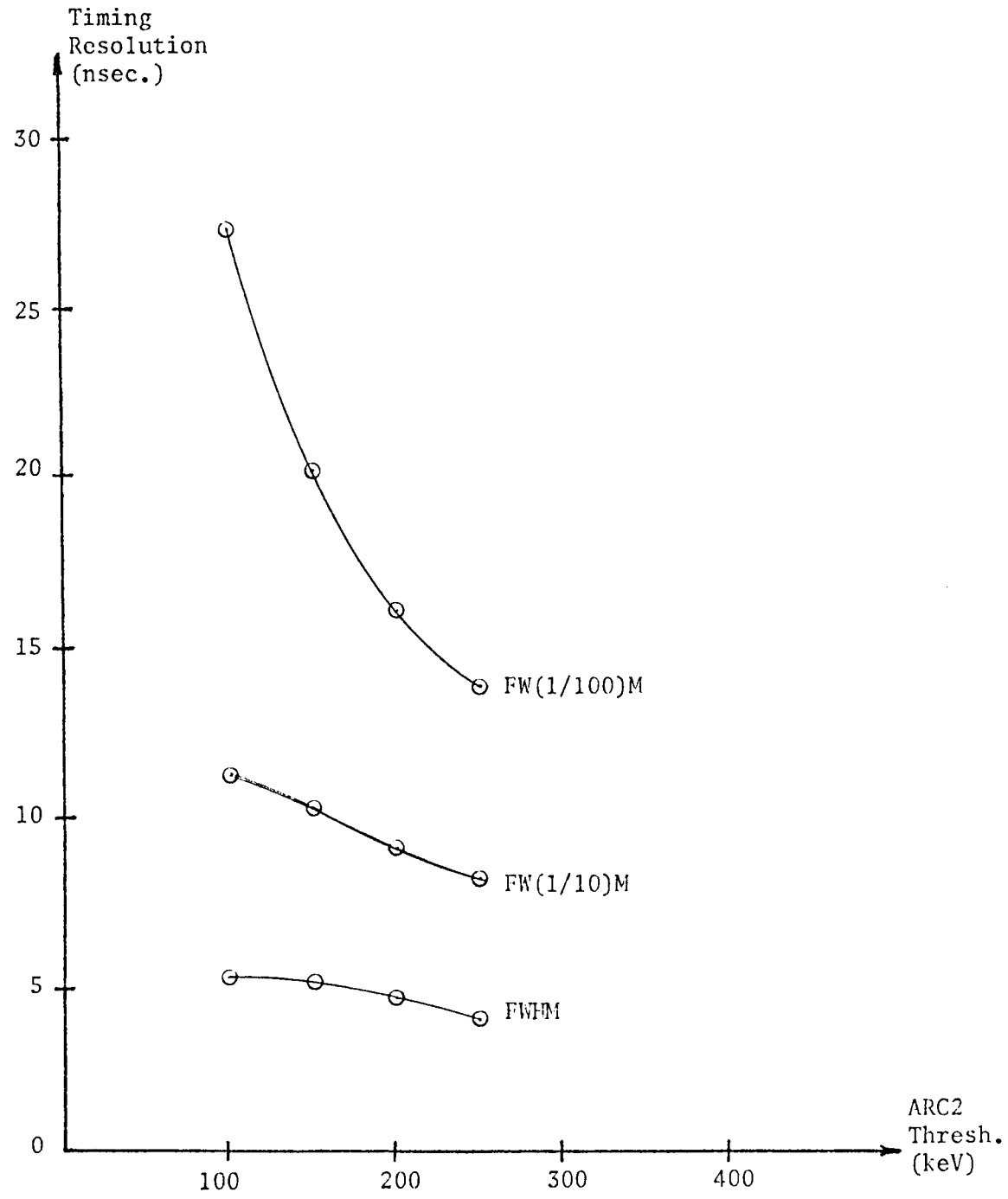


Figure 6.7. System timing resolution as a function of the ARC2 discriminator threshold setting, for a 2:1 (0.3 MeV to 0.6 MeV) dynamic range of energies; SRT circuitry in use.

for ARC timing without the SRT circuitry. Thus, the resolution improvements made in the timing spectra by eliminating leading-edge timing pulses are greater for the wider dynamic range experiment than for the narrower dynamic range experiment.

Below the FWHM level, errors in timing for the system in Figure 6.1, page 134, can be attributed primarily to the risetime variations of the pulses from the Ge(Li) detector. These errors can be significantly reduced by employing the SRT circuitry and by then raising the threshold level of the ARC2 discriminator toward the energy range of interest. The improvements in timing are made at the expense of system counting efficiency. Use of the SRT circuitry places stringent risetime constraints on the input signals to the ARC2 discriminator, to insure ARC timing and not leading-edge timing from the instrument. The risetime variations of the input signals to the ARC2 discriminator are examined in the following section.

Distribution of Risetimes

Use of the SRT circuitry in the ARC2 timing discriminator causes a reduction in the counting efficiency of the discriminator. Thus, a reduction in counting efficiency is introduced into the timing system of Figure 6.1, page 134. A knowledge of the risetime probability density function for signals from the Ge(Li) detector is essential in determining the efficiency loss for the system. The necessity of knowing this density function was discussed in Chapter IV, where analytical expressions for efficiency loss were derived.

The system shown in Figure 6.8 was devised to measure the risetime probability density function for signals applied to the ARC2 discriminator in Figure 6.1, page 134. The risetimes of these signals can be made equal to the risetimes of the pulses from the Ge(Li) detector, as discussed in Chapter III.

In the system shown in Figure 6.8, impinging radiation produces a current pulse from the Ge(Li) detector. The current pulse is integrated and amplified by the preamplifier and then provided to the timing-filter amplifier (TFA). The TFA amplifies and shapes the signal, following the constraints for shaping time constants given in Equation (3.54), page 57, and Equation (3.55), page 57. The analog output signal from the TFA is provided to two leading-edge discriminators, LE1 and LE2. The LE1 discriminator is adjusted to trigger at a level that is equal to 10 percent of the energy of interest; the LE2 discriminator is adjusted to fire at 90 percent of the selected energy. These two discriminators furnish, respectively, the start and stop signals for the time-to-pulse-height converter (TPHC).

A linear side channel, composed of a shaping amplifier and a single-channel analyzer (SCA), selects a very narrow range of energies around the energy level of interest. The SCA output signal strobes the risetime information from the TPHC, if the detected radiation was within the selected energy range. A multichannel analyzer (MCA) accumulates and displays the timing information strobed from the TPHC.

The timing information displayed by the MCA is the probability density function of 10 percent to 90 percent risetimes for signals from

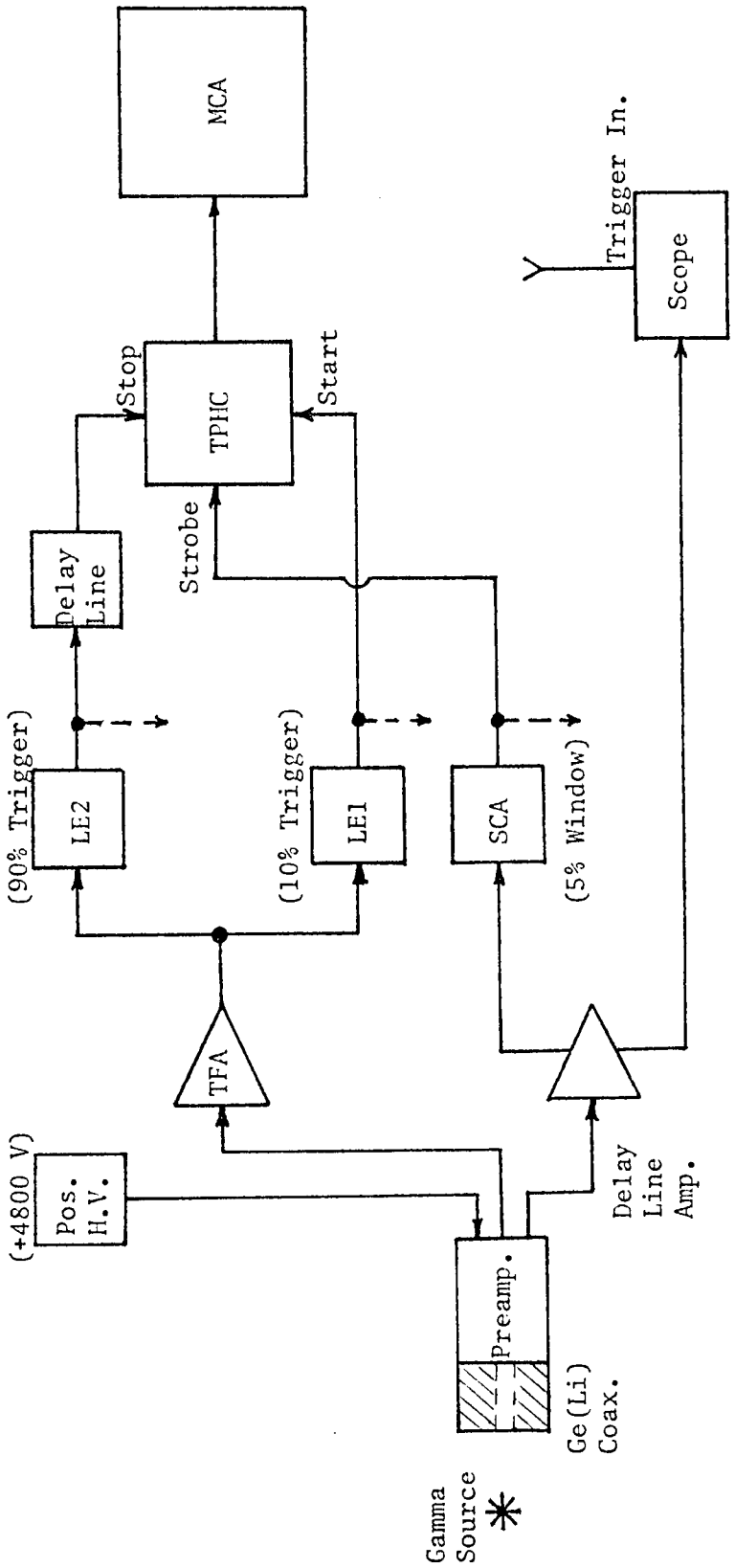


Figure 6.8. System for measuring risetime probability density functions for signals from a coaxial Ge(Li) detector.

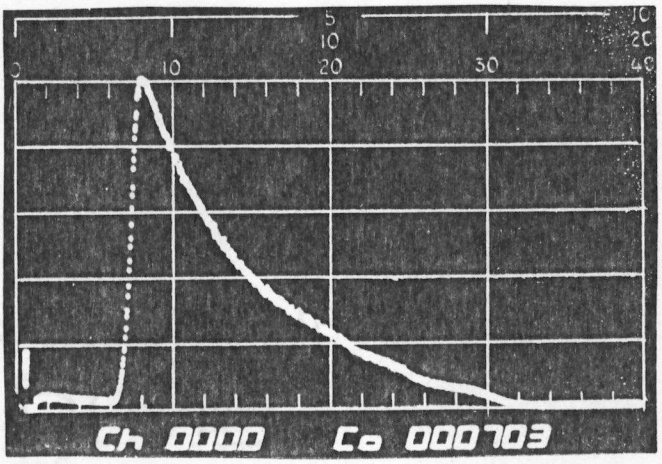
the Ge(Li) detector and amplifier system. The measurement technique indicated in Figure 6.8 allows a risetime density function to be determined for signals corresponding to events of a particular energy; it is not applicable to a wide dynamic range of signals.

Figures 6.9 and 6.10 show four risetime probability density functions that were obtained with the system shown in Figure 6.8. The photographs of Figure 6.9(a) and 6.9(b) show the risetime distributions for detector signals corresponding, respectively, to the 0.511 MeV and to the 1.274 MeV energy levels of ^{22}Na. The photographs of Figure 6.10(a) and 6.10(b) represent the risetime probability density functions for detector signals corresponding, respectively, to the 1.174 MeV and to the 1.333 MeV energy levels of ^{60}Co. The scale factors are identical for all four photographs. The vertical scales are linear, with 10,000 counts in each peak, and the horizontal scales are each linear, at 160 psec./channel. In each experiment the SCA was set for a 5 percent energy window around the energy level of interest. Numerical data corresponding to the risetime density functions in Figures 6.9 and 6.10 are given in Table I.

From the spectra shown in Figures 6.9 and 6.10, one can conclude that shorter risetime signals from the Ge(Li) detector in this configuration are more probable than longer risetime signals. However, the risetimes vary upward in value by as much as 100 nsec, from some minimum value. The minimum risetime cannot be measured exactly, but the minimum observed 10 percent to 90 percent risetime of the pulses from the Ge(Li) detector is in the order of 40 nsec. to 50 nsec.

P [t_R(10%-90%)]
(Counts)

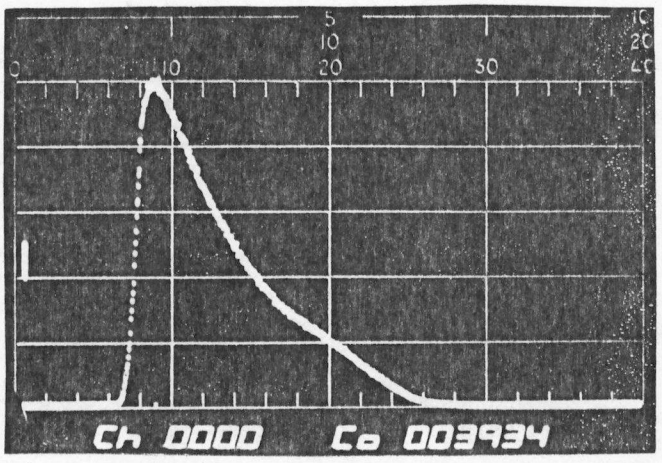
(a)



t_R
(160 psec./ch)

P [t_R(10%-90%)]
(Counts)

(b)

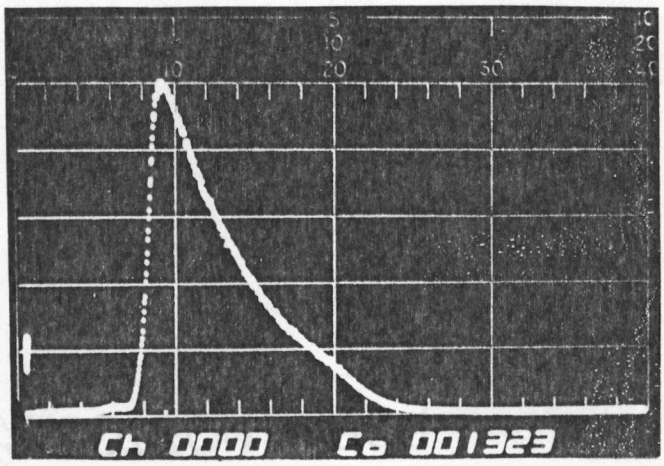


t_R
(160 psec./ch)

Figure 6.9. Probability density functions of 10 percent to 90 percent risetimes for signals from a coaxial Ge(Li) detector-amplifier system for: (a) the 0.511 MeV photopeak of ^{22}Na, and (b) the 1.274 MeV photopeak of ^{22}Na.

P [t_R(10%-90%)]
(Counts)

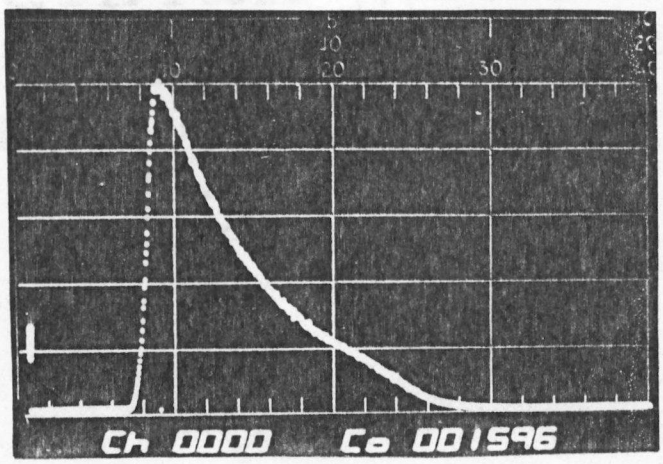
(a)



t_R
(160 psec./ch)

P [t_R(10%-90%)]
(Counts)

(b)



t_R
(160 psec./ch)

Figure 6.10. Probability density functions of 10 percent to 90 percent risetimes for signals from a coaxial Ge(Li) detector-amplifier system for: (a) the 1.174 MeV photopeak of ^{60}Co, and (b) the 1.333 MeV photopeak of ^{60}Co.

TABLE I

DATA FOR THE RISETIME PROBABILITY DENSITY SPECTRA

Measurement Levels	^{22}Na (Gamma Source)		^{60}Co (Gamma Source)	
	0.511 MeV	1.274 MeV	1.174 MeV	1.333 MeV
FWHM	23.7 nsec.	25.3 nsec.	22.2 nsec.	23.5 nsec.
FW(1/ε)M	34.7	33.6	29.4	32.5
FW(1/10)M	75.8	64.8	55.7	66.9
FW(1/100)M	104	82.2	76.2	86.1

Each of the four risetime probability density functions shown in Figure 6.9 or in Figure 6.10 is a decaying exponential with multiple decay time constants. To the first order, each spectrum can be approximated by a single time constant exponential of the form of Equation (4.95), page 112. The decay time constant for an exponential of this form can be measured directly; it is equal to the elapsed time from the beginning of the exponential until the function has dropped to the fraction $1/\varepsilon$ (approximately 0.37) of its maximum amplitude. Table I gives the measured values that approximate the single decay time constants for the risetime distributions as the $FW(1/\varepsilon)M$ values. The average value of these decay time constants is 32.6 nsec. None of the measured values differs from the average time constant value by more than 10 percent. For a decaying exponential of the form of Equation (4.95), this measurement incorporates approximately 63 percent of the total number of events for each spectrum.

Several generalizations may be drawn from the previous discussion. Under the presented test conditions, the 10 percent to 90 percent risetime probability density function for signals from the coaxial Ge(Li) detector-amplifier system can be approximated by a single time constant decaying exponential. The density function is valid for photopeaks of energy produced by Gamma-rays in the 0.5 MeV to 1.4 MeV range; it is also independent of energy in this energy region. The sources of gamma-rays for the experiments were uncollimated and were placed at the end of the cylindrical coaxial detector, as described in the Appendix.

The timing system shown in Figure 6.1, page 134, suffers a loss in counting efficiency when the SRT circuitry in the ARC2 discriminator is employed. This efficiency loss can be calculated, using the results of the experimentally determined risetime probability density function. Experimental and calculated curves for efficiency loss are compared in the following section.

System Counting Efficiency Loss

In Chapter IV analytical expressions were derived to indicate how the use of the Slow-Risetime-Reject (SRT) circuitry affects the counting efficiency of the ARC timing discriminator under study. This section of the dissertation shows the correlation between the analytical results and the experimental data accumulated for efficiency loss.

Equation (4.102), page 117, represents the loss in counting efficiency of the discriminator at a particular energy level, E_2, as a function of threshold level. This loss is due to the use of the SRT circuitry, which rejects logic pulses resulting from leading-edge timing. In deriving Equation (4.102), all input signals to the discriminator were assumed to be linear. The risetime probability density function for input signals was approximated by a single time constant decaying exponential of the form of Equation (4.95), page 112. The risetimes represented in these expressions are the 10 percent to 90 percent risetimes for linear signals; the decay time constant, τ_R, is for an exponential density function of 10 percent to 90 percent risetimes

An experimental determination of the value of τ_R is recorded in the previous section. For the detector described in the Appendix and for

gamma-rays in the energy range from 0.5 MeV to 1.4 MeV, the average value of τ_R was seen to be

$$\tau_R = 32.6 \text{ nsec.} \tag{6.1}$$

Other numerical values to be used in the expression for efficiency loss are determined by the constant-fraction discriminator used to obtain experimental data. The constant-fraction shaping delay, t_d, was chosen for ARC timing with Ge(Li) detectors. This Ge(Li) mode shaping delay is

$$t_d = 14 \text{ nsec.} \tag{6.2}$$

for the commercially available unit described in Chapter V. The attenuation factor f, for the unit, is

$$f = 0.32 \text{ .} \tag{6.3}$$

Substituting these values for delay and attenuation into Equation (4.24), page 83, yields the ARC zero-crossing time for linear input signals applied to an ideal constant-fraction discriminator as

$$t_{ARC2} = 20 \text{ nsec.} \tag{6.4}$$

The fixed delay t_k, discussed in Chapter IV, is the difference in the effective propagation delay between the signal from the upper-level discriminator in the commercial unit and the signal from the zero-crossing gate. This value was experimentally determined to be approximately

$$t_k \approx 19 \text{ nsec.} \tag{6.5}$$

Note that this value of t_k satisfies the constraint of Equation (4.40), page 87, for linear input signals. In Chapter IV the constraint of Equation (4.40) was shown to insure that the SRT circuitry could be used to eliminate logic pulses generated by leading-edge timing in the third generation discriminator.

Using Equations (6.4) and (6.5) in Equation (4.80), page 101, yields the value for the term t_{b2} in the expression for efficiency loss, or

$$t_{b2} \approx 39 \text{ nsec.} \tag{6.6}$$

Equations (6.1) and (6.6) are used in Equation (4.102), page 117, to obtain the expression for the loss in counting efficiency of the discriminator at a particular energy as

$$P_{2\varepsilon(\text{loss})}(E_{th}) = \begin{cases} \varepsilon^{-\left(\frac{0.8\,E_2}{E_{th}}(39\times10^{-9})-T_R\right)/32.6\times10^{-9}} & , 0 \leq P_{2\varepsilon(\text{loss})}(E_{th}) \leq 1 \\ 1 & , E_{th} > E_2 \end{cases} . \tag{6.7}$$

The remaining risetime term, T_R, in Equation (6.7) represents the minimum observed 10 percent to 90 percent risetime for input signals to the discriminator. This minimum risetime cannot be determined precisely from an oscilloscope due to the random nature of the detected events. Therefore, T_R can be evaluated by fitting Equation (6.7) to the

experimental data at one point. Later in this section, Equation (6.7) is plotted on the same graph as the experimental data, for ease of comparison.

Figure 6.11 is a block diagram of the system used to measure the loss in counting efficiency of the constant-fraction discriminator with SRT circuitry. Incident radiation is processed by the Ge(Li) detector and the preamplifier, as previously discussed. The signal from the preamplifier is further amplified and shaped by a delay-line shaping amplifier to insure accurate transfer of the energy information to the multichannel analyzer (MCA). The MCA accumulates the amplitude information from the shaping amplifier and displays the data as a probability density of detected energies.

In the system of Figure 6.11, the MCA is gated by the ARC timing discriminator to accept information from the shaping amplifier. This means that each signal from the detector and preamplifier must pass the threshold and risetime constraints of the ARC discriminator before it is processed by the MCA. The ARC discriminator in this system is the unit under study in this dissertation. If the SRT circuitry in this discriminator is employed, the energy distribution displayed by the MCA is modified relative to the actual energy probability density. The discussion in Chapter IV indicates that those events with energies near the threshold of the ARC discriminator are less likely to produce a discriminator output signal than those events whose energies greatly exceed the threshold.

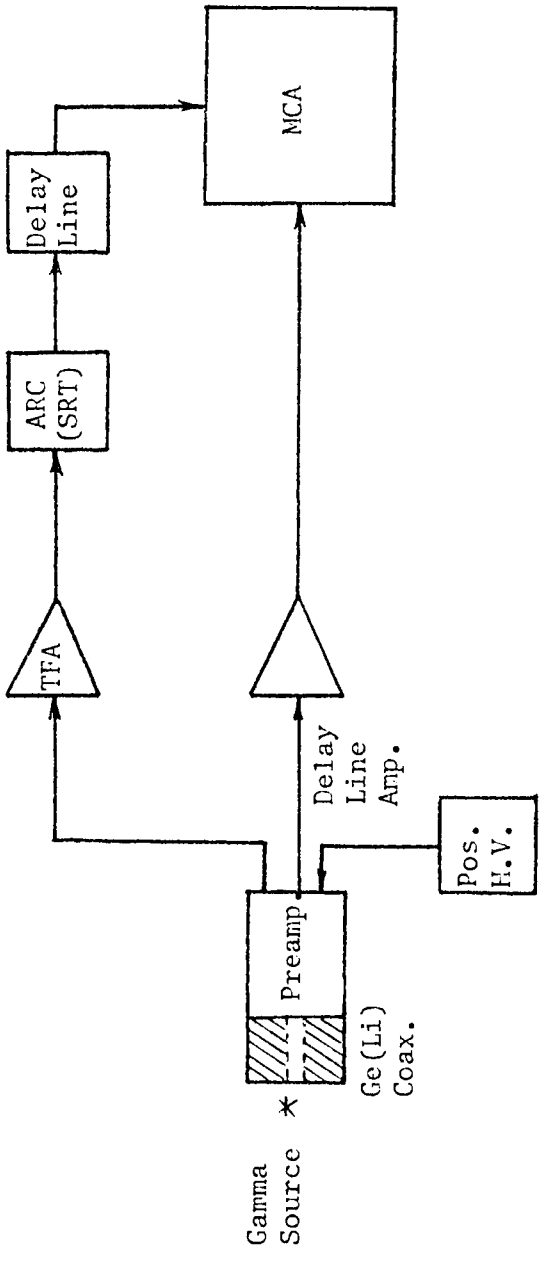


Figure 6.11. System used for gated energy analysis.

The photographs in Figure 6.12 are energy spectra obtained with the system in Figure 6.11. These spectra are presented to illustrate the loss in counting efficiency of the discriminator near threshold when the SRT circuitry is employed. The vertical scales in these distributions are logarithmic and the horizontal scales are linear. The accumulation time was 100 seconds for each spectrum to allow a channel by channel comparison of efficiency.

Figure 6.12(a) is an ungated energy spectrum for a 10μ Ci, ^{60}Co gamma-ray source. In this spectrum, all the information from the shaping amplifier was accepted and processed by the MCA. This distribution represents the true probability density of detected energies. There are two distinct, narrow peaks toward the higher energies of the distribution; these characteristics are called the 1.174 MeV and 1.333 MeV photopeaks. The relatively flat distribution toward the lower energies is known as the Compton distribution.

Figure 6.12(b) is the energy spectrum, gated by the ARC discriminator without the use of the SRT circuitry. In this case, each event whose energy exceeds the threshold of the ARC discriminator is analyzed by the MCA. The energy level of the discriminator threshold is the left-hand vertical edge of the spectrum; the value of this energy threshold is approximately 260 keV. Above the threshold level there is no apparent loss in the number of counts in each channel, relative to the previous photograph. Thus, when the SRT circuitry is not employed, there is no loss in the counting efficiency of the discriminator for events above threshold level.

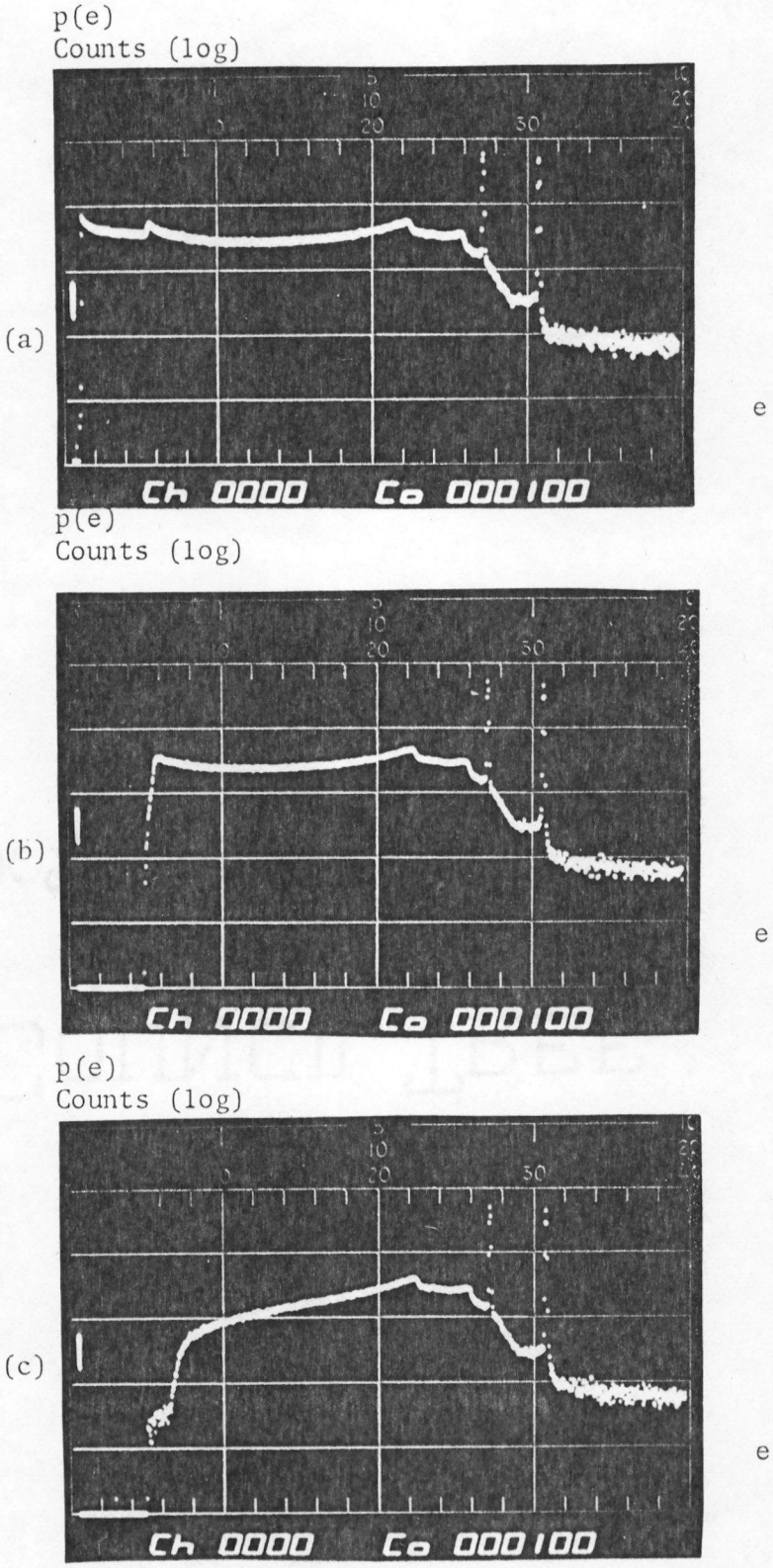


Figure 6.12. Five decade logarithmic display of a gamma-ray energy distribution for ^{60}Co with a coaxial Ge(Li) detector: (a) ungated, (b) gated by ARC discriminator without SRT circuitry, and (c) gated by ARC discriminator with SRT circuitry.

The gated ^{60}Co energy spectrum for ARC timing obtained with the SRT circuitry is shown in Figure 6.12(c). Relative to the two previous photographs, the loss in the counting efficiency of the discriminator is evident. The loss in counts in each channel is much more severe for events with energies only slightly exceeding the threshold level. This loss is a result of the severe risetime constraints placed by the SRT circuitry on the input signals to the constant-fraction discriminator. The analytical results for a flat energy distribution are shown in Figure 4.8, page 116.

Determining the efficiency loss at a particular energy requires an evaluation of spectra similar to Figures 6.12(b) and 6.12(c). Each of these spectra is accumulated for an identical period of time and the numbers of counts in the channel corresponding to the energy of interest are compared. Plotting the loss in efficiency at a particular energy as a function of threshold level requires that this procedure be performed for several different discriminator threshold settings.

Figure 6.13 shows plots of the loss in counting efficiency at a particular energy as a function of threshold level. The efficiency loss results from employing the SRT circuitry in the ARC discriminator. The solid curve in Figure 6.13 is a plot of the calculated efficiency loss at energy E_2, from Equation (6.7), page 157. Fitting the calculated curve to an efficiency loss of 55 percent at a normalized threshold level of 0.5 yields the approximate value of the minimum 10 percent to 90 percent risetime, T_R of the input signals to the discriminator, or

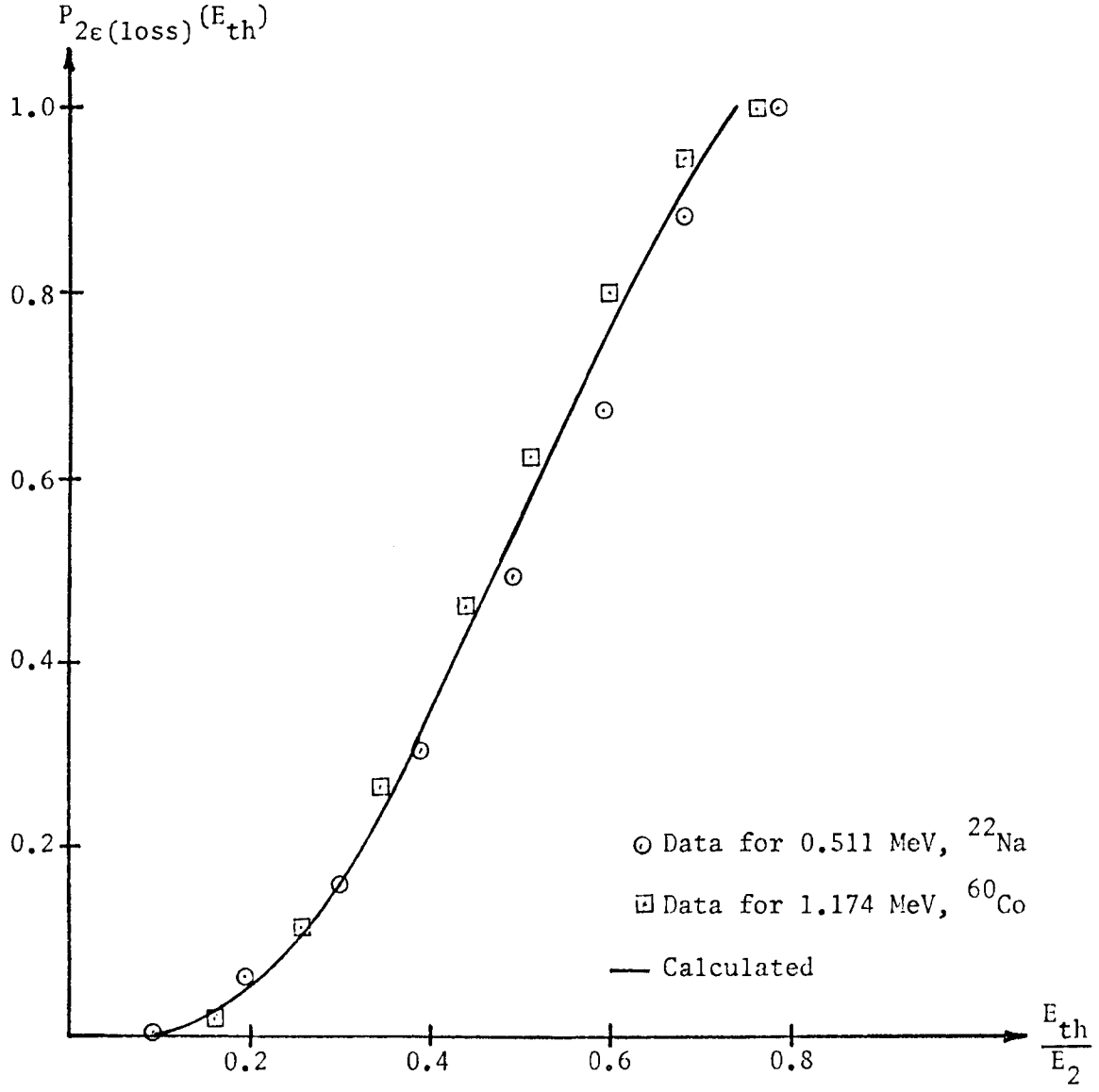


Figure 6.13. Loss in the counting efficiency of the commercial discriminator, as a function of threshold, for the 0.511 MeV photopeak of ^{22}Na and the 1.174 MeV photopeak of ^{60}Co.

$$T_R \approx 43 \text{ nsec.} \qquad (6.8)$$

The remainder of the calculated curve is plotted using the value of T_R from Equation (6.8) in Equation (6.7). Actual values of the loss in counting efficiency of the discriminator are also shown in Figure 6.13. The circled data points represent efficiency loss for the 0.511 MeV photopeak of ^{22}Na. Counting efficiency loss for the 1.174 MeV photopeak of ^{60}Co is shown by the data points within the squares. The value of T_R which positions the calculated curve was selected to approximately bisect the curves for the two sets of measured data.

The data in Figure 6.13 indicate a very close correlation between the calculated and the actual loss in counting efficiency for the discriminator under consideration. Comparing the normalized threshold levels at which the loss in counting efficiency becomes total yields approximately a 7 percent difference between calculated and actual values.

Conclusions can be drawn from the data in this section. Calculations for efficiency loss can be made with excellent accuracy by assuming that the signals from the coaxial Ge(Li) detector-amplifier system are linear, with an exponential risetime probability density function. The minimum signal risetime and the characteristic decay time constant of the risetime probability density function must be determined for each detector system. Other constants in the expression for efficiency loss are determined by the ARC discriminator.

Summary

Chapter VI presents resolution measurements for a gamma-gamma timing coincidence system, using the 0.511 MeV events from ^{22}Na. The detectors were a 1" x 1", cylindrical, KL236 plastic scintillator mounted on an RCA 8575 phototube and a 10.3 percent efficient, 58.6 cc, true coaxial Ge(Li) detector. The Ge(Li) timing channel utilized a commercially available ARC discriminator with optional SRT circuitry. Use of the SRT circuitry produced an improvement of 33 percent in the FWHM timing resolution for a 1.1:1 dynamic range of signals and a 350 keV threshold setting. An improvement of 48 percent was realized in the FW(1/10)M timing resolution, for a 1.1:1 dynamic range and a 250 keV threshold setting. These data, combined with photographs of the approximately normal timing distributions obtained when using the SRT circuitry, indicate that the SRT circuitry eliminates logic pulses resulting from leading-edge timing in the ARC discriminator.

A decrease in counting efficiency is a price paid for the improved timing resolution. The SRT circuitry rejects some events, based on risetime, that do have sufficient amplitude to exceed the energy threshold. From Chapter IV, calculation of the counting efficiency loss of the discriminator requires a knowledge of the distribution of rise-times from the detector. In this chapter a system is shown that was devised to measure the probability density function of 10 percent to 90 percent risetimes for the signals from the detector-amplifier system. This density function is shown to be a decaying exponential with an average decay time constant of approximately 32.6 nsec., for the

detector and amplifier system tested. The decay time constant varied less than 10 percent from the average value for gamma spectrum photopeaks in the energy range from 0.5 MeV to 1.4 MeV.

Using the experimentally determined risetime probability density function, the loss in counting efficiency of the ARC discriminator was calculated, assuming linear input signals. The efficiency loss at a particular energy was plotted as a function of the normalized threshold level. This loss curve was plotted on the same axes as the measured data for efficiency loss in the 0.511 MeV photopeak of ^{22}Na and the data for efficiency loss in the 1.174 MeV photopeak of ^{60}Co. The actual and calculated values of the normalized threshold, at which efficiency loss becomes total, differ by only 7 percent. These comparisons indicate the validity of the assumptions used in calculating efficiency loss for this detector.

CHAPTER VII

CONCLUSIONS

Summary

The object of this dissertation was to study the application of a refined version of the constant-fraction technique to a Ge(Li) timing system. Compared to a typical second-generation constant-fraction discriminator, three fundamental design improvements are incorporated in the refined instrument.

The first design improvement is in the arming technique for the zero-crossing detector. A separate lower-level leading-edge (LLLE) discriminator is employed to arm the zero-crossing device, which senses the crossover of the constant-fraction signal. The threshold level for the LLLE discriminator is automatically set at one-half the minimum energy level required to produce an output pulse from the instrument. Thus, input signals that reach the minimum level of interest exceed the LLLE threshold by a factor of two. Leading-edge walk introduced at the zero-crossing detector is reduced for input signals with amplitudes only slightly exceeding the minimum energy requirement.

The second design improvement in the constant-fraction implementation is a fixed delay, t_k, in the path of the timing logic pulse from the zero-crossing detector. An upper-level leading-edge (ULLE) discriminator determines the minimum signal amplitude of interest and arms a coincidence gate for the detection of the delayed timing logic pulse. After the zero-crossing time of the constant-fraction signal, the delay t_k allows

approximately 19 nsec. for the input signal to trigger the ULLE discriminator. If the ULLE arming signal arrives at the gate after the 19 nsec. interval, leading-edge walk occurs at the coincidence gate.

The third basic design improvement is the addition of a Slow-Risetime-Reject (SRT) circuit. This SRT circuit can be employed to evaluate the delayed timing logic pulse and the ULLE signal at the coincidence gate. If the signal from the ULLE discriminator arrives at the coincidence gate prior to the delayed timing pulse, the output signal from the gate is processed to the output of the instrument. Logic signals from the coincidence gate are rejected if the delayed timing pulse arrived at the gate prior to the ULLE signal.

The SRT circuitry is intended for use with Ge(Li) detectors and other similar semiconductor detectors that have wide variations in charge collection times. These variations in charge collection times cause variations in the pulse shapes of the input signals to a constant-fraction timing discriminator. Timing performance is affected because pulse shape variations introduce changes in the zero-crossing time of the constant-fraction signals. Even more importantly, the long risetimes of the detector signals (40 nsec. to 200 nsec.) often cause leading-edge timing to be produced by the constant-fraction discriminator. This latter timing error can be greater by an order of magnitude than the error in the zero-crossing time. The logic signals resulting from leading-edge timing can be eliminated by employing the SRT circuitry.

An analysis was performed to determine the transfer function of a typical signal processing system used in constant-fraction timing

applications with Ge(Li) detectors. The simplified equivalent circuit used in analyzing the system is shown in Figure 3.2, page 43. Using the system transfer function, an approximate solution for the constant-fraction zero-crossing time was derived and is given in Equation (3.38), page 51. The detector current signal used in this derivation was a decaying exponential. The solution shown in Equation (3.38) clearly illustrates that the crossover time of the constant-fraction signal is affected, in a general solution, by the charge-collection time of the detector. This result is one indication that constant-fraction timing is dependent on the shape of the signal from the detector.

Further study of the signal processing system shown in Figure 3.2 revealed that the risetimes of the detector signals can be preserved through the preamplifier and the shaping amplifier. Constraints on the time constants of the signal shaping system were derived to insure that these risetimes can remain unchanged. The constraints on the time constants of the system are given in Equation (3.54), page 57, and Equation (3.55), page 57. Under these conditions constant-fraction timing performed on the leading edge of a processed signal is equivalent to constant-fraction timing performed directly on the leading edge of a detector signal. Thus, the effects of pulse shape variations on constant-fraction timing can be effectively studied with the system shown in Figure 3.2.

The curves shown in Figure 3.3, page 53, illustrate the variations in the shapes of risetimes of the signals from a coaxial Ge(Li) detector as a function of interaction position in the detector. Three functions

were chosen to represent the various general signal shapes seen in Figure 3.3. Decreasing slope signals were represented by the function in Equation (3.56), page 60. Constant slope signals were represented by the linear function given in Equation (3.69), page 63. Increasing slope input signals were represented by the function in Equation (3.76), page 64.

True constant-fraction (TCF) and ARC zero-crossing times were derived for each of the functions chosen to represent detector signals. These expressions are given in Equation (3.59), page 60, and Equation (3.62), page 61, for the decreasing slope signal, in Equation (3.70), page 63, and Equation (3.72), page 63, for the constant slope signal, and in Equation (3.79), page 65, and Equation (3.82), page 66, for the increasing slope signal. These expressions show that each of the three shapes results in a different TCF or ARC zero-crossing time. These derivations further confirm the dependence of constant-fraction timing on detector pulse shape variations.

Expressions for the noise-induced RMS jitter in the TCF and the ARC zero-crossing times were derived for each of the three selected input signal shapes. These jitter terms are given in Equation (3.66), page 62, and Equation (3.68), page 62, for the decreasing slope function, in Equation (3.74), page 64, and Equation (3.75), page 64, for the constant slope function, and in Equation (3.86), page 67, and Equation (3.88), page 67, for the increasing slope function. Furthermore, a general expression was derived to relate the noise on the constant-fraction signal to the noise on the input signal, assuming zero noise contributed

by the constant-fraction circuitry. This expression is given in Equation (2.38), page 33. This equation allowed the limits in Equation (2.41), page 34, to be set for the noise on the constant-fraction signal relative to the noise on the input signal. The derivations for noise-induced time jitter are included to more completely describe the contribution of pulse shape to timing error for the constant-fraction technique.

In Chapters III and IV circuit delay criteria were derived to insure that ARC timing would be provided by the refined discriminator, not by leading-edge timing. Constraints on the constant-fraction shaping delay, t_d, are given in Equation (3.63), page 61, for the decreasing slope input signal, in Equation (3.73), page 63, for the linear input signal, and in Equation (3.83), page 66, for the increasing slope input signal. These constraints on t_d insure that the constant-fraction signals produced by each of the three types of input signals are shaped for ARC timing. The subsequent constraints derived for the fixed delay, t_k, are given in Equation (4.20), page 83, for the increasing slope signal, in Equation (4.39), page 87, for the linear signal, and in Equation (4.54), page 90, for the increasing slope signal. For ARC timing with the signals mentioned above, these constraints on t_k can be reduced to the single constraint given in Equation (4.58), page 92, to allow the SRT circuitry to eliminate timing logic pulses resulting from leading-edge timing in the refined discriminator.

A reduction in the counting efficiency of the refined constant-fraction discriminator is a price paid for improving timing information

through the use of the SRT circuitry. The reduction in the counting efficiency of the discriminator was investigated analytically for the decreasing slope, constant slope and increasing slope input signals, assuming independent probability density functions of energy and risetime. Results of these derivations are given in Chapter IV.

Expressions indicating the loss in counting efficiency were also derived for linear input signals with an exponential risetime probability density function. The effect that the use of the SRT circuitry would produce upon a uniform energy probability density function is given in the modified density function of Equation (4.99), page 114. This equation is plotted in Figure 4.8, page 116, for energies above the threshold level. The SRT circuitry severely limits the counting efficiency of the discriminator for signals only slightly exceeding the threshold level. The counting efficiency loss at a particular energy, E_2, was derived for the exponential risetime probability density function of linear input signals. This expression for the loss in efficiency is given in Equation (4.102), page 117. A plot of the loss in counting efficiency as a function of the threshold level is shown in Figure 4.9, page 118.

The refined constant-fraction discriminator used in the actual testing work was discussed in more detail in Chapter V. Specifications for the instrument were given, including the values of the delay times, t_d and t_k, and the attenuation factor, f. The author of this dissertation was closely involved in the development and the testing of the commercially available instrument that was designed on the principles stated herein.

Experimental results were reported in Chapter VI. The detector used in the experiments was a coaxial Ge(Li) detector with a cylindrical configuration. This device has an active volume of 58.6 cc, a measured efficiency of 10.3 percent, and a FWHM system energy resolution of 1.93 keV for photons at 1.33 MeV. More complete specifications pertaining to this detector are given in the Appendix.

Timing data were obtained for the time relationship between coincident 0.511 MeV gamma-rays from a 10μ Ci, ^{22}Na source. A block diagram of the system used for the timing coincidence measurements is shown in Figure 6.1, page 134. Photographs of twelve timing spectra obtained with this system are shown in Figure 6.2, page 137, and Figure 6.3, page 140. These spectra qualitatively illustrate the relative improvement in timing resolution that was effected by the use of the SRT circuitry.

In Figure 6.4, page 141, and in Figure 6.5, page 142, the timing resolution of the system in Figure 6.1 was plotted versus the threshold level of the refined discriminator. These plots represent the resolution obtained for a 1.1:1 dynamic range of energies, both with and without the use of the SRT circuitry. Use of the SRT circuitry caused an improvement of 33 percent in the FWHM timing resolution for a 1.1:1 dynamic range of signals and a 350 keV threshold setting. An improvement of 48 percent was realized in the FW(1/10)M resolution for a 1.1:1 dynamic range and a 250 keV threshold setting. The measured improvements in timing resolution, combined with the photographs of the approximately normal distributions obtained when using the SRT circuitry, indicate that

the SRT circuitry did eliminate logic pulses resulting from leading-edge timing.

As mentioned previously the counting efficiency of the discriminator is impaired by the use of the SRT circuitry. Calculation of this loss in efficiency requires a knowledge of the distribution of risetimes for signals from the Ge(Li) detector and amplifier system. Figure 6.8, page 149, shows a block diagram of the system that was devised to obtain the probability density function of 10 percent to 90 percent risetimes. For the system that was tested, the risetime probability density function was approximated by a decaying exponential with an average decay time constant of 32.6 nsec. The decay time constant varied less than 10 percent from the average value for gamma spectrum photopeaks in the energy range from 0.5 MeV to 1.4 MeV. These conclusions were drawn from a study of the four risetime distributions shown in Figure 6.9, page 151, and Figure 6.10, page 152, and the corresponding data in Table I, page 153. The 32.6 nsec. decay time constant for the risetime distribution was used in calculating the efficiency loss of the discriminator.

Using the experimentally determined risetime probability density function, the loss in counting efficiency of the discriminator was calculated for linear input signals. From Equation (4.102), page 117, the loss in efficiency at a particular energy, E_2, was plotted as a function of the normalized threshold level. This plot is shown in Figure 6.13, page 163. On the same graph the measured data were plotted for efficiency loss in the 0.511 MeV photopeak of ^{22}Na and for efficiency loss in the 1.174 MeV photopeak of ^{60}Co. A difference of only 7 percent

was obtained between the actual and calculated values of the normalized threshold level at which the efficiency loss of the discriminator became total. Figure 6.11, page 159, shows a block diagram of the system used in determining the efficiency loss of the discriminator. The photographs in Figure 6.12, page 161, show gated energy spectra that were obtained with the system in Figure 6.11 and a ^{60}Co source. These spectra illustrate the dramatic effect that the use of the SRT circuitry has on energy information, relative to the ungated energy distribution.

Suggestions for Further Study

This dissertation showed that ARC timing with coaxial Ge(Li) detectors can be improved significantly by rejecting logic signals resulting from leading-edge timing in the discriminator. Another major source of timing error is inherent in ARC timing with coaxial Ge(Li) detectors. This error can be deduced from Chapter III, where the zero-crossing time of the bipolar, ARC timing signal was shown to change as the shape of the input pulse changed. A constant slope signal, an increasing slope signal and a decreasing slope signal each produces a different crossover time.

Investigations should be conducted to determine a second-order correction technique that would compensate for the changes in the ARC zero-crossing time that was mentioned in the previous paragraph. Some work has been done on a pulse-shape discriminator method[11,12] which provides improved timing resolution at the expense of counting efficiency. The ideal solution would be a correction technique that produces no loss

in counting efficiency. One possible area for future study might lie in nonlinear pulse-shaping to compress the detector signals toward shorter risetimes and more consistent pulse shapes.

Another area in which experimental work should be done is in further characterizing the signal shapes from a coaxial Ge(Li) detector for an uncollimated source. A system was shown in Chapter VI to determine the probability density function of 10 percent to 90 percent risetimes for signals from a Ge(Li) detector. The results obtained with this system were used to good advantage. However, a system should be devised to measure the relative contributions to the risetime distribution, of the decreasing slope, the constant slope, and the increasing slope detector signals.

For an uncollimated radiation source, the average shape of the signals from a Ge(Li) detector could be determined. The system shown in Chapter VI for measuring the risetime distribution would provide an excellent means to this end. Meaningful approximations for the system timing resolution might be derived from a knowledge of the system noise and the average shape of the detector signal.

Further investigations should be made into the best means of forming the constant-fraction signal. In the commercial instrument discussed in this dissertation, the bipolar signal is formed in cascaded ECL line-receivers which operate as linear amplifiers. The poor linear response of these devices increases jitter and walk in the zero-crossing time. A wideband passive network might provide the most reliable and noise-free means of forming the bipolar timing signal.

Advancing technology should spur continuing efforts to improve the performance of constant-fraction discriminators. New techniques for deriving a time-pickoff signal should also be pursued.

REFERENCES

REFERENCES

1. W. J. Price, Nuclear Radiation Detection, McGraw-Hill Book Co., New York, 1964.

2. P. W. Nicholson, Nuclear Electronics, John Wiley and Sons, Inc., New York, 1974.

3. E. E. Gross, "A Theoretical Comparison of Two Methods for Timing with Surface-Barrier Detectors," Ph.D. dissertation, The University of Tennessee, Knoxville, Tenn., 1972.

4. D. A. Gedcke and C. W. Williams, "High Resolution Time Spectroscopy: 1. Scintillation Detectors," ORTEC publication, ORTEC, Inc., Oak Ridge, Tenn., 1968.

5. ORTEC Application Note, AN31, "Timing with Ge(Li) Detectors," ORTEC, Inc., Oak Ridge, Tenn., 1970.

6. R. E. Bell, "Comparison of Leading Edge and Crossover Timing in Coincidence Measurements," Nucl. Inst. and Meth., 42, pp. 211-212, 1966.

7. D. A. Gedcke and W. J. McDonald, "A Constant Fraction of Pulse Height Trigger for Optimum Time Resolution," Nucl. Inst. and Meth., 55, pp. 377-380, 1967.

8. D. A. Gedcke and W. J. McDonald, "Design of the Constant Fraction of Pulse Height Trigger for Optimum Time Resolution," Nucl. Inst. and Meth., 58, pp. 253-260, 1968.

9. R. L. Chase, "Pulse Timing System for Use with Gamma Rays on Ge(Li) Detectors," Rev. of Sci. Inst., 39 (9), pp. 1318-1326, 1968.

10. M. R. Maier and P. Sperr, "On the Construction of a Fast Constant Fraction Trigger with Integrated Circuits and Application to Various Photomultiplier Tubes," Nucl. Inst. and Meth., 87, pp. 13-18, 1970.

11. D. C. S. White and W. J. McDonald, "Recent Developments in Subnanosecond Timing with Coaxial Ge(Li) Detectors," Nucl. Inst. and Meth., 115, pp. 1-11, 1974.

12. W. J. McDonald and D. C. S. White, "Triple Constant-Fraction Discriminator," Nucl. Inst. and Meth., 119, pp. 527-532, 1974.

13. Z. H. Cho and R. L. Chase, "Improved Amplitude and Rise Time Compensated Timing with Ge Detectors," IEEE Trans. Nucl. Sci., NS-19 (1), pp. 451-460, 1972.

14. M. R. Maier and D. A. Landis, "Second Version of a Constant-Fraction Trigger Redesigned with New Integrated Circuits and Results with Semiconductor Detectors," Nucl. Inst. and Meth., 117, pp. 245-247, 1974.

15. N. Karlovac, "Time-Variant Filters in Nuclear Energy Measurements," Ph.D. dissertation, The University of Tennessee, Knoxville, Tenn., 1973.

16. E. Gatti and V. Svelto, "Review of Theories and Experiments of Resolving Time with Scintillation Counters," Nucl. Inst. and Meth., 43, pp. 248-268, 1966.

17. W. J. McDonald and D. A. Gedcke, "Time Resolution Studies on Large Photomultipliers," Nucl. Inst. and Meth., 55, pp. 1-14, 1967.

18. Y. K. Akimov and S. V. Medved, "On the Theory of the Resolving Time of Scintillation Counters," Nucl. Inst. and Meth., 78, pp. 151-153, 1970.

19. R. Nutt, "A Study of a NaI(Tl) Scintillator-Photomultiplier Timing System," Ph.D. dissertation, The University of Tennessee, Knoxville, Tenn., 1969.

20. J. Bialkowski and M. Moszynski, "Timing System for High Resolution Time Spectroscopy," Nucl. Inst. and Meth., 105, pp. 51-56, 1972.

21. R. G. Brown and J. W. Nilsson, Introduction to Linear Systems Analysis, John Wiley and Sons, Inc., New York, 1966.

22. A. Papoulis, Probability, Random Variables, and Stochastic Processes, McGraw-Hill Book Co., New York, 1965.

23. S. Goldman, Laplace Transform Theory and Electrical Transients, Dover Publications, Inc., New York, 1966.

24. T. D. Douglass, "The Application of Filters to Time Analysis of Signals from Ge(Li) Detectors," Ph.D. dissertation, The University of Tennessee, Knoxville, Tenn., 1968.

25. P. G. Coulter, H. C. Evans, and B. C. Robertson, "The Dependence of Ge(Li) Timing Information on Gamma-Ray Intensity Distributions," Nucl. Inst. and Meth., 117, pp. 239-243, 1974.

26. L. Karlsson, "On a Timing Circuit for Ge(Li) Detectors," Nucl. Inst. and Meth., 106, pp. 161-169, 1973.

27. G. Bertolini and A. Coche, Semiconductor Detectors, North-Holland Publishing Co., Amsterdam, 1968.

28. Model 463 Constant Fraction Discriminator, Operating and Service Manual, ORTEC, Inc., Oak Ridge, Tenn., 1971.

29. Model 473 Constant Fraction Discriminator, Operating and Service Manual, ORTEC, Inc., Oak Ridge, Tenn., 1975.

30. ORTEC Application Note, AN34, "Experiments in Nuclear Science," ORTEC, Inc., Oak Ridge, Tenn., 1971.

APPENDIX

APPENDIX

The following data are the specifications for the coaxial lithium-drifted germanium detector-cryostat system.

System serial No. 1741.

System model No. 8101-1020.

Detector size, 40.7 mm dia. x 50.05 mm length.

Diffusion depth, 0.7 mm.

Total active volume, 58.6 cc.

Absorbing layers:

Aluminum, 0.5 mm.

Teflon, 1.0 mm.

Window to detector distance, 5 mm.

Total capacitance, 23 pF at 1000 V.

Recommended operating bias, positive polarity at 4800 V.

Measured total Resolution, 1.93 keV FWHM using 1.33 MeV photons at 3μ sec. amplifier time constant with ORTEC amplifier system with a noise width of 1.24 keV.

Measured peak/Compton, 38.3/1 (Ratio of peak height to Compton plateau height).

Measured efficiency, 10.3 percent (Ratio of area under photopeak to that of 3" x 3" NaI(Tl), measured at 1.333 MeV, source-to-detector distance of 25 cm).

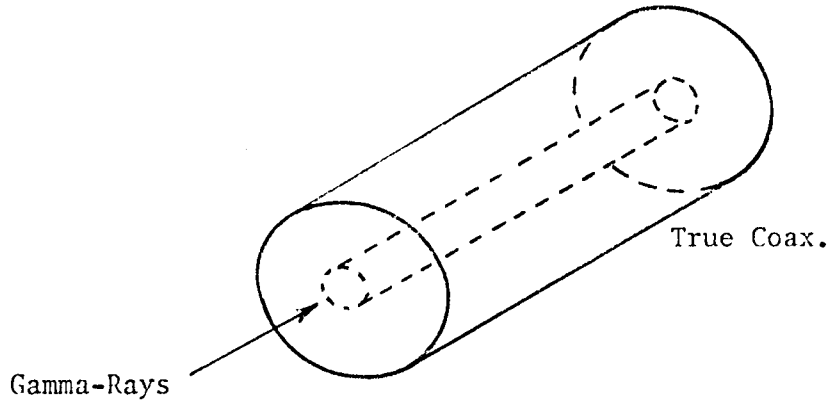


Figure A.1. True coaxial Ge(Li) detector.

VITA

Michael O. Bedwell was born in Chattanooga, Tennessee, on March 1, 1947. He graduated from Brainerd High School, Chattanooga, Tennessee, in June, 1965. The following September he entered Auburn University, Auburn, Alabama. In June, 1969, he received a Bachelor of Electrical Engineering degree at Auburn and was commissioned a Second Lieutenant in the United States Army.

He entered graduate school at the University of Tennessee, Knoxville, Tennessee, in September, 1969. His graduate study for the next three years was funded by a National Defense Education Act, Title IV Fellowship. He received the MS degree in electrical engineering in August, 1972. From September, 1972, to December, 1973, he was employed as a graduate teaching assistant in the Electrical Engineering Department of the University of Tennessee.

From December, 1973, to December, 1974, he was employed as a consultant at ORTEC, Inc., Oak Ridge, Tennessee. He joined the Fast Circuits Group at ORTEC, Inc. in December, 1974. From June, 1975, through August, 1975, he obtained a three months military leave of absence to serve as a First Lieutenant in the U. S. Army. Work on the dissertation was performed at ORTEC, Inc., where he is currently employed.

He is married to the former Sharon Gail Thweatt of Chattanooga, Tennessee. They have one child, Kenneth Wayne Bedwell.